

MultiPulse *Fermi* Gamma-Ray Bursts. I.
Evidence of the Transition from Fireball to Poynting-flux-dominated Outflow

LIANG LI¹

¹*ICRANet, Piazza della Repubblica 10, I-65122 Pescara, Italy*

(Received 2018 October 5; Revised 2019 March 22; Accepted 2019 March 24; Published 2019 May 31)

ABSTRACT

The composition of a jet is still an unsolved problem in gamma-ray bursts (GRBs). Several previous studies have suggested that the prompt emission spectrum of GRBs is likely to consist of a few components that may arise from different jet compositions. Here we present a systematic analysis to search for the GRBs that seem to show the transition from a fireball to the Poynting-flux-dominated outflow between well-separated pulses within a single burst, like the GRB 160626B, using the Gamma-ray Burst Monitor data of the *Fermi* satellite. We obtain 43 GRBs with clear multiple pulses and find that 9/43 (21%) bursts may exhibit such a transition based on the time-integrated spectral analysis. We then select a further four bursts with the data of adequate quality to perform a detailed time-resolved spectral analysis, and we find that in three bursts the thermal-like pulse is a precursor. Furthermore, based on the time-resolved spectra, we constrain the outflow properties for those thermal pulses and find them consistent with the typical properties of the photosphere emission. Also, the later pulses with the softer low-energy spectral index are compatible with the optically thin synchrotron emission model. Our analysis indicates that a good fraction of the multipulse *Fermi* bursts may obtain the transition from fireball to the Poynting-flux-dominated outflow.

Keywords: gamma-ray burst: general methods: data analysis radiation mechanisms: non-thermal

1. INTRODUCTION

Nearly 50 yr after the discovery of gamma-ray bursts (GRBs), the prompt emission of GRBs is still puzzling in several fundamental perspectives (e.g., Popham et al. 1999; Ruffini et al. 1999, 2000; Di Matteo et al. 2002; Gu et al. 2006; Liu et al. 2007; Zhang 2011; Zhang & Yan 2011; Xue et al. 2013; Kumar & Zhang 2015; Pe'er 2015; Liu et al. 2017). A quite fundamental question is the jet composition (baryonic-dominated fireball or Poynting-flux-dominated outflow), which determines or at least strongly affects the energy dissipation mechanism (the shock or the magnetic reconnection), the particle acceleration mechanism (thermally driven or magnetically driven), and especially the

radiation mechanism (synchrotron, Katz 1994; Meszaros et al. 1994; Sari et al. 1996; Daigne & Mochkovitch 1998; Lloyd & Petrosian 2000; Kumar & McMahon 2008; Daigne et al. 2011; Zhang & Yan 2011; Beniamini & Piran 2013, 2014; or Comptonization of quasi-thermal emission from the photosphere, Goodman 1986; Thompson 1994; Rees & Mészáros 2005; Giannios 2006; Beloborodov 2010; Lazzati & Begelman 2010; Giannios 2012; Bégué et al. 2013; Vereshchagin 2014; Pe’Er & Ryde 2017). Several scenarios of the jet composition have been proposed in the literature (e.g., Ryde & Pe’er 2009; Pe’Er et al. 2012; Acuner & Ryde 2018) based on the components in the observed spectrum: (i) a quasi-thermal component indicating a hot fireball origin (Ryde et al. 2010); (ii) a nonthermal component from the synchrotron radiation of the Poynting-flux-dominated outflow (e.g., Preparata et al. 1998, 2002); and (iii) a combination of the quasi-thermal component and nonthermal component from a hybrid jet, consisting of a hot fireball and a cold Poynting flux (Iyyani et al. 2013, 2015; Gao & Zhang 2015).

As mentioned above, the synchrotron radiation and the photosphere emission in the observed spectrum are crucial to judging the jet composition. A criterion that could distinguish the synchrotron and photosphere emission is the observed low-energy spectral index α . Generally speaking, the photosphere model predicts a much harder value of α . For the fast-cooling synchrotron emission (the dynamical timescale is greater than the synchrotron cooling timescale) the predicted α is -1.5 (Sari et al. 1998; Ghisellini & Celotti 1999), much softer than the typical value of -0.8 (Preece et al. 1998, 2000; Burgess et al. 2011; Nava et al. 2011; Zhang 2011; Burgess et al. 2014; Goldstein et al. 2013). The slow-cooling synchrotron emission predicts a much harder value of $\alpha = -2/3$, the so-called line of the death of synchrotron emission (Preece et al. 1998), more consistent with that typical value. Noteworthy, the electrons in the slow-cooling regime are unexpected, due to the usually strong local magnetic field in the prompt emission region (Ghisellini & Celotti 1999; Uhm & Zhang 2014). However, reconciling the slow-cooling spectra, as required by observations, with high efficiency for the prompt emission (as obtained by fast-cooling electrons) is possible to do naturally if synchrotron cooling is balanced by a continuous source of heating (Beniamini et al. 2018). Also, the specific question of electron cooling in magnetic GRB jets has been extensively discussed in Beniamini & Piran (2014). Besides, recent broad time-dependent spectral analysis of GRBs, going beyond the simple Band function (a smoothly joint broken power law, Band et al. 1993), suggests that the synchrotron spectrum is consistent with observations (e.g., Oganessian et al. 2017; Burgess et al. 2018). For the photosphere model, pure blackbody (BB) emission in the Rayleigh-Jeans regime predicts $\alpha \sim +1.0$, while with the curvature effect (equal-arrival-time surface effect) $\alpha \simeq +0.4$ (e.g., Beloborodov 2010; Deng & Zhang 2014). In reality, a pure BB emission is in general never expected from the photosphere, since geometry (Pe’er 2008) and dissipation (Beloborodov 2010) will always broaden the spectrum a bit, but it can be used as an approximation. It is worth noting that the deviation from the straightforward prediction of both models for α can be modified with reasonable assumptions (e.g., Lloyd & Petrosian 2000; Mészáros & Rees 2000; Toma et al. 2011; Lundman et al. 2013; Geng et al. 2018; Meng et al. 2018).

Photosphere emission and synchrotron radiation widely exist in the observed spectrum of GRBs, indicating the different kinds of jet composition. A hot fireball, the Poynting-flux-dominated outflow, or a hybrid jet with both these components in a single burst are the common types of jet composition. But whether the composition can change between different pulses in a single burst is an interesting issue, which seems to be confirmed in Zhang et al. (2018). In that work, the spectral property of

the bright burst GRB 160625B (see also Wang et al. 2017; Wei et al. 2017), with three sub-bursts, is found to change very noticeably between the different sub-bursts, suggesting a different physical origin. Thus, Zhang et al. (2018) for the first time suggest, from early precursor to late main sub-bursts, the transition from fireball to the Poynting-flux-dominated outflow. To go a step further, it is interesting to address the question, what is the proportion of GRBs having observed evidence of the transition from fireball to the Poynting-flux-dominated outflow within a single burst?

In this paper, we have systematically searched for the bright *Fermi* GRBs to perform the time-integrated and the detailed time-resolved spectral analysis. To know whether there is apparent spectral evolution among the multiple pulses¹ (or sub-bursts²) within a single GRB, we are particularly concerned with those GRBs with clear multiple pulses (or sub-bursts) from precursor to the main burst, or extended emission. The explicit goal of this task is to investigate whether there is evidence of the transition from fireball to the Poynting-flux-dominated outflow of GRBs.

The paper is organized as follows. In §2, we perform the spectral analysis and then discuss the fitting parameters of different empirical models. In §3, we derive the fireball parameters for the early thermal pulse and check the synchrotron origin for the later nonthermal pulse. The discussions and conclusions are presented in §4. Throughout the paper, a concordance cosmology with parameters $H_0 = 71 \text{ km s}^{-1} \text{ Mpc}^{-1}$, $\Omega_M = 0.30$, and $\Omega_\Lambda = 0.70$ is adopted. The convention $Q = 10^x Q_x$ is adopted in cgs units.

2. DATA ANALYSIS

This task was carried out by working with the data from the Gamma-ray Burst Monitor (GBM; Meegan et al. 2009) on board the *Fermi Gamma-ray Space Telescope*. More than 2200 GRBs have been detected by the GBM, from 2008 July until 2018 March. The GBM covered the energy range from 8 keV to 40 MeV. It carries two sets of detectors: sodium iodide (NaI) scintillation with 12 detectors, and bismuth germanate (BGO) scintillation with two detectors. All 14 GBM detectors point to different directions and collected the signals of the photon by a Central Data Processing Unit. The 12 NaI detectors play the same role but with a different direction, and they provide an energy range of observations from the 8 keV to 1 MeV. The two BGO detectors provide coverage from 200 keV to 40 MeV. This overlaps with the energy range at the lower end of NaI detectors and lower energies of the Large Area Telescope (LAT), allowing for cross-calibration of the detectors. The BGO detectors are located on opposite sides of the spacecraft to ensure that at least one BGO detector gets illuminated for each possible source location. Three data types of science data that are available in GBM are 128-channel resolution (CSPEC), 8-channel resolution (CTIME), and the time-tagged event (TTE) data. The CSPEC and CTIME are the binned data events. CTIME contains data collected from each detector with 8-channel pulse height resolution and provides data with continuous high time resolution, with a temporal resolution of 0.064 s after triggered time and 0.256 s before triggered time, with the time range from -1000s to 1000 s . CSPEC contains data collected from each detector with 128-channel pulse height resolution and provides data with continuous high spectral resolution, with a temporal resolution of 1.024 s after triggered time and 4.096 s before triggered time, with the time range from -4000 s to 4000 s . The TTE data event is an unbinned data type, consisting of individually digitalized pulse height events from the GBM detector during the event of the burst. It

¹ In the following discussions of the paper, the first pulse (or sub-burst), the second pulse (or sub-burst), the third pulse (or sub-burst), and the fourth pulse (or sub-burst) will be denoted as 1st, 2nd, 3rd, and 4th, respectively.

² The sub-bursts are defined as different pulses that are separated with clear quiescent intervals.

has an energy resolution of 128 channels, which is similar to CSPEC, and records the time interval of photons from the -20 s to 300 s.

The TTE data and the standard response files are used as provided by the GBM team. We selected the data from all the NaI detectors that are triggered by GBM (most cases are one to three) and the brightest BGO detector.

2.1. Data Reduction and Sample Selection

Two main criteria are adopted for a rough sample selection: (i) To perform a detailed time-resolved spectral analysis, brighter bursts³ are required. Therefore, we initially selected all bright bursts from the *Fermi* GBM catalog; (ii) Since it is interesting to investigate whether we have an apparent spectral evolution among the multipulses (or the sub-bursts) within a single GRB, we then obtained all those GRBs that have a clear couple (or more) of distinct pulses (sub-bursts) in our sample, particularly in the GRBs that do not overlap each other significantly. With those selected criteria, we obtain 43 bursts from all 2281 GRBs detected by the GBM until 2018 March 31. In total, 118 pulses/sub-bursts are obtained from these 43 GRBs. In addition to the 43 bursts showing at least two clear pulses/sub-bursts (including 22 bursts that only contain two clear pulses), we also identified 12 bursts having three distinct pulses/sub-bursts, 7 bursts exhibiting four different pulses/sub-bursts, and 2 bursts displaying five pulses/sub-bursts within one single burst.

Observationally, *Fermi* Gamma-ray Observatory has revealed three elemental spectral features of GRBs (Zhang et al. 2011): (i) The Band spectral component, Band function (Band et al. 1993), which is written as

$$N_E = A \begin{cases} \left(\frac{E}{E_{\text{piv}}}\right)^\alpha e^{-E/E_0}, & (\alpha - \beta)E_0 \geq E \\ \left(\frac{(\alpha - \beta)E_0}{E_{\text{piv}}}\right)^{(\alpha - \beta)} e^{(\beta - \alpha)} \left(\frac{E}{E_{\text{piv}}}\right)^\beta, & (\alpha - \beta)E_0 \leq E \end{cases} \quad (1)$$

where N_E is the photon flux (ph/cm²/keV/s), A is the normalization for the spectral fit, E_{piv} is the pivot energy fixed at 100 keV, E is the photon energy, and E_0 is the break energy. The function consists of two power laws that are smoothly separated by a peak energy $E_{\text{pk}} \sim 250$ keV (e.g., Kaneko et al. 2006; Nava et al. 2011), described by the low-energy photon index $\alpha \sim -1.0$,

$$N_E \propto E^\alpha e^{-E/E_{\text{pk}}}, \quad (2)$$

and the high-energy photon index $\beta \sim -2.1$,

$$N_E \propto E^\beta. \quad (3)$$

Equation (2) is also called the CPL function; it can be used when the high-energy photon index β of Band is unconstrained. (ii) A quasi-thermal component (Ryde et al. 2010; Guiriec et al. 2011, 2015; Axelsson et al. 2012). The thermal energy of the photon will be emitted as BB emission when the optical depth goes below unity; the BB emission can be modified by the Planck spectrum, which is given by the photon flux

$$N_E(E, t) = A(t) \frac{E^2}{\exp[E/kT(t)] - 1}, \quad (4)$$

³ Peak flux > 40 photons cm⁻² s⁻¹ or fluence $> 1 \times 10^4$ erg cm⁻².

where E is the photon energy and k is the Boltzmann’s constant. It has two free parameters: $T = T(t)$ and the normalization $A(t)$ of the photon flux⁴. And (iii) A power-law component extending to high energies (Abdo et al. 2010; Zhang et al. 2011)

$$N_E \propto E^s, \quad (5)$$

where s is the power-law index.

Of these, only the BB component indicates a clear physical meaning, which explains as the thermal emission from the photosphere of the outflow. The other two functions do not have any direct physical meaning, although the Band function can be interpreted as being the result of a radiation mechanism (e.g., synchrotron emission), and the power-law component can be a valid approximation of various emission processes over a limited energy range.

2.2. Spectral Fitting and Model Comparison

When performing spectral fits, we need to know several important things: (i) How can we derive the best-fit model parameters from data? (ii) How well does our model fit our data? (iii) How can we choose the best model from given models?

2.2.1. Spectral Fitting

The above-mentioned questions involve two operations that require statistics in spectral fitting: one is parameter estimation, which includes finding the best-fit parameters and its uncertainties for a given model; another is testing whether the model and its best-fit parameters actually match the data, which is usually referred to as determining the goodness of fit (GOF).

For the former operation (parameter estimation), the purpose of performing a spectral fit is first to find the “best-fit” parameters that make a given model optimally consistent with data. On the other hand, the equally important thing is also to find the true likelihood⁵ map in the entire parameter space, with which how the model parameters can be really constrained in a globally confident manner. We adopt the Markov chain Monte Carlo (MCMC) technique to conduct the time-resolved spectral fitting for the following reasons: (i) traditional fitting algorithms (e.g., Levenberg-Marquardt) typically fail to map the multidimensional likelihood; (ii) the theoretical models always involve in multiple model parameters, which may be affected by correlation and multimodality of the likelihood in their parameter space; (iii) the MCMC method can effectively solve multidimensional problems. We therefore perform the MCMC fitting technique based on the Bayesian statistic by using the 3ML tool (see §2.3) to carry out the parameter estimation of data. The priors distribution is used and multiplied by the likelihood that combines the model and the observed data, yielding a posterior distribution of the parameters. Similar techniques have been widely and successfully applied to GRB modeling (e.g., Xu & Huang 2012; Ryan et al. 2015; Zhang et al. 2015). The parameters of our model in the Monte Carlo fit are allowed in the following range—index (PL model): $[-5, 1]$; KT (keV, BB model): $[1, 10^3]$; α (CPL model): $[-5, 1]$; E_c (keV, CPL model): $[1, 10^4]$; α (Band model): $[-5, 1]$; β (Band model): $[-10, 1]$; E_{pk} (keV, Band model): $[1, 10^4]$.

⁴ In reality, photospheric emission is not expected to be a pure Planck function, since several effects (Pe’er 2008; Ryde et al. 2010) need to be taken into account (e.g. the observed BB temperature and the optical depth are the angle dependent). Physically, the photospheric emission therefore should be a multicolor BB (mBB; e.g., Ryde et al. 2010, Hou et al. 2018) instead of a single Planck function.

⁵ The maximum likelihood is the standard statistic used for parameter estimation. This is because the best values of the parameters are those that maximize the probability of the observed data given the model. In other words, finding the maximum likelihood means finding the set of model parameters that maximize the likelihood function.

For the latter operation (test the model and its best-fit parameters), the reduced χ^2 is often used as a measure of fit quality. Indeed, most of the time it is unreliable and incorrect to use (Andrae et al. 2010). Instead, we can almost always use the bootstrap method to estimate the quality of a Maximum Likelihood Estimate (MLE) analysis; the statistic to choose for the MLE is a Poisson–Gaussian profile likelihood (Cash 1979), the so-called Pgstat⁶. The free parameter $\vec{\theta}$ of the likelihood function $L(\vec{\theta})$ usually tends to be very small; therefore, numerically it is more tractable to deal with the logarithmic form of the likelihood function. In practice, the 3ML provides an algorithm to find the minimum of the $-L(\vec{\theta})$ function, which is equivalent to finding the maximum of the $L(\vec{\theta})$ function. To perform the analysis, either the MLE analysis $-\ln(\text{likelihood})$ or the Bayesian analysis $-\ln(\text{posterior})$ can be used. In this paper, we use the minimum logarithm of likelihood-based statistics based on both the MLE analysis (time-integrated spectral fits) and the Bayesian analysis (time-resolved spectral fits). When our data are fitted, we can assess the GOF for the MLE analysis by using $-\ln(\text{likelihood})$ and for the Bayesian analysis via simulating synthetic data sets, $-\ln(\text{posterior})$.

2.2.2. Model Comparison

Since we often need to know which of a suite of models best represents the data, one question is how to choose between different models. The Akaike Information Criterion (AIC; Akaike 1974), defined as $\text{AIC} = -2\ln L(\vec{\theta}) + 2k$, is preferred to discretely select (non-nested, e.g., BB vs. CPL, BB vs. Band, CPL vs. Band) models from a set of models that contains the true data-generating process, under the assumption that the model errors or disturbances are normally distributed, where L is the maximized value of the likelihood function for the estimated model, and k is the number of free parameters to be estimated. The Bayesian Information Criterion (BIC; Schwarz 1978) is better for comparing nested models (e.g., BB vs. PL+BB, BB vs. CPL+BB, BB vs. Band+BB), which is defined as $\text{BIC} = -2\ln L(\vec{\theta}) + k\ln(n)$, where n is the number of observations⁷ (or the sample size). In the Bayesian statistics MCMC case, another criterion, namely, the deviance information criterion (DIC), should be invoked, defined as $\text{DIC} = -2\log[p(\text{data} | \hat{\theta})] + 2p_{\text{DIC}}$, where $\hat{\theta}$ is the posterior mean of the parameters and p_{DIC} is the effective number of parameters. In this paper, we adopt the corresponding criteria for different model comparison scenarios. Given any two estimated models, the preferred model is the one that provides the minimum AIC, BIC, or DIC scores, which are often compared as ΔAIC , ΔBIC , or DIC scores (the difference between the best model and each model). For example, we can use ΔBIC to describe the evidence against a candidate model as the best model in the nested model comparisons. If ΔBIC is greater than 10, the evidence against the candidate model is very strong (Kass & Raftery 1995). Figure S1 presents the time evolution of the $\Delta\text{AIC}/\text{BIC}/\text{DIC}$ in comparison with two different empirical models. For the first pulse/sub-burst (Fig.S1a), we compared the PL+BB model with the CPL model, the PL+BB model with the single BB model, and the CPL model with the single BB model. For the rest pulses/sub-bursts (Fig.S1b), the case displays the CPL model against the Band model. For instance, a majority of ΔBIC have negative values and much less than -10 for the case of the PL+BB model against the single BB model, indicating that the PL+BB is the preferred model in these two models.

⁶ Which statistics should be used depends on the probability distributions underlying the data. Nearly all astronomical data are drawn from two main distributions: Gaussian (normal) or Poisson distributions, e.g., a Gaussian-distributed data with a background (Chi), or a Poisson-distributed data with a Poisson background (Cstat), or a Poisson-distributed data with a Gaussian background (Pgstat). A more detailed discussion can be found in Arnaud et al. (2011) or at the official XSPEC website: <https://heasarc.gsfc.nasa.gov/xanadu/xspec/>.

⁷ Note that if the sample size is large, BIC is superior to AIC.

Another common method is to do hypothesis testing. We can use a likelihood-ratio test to compare the GOF of two statistical models: a null model against an alternative model. This test is based on the likelihood ratio, which expresses how many times more likely the data are under one model than the other. The steps in hypothesis testing are like this: First, set up two possible exclusive hypotheses: the null hypothesis (e.g. BB), which is usually formulated to be rejected, and the alternative hypothesis, which is the research hypothesis (e.g. CPL). Second, specify a priori the significance level $\hat{\alpha}$ (a typical value of 0.05 is usually set). We can reject the null model if the test yields a value of the statistics whose probability of occurrence under the null model is $p < \hat{\alpha}$ (small probability events occurrence). The null model is usually set as a simpler model, while the alternative model is configured as a more complex model.

2.3. Time-integrated Spectral Fit Results

In this work, we adopted the Bayesian approach analysis package, namely, the Multi-Mission Maximum Likelihood Framework (3ML; [Vianello et al. 2015](#)), as the main tool to carry out all the temporal and the spectral analyses. We also used the RMFIT (version 3.3pr7) package⁸ and XSPEC (version 12.9.0) package⁹ ([Arnaud 1996](#)) to ensure consistency of the results across various fitting tools. In this section, we will perform a detailed temporal and spectral analyses to find the character and commonality for our sample.

Observationally, a single power-law component cannot well fit the data for most cases, whereas the Band (or a power-law plus an exponential cutoff, hereafter CPL) component favors the majority of bursts. The interplay among three elemental components indeed can explain a variety of observed GRB spectra ([Guiriec et al. 2015](#)). Therefore, we first perform time-integrated spectral fits by the Band model to each pulse/sub-burst for individual burst. If the values of β are not well constrained (have fairly large values and large uncertainties), we adopt the CPL model to possibly obtain equally good fits for α and E_c . In reality, we find that the high-energy index β indeed cannot be well constrained by the Band model fitting in many time-integrated spectra. Also, as suggested in [Yu et al. \(2016\)](#), the CPL model is probably the best model for a majority of bursts. We therefore use the CPL model for the time-integrated spectral analyses, and mainly focus on the properties of α , and E_c . Since the α value is more important for comparing the physical models, the CPL model is a better choice than the Band model for a rough sample selection when we perform spectral fits.

We select two background intervals (before and after a burst, marked with “Bkg.Selections” in [Figure S2](#)) and fit the light curve with order 0-4 polynomials for one of the triggered NaI detectors. The 0-order of the polynomial can optimally describe a majority of bursts. A source selection is carried out by which we visually inspected the TTE light curves from each of the 43 GRBs (labelled “Selection” in [Figure S2](#)). The maximum-likelihood-based statistics are used, the so-called Pgstat, given by a Poisson (observation; [Cash 1979](#))—gaussian (background) profile likelihood.

We reported the properties of all 43 GRBs in [Table 1](#), together with their results of the time-integrated spectral fits, which include the GBM-triggered number, the each time slice (time interval) of the pulses/sub-bursts, the temporal sequence of the pulses/sub-bursts, the low-energy index α , and the peak energy $E_{\text{pk}(c)}$ of the Band or CPL model; we used the GBM-triggered detectors, the selection criteria (peak flux or fluence), and the $-\ln(L)/\text{dof}$ (degrees of freedom). The light curve of

⁸ <https://fermi.gsfc.nasa.gov/ssc/data/analysis/user/>

⁹ <https://heasarc.gsfc.nasa.gov/xanadu/xspec/>

prompt emission, along with the source selection, the background selections, and the best background fitting, is shown in Figure S2.

We note that here $-\ln(L)^{10}/\text{dof}$ should approach 1 if the statistic follows a chi-square distribution¹¹. We use the Pgstat¹² rather than the chi-square in this paper; this is why $-2\ln(L)/\text{dof}$ cannot be expected to be close to 1 for most of our cases (see Table 1). A detailed discussion of why Pgstat is preferred can be found in Greiner et al. (2016). The main reason that we are using different statistics like Pgstat and Cstat rather than chi-square is that, in the *Fermi* data analysis here, counts per bin are not large and each bin therefore cannot be considered as an observation from a normal distribution. So when counts per bin become large enough, the Poisson distribution can be well approximated by a Gaussian, then Pgstat or Cstat will approach chi-square behaviour, and then in that case $-2\ln(L)/\text{dof}$ can be expected to be close to 1. Otherwise, it is not necessary to be close to 1.

We next compare the low-energy index α and peak energy $E_{\text{pk}(c)}$ between pulses/sub-bursts to investigate how α and $E_{\text{pk}(c)}$ evolve in different pulses/sub-bursts within one single burst. If α and $E_{\text{pk}(c)}$ values are very different, it indicates a different physical process. In Figure S3, we present $\alpha^{\text{P}}-\alpha^{\text{F}}$ (Fig.S3a) and $E_{\text{pk}(c)}^{\text{P}}-E_{\text{pk}(c)}^{\text{F}}$ (Fig.S3b) relations¹³ between different multi-pulses/sub-bursts based on time sequence and find that the relations in later pulses show a more discrete behavior compared with previous ones. This result is confirmed with the quantitative test by using the probabilities of the nonparametric Kendall coefficient¹⁴. This indicates that the spectral evolution prominently occurs in the later pulses. On the other hand, we compare the $E_{\text{pk}(c)}-\alpha$ relation of different pulses/sub-bursts (Figure S4) and find that the $E_{\text{pk}(c)}-\alpha$ relation generally presents two different behaviors for two different α distributions, which show a positive correlation for $\alpha \lesssim -1.0$ while show a negative correlation for $\alpha \gtrsim -1.0$ in the log-linear plots. Moreover, in comparing with the different empirical models, the slope obtained from the Band model is significantly steeper than that of the CPL model for $\alpha \lesssim -1.0$, while interestingly present the same for $\alpha \gtrsim -1.0$ (Figure S4). In general, the global behavior of $E_{\text{pk}(c)}$ presents a hard-to-soft evolution (e.g., Lu et al. 2012).

We select the bursts with such features in our sample: the low-energy index α above $-2/3$ (much harder and close to 0) for the first pulse/sub-burst, and dropping below $-2/3$ (generally range from $-3/2$ to $-2/3$) for the second pulse/sub-burst. In total, based on the time-integrated spectra fitting results, we find that 9 out of 43 bursts in our sample satisfy this criterion significantly. These bursts are GRB 090926181 (Ackermann et al. 2011), GRB 100719989, GRB 140206275 (Götz et al. 2014), GRB140329295, GRB 140523129, GRB 150330828, GRB 160625945 (Zhang et al. 2018), GRB 160820259 (Chand et al. 2018), and GRB 171102107. Such a transition that across the line of the death of synchrotron emission in different pulses/sub-bursts within a single burst could provide a good clue for us to study the jet composition. Based on this, we finally obtain four interesting bursts with adequate data for a further time-resolved spectral analysis and model discussion: GRB 140206B,

¹⁰ Here $-\ln(L)$ needs to be multiplied by 2.

¹¹ Chi-square distribution is defined as if all n independent random variables are subject to the standard normal distribution, and then the sum of the squares of these n random variables obeying the standard normal distribution constitutes a new random variable, whose distribution rule is called the χ^2_ν distribution, where the parameter ν is called the degree of freedom. The chi-square distribution is a new distribution formed by a normal distribution. When the degree of freedom ν is large, the chi-square distribution is approximately normal.

¹² Pgstat = $-2 \ln(L)$.

¹³ The symbols ‘P’ and ‘F’ represent previous and following pulses (or sub-bursts), respectively.

¹⁴ For the Band model $\alpha^{\text{P}}-\alpha^{\text{F}}$ relations, we have $\tau=0.45$ (1st to 2nd), $\tau=0.41$ (2nd to 3rd), and $\tau=-0.33$ (3rd to 4th). For the Band model $E_{\text{pk}}^{\text{P}}-E_{\text{pk}}^{\text{F}}$ relations, one has $\tau=0.46$ (1st to 2nd), $\tau=0.25$ (2nd to 3rd), and $\tau=0.24$ (3rd to 4th).

GRB 140329B, GRB 150330A, and GRB 160625B¹⁵. The lower-energy power-law index¹⁶, α , evolves with time in different pulses/sub-bursts for those bursts and is shown in Figure 1.

2.4. Time Bin Techniques

To perform a time-resolved spectral analysis, how to effectively time-bin the data is a crucial issue, since time-resolved spectral analysis is the main method of extracting information from the data. Burgess (2014) investigated several techniques for temporal binning of GRB spectra—constant cadence (CC), Bayesian blocks (BBlocks, Scargle et al. 2013), signal-to-noise ratio (S/N), and Knuth bins (KB)—and concluded that the S/N and the BBs are two most effective binning methods. Yet both these two techniques have their own disadvantages. The traditional S/N method ensures enough photons to perform the spectral fits, but sometimes it could also destroy the physical structure. BBlocks refer to the technique with the following features (Burgess 2014): (i) each time bin conforms to a constant Poisson rate; (ii) time bins selection is conducted by algorithmically subdividing the flux history of the GRB light curve; (iii) comparing the likelihood of the distribution of the count rate of each bin to being piecewise constant or constant; (iv) possess a variable width and variable S/N; (v) the selection of the time bins demonstrates the true variability of the data. Nevertheless, the technique does not guarantee adequate signal in the bins to carry out an accurate spectral fit.

Therefore, to ensure all the advantages from both these two methods, we first use the BBlocks binning method to time-bin the data, then calculate the S/N value for each individual bin, and obtain the bins that have suitable S/N values (we applied S/N greater than 20 in this paper). Time bins selected in this case thus could be more reasonable.

In Figure S5, we take GRB 140206B as an example to show temporal evolution of the S/N based on the BBlocks technique, along with its light curve of the prompt emission. Time evolution of the S/N and flux track each other for all time bins.

2.5. Time-resolved Spectral Fit Results

We rebin the TTE data by using the BBlocks method with false alarm probability $p_0 = 0.01$ to the TTE light curves of one of the brightest NaI detectors for each burst, and other triggered detectors follow the same bin time information. In total, we obtained 13 pulses/sub-bursts and 132 time-resolved spectra¹⁷ from these four bursts following the BBlocks. All these four bursts in our sample are long GRBs (type II GRBs), with T_{90} being 93.6s (GRB 140206B), 21.5s (GRB 140329B), 153s (GRB 150330A), and 460s (GRB 160625B), respectively. Three bursts (all except GRB 140206B) show a clear short precursor (Hu et al. 2014) characteristics before the main emission episode. The first pulses/sub-bursts for all three bursts in our analysis are consistent with being a precursor of the main burst. This interesting finding is inconsistent with some previous findings (e.g., Troja et al. 2010; Hu et al. 2014), which claimed that no thermal precursor is found in early time. The reason for this could be that early short precursors are typically so weak that they cannot ensure enough photons to perform precise spectral fits. This is why we select the bright bursts in our sample. There is also another possibility. If precursors have low S/N values¹⁸, the underlying spectrum may not

¹⁵ Corresponding to the *Fermi* GBM-triggered burst ID: GRB 140206B (140206275), GRB 140329B (140329295), GRB 150330A (150330828), and GRB 160625B (160625945).

¹⁶ Time-integrated spectral fit results for the first pulses give 0.23 ± 0.21 (Band) and 0.23 ± 0.10 (CPL) for GRB 140206B; -0.32 ± 0.26 (Band) and -0.59 ± 0.14 (CPL) for GRB 140329B; -0.21 ± 0.06 (Band) and -0.30 ± 0.08 (CPL) for GRB 150330A; and 0.02 ± 0.16 (Band) and -0.29 ± 0.13 (CPL) for GRB 160625B.

¹⁷ The number of time-resolved spectra for each burst and their temporal sequence are as follows: 140206B, 3 (1st), 12 (2nd), 8 (3rd); 140329B, 4 (1st), 6 (2nd), 11 (3rd); 150330A, 6 (1st), 21 (2nd), 9 (3rd); 160625B, 7 (1st), 38 (2nd).

¹⁸ Note that we also keep these spectra that have lower S/N values (< 20) in the analysis for precursors, since early short precursors are always weak, and a majority of time-resolved spectra of precursors have low S/N values (< 20).

be reliably obtained. This is because it is difficult to do the model selection, and the finding of the thermal component is not convincing.

Similar to the time-integrated spectral fits, we also find that many cases show an unconstrained β in the time-resolved spectra by the Band model fitting. On the other hand, the CPL model is the best model for a majority of bursts in the GBM GRB time-resolved spectral catalog as suggested in Yu et al. (2016). We therefore use the CPL to perform time-resolved fits for our sample. One interesting question is the difference of the α values comparing the CPL and the Band model (see §2.6). To clarify this, we first take GRB 140206B as an example to study such questions by performing the detailed spectral analysis. GRB 140206B was triggered by GBM (8 keV–40 MeV) on board the *Fermi*, and had a fluence of $(9.93 \pm 0.05) \times 10^{-5} \text{ erg cm}^{-2}$ in the energy range 10 keV–1000 keV. The light curve of the prompt emission of GRB 140206B shows three clear distinct pulses (see Figure 2). Before the main pulse, we find a small pulse with a duration of ~ 5 s. Such a case cannot be defined as a precursor since it does not have a long quiescent interval between it and the main pulse.

Time evolution of α (both the Band and the CPL), $E_{\text{pk}(c)}$ (both the Band and the CPL), BB temperature, and BB flux F_{BB} based on the time-resolved spectrum for GRB 140206B, together with its light curve of prompt emission and typical spectral fits to each sub-burst, are shown in Figure 2. The best-fit parameters and their uncertainties, the $-\ln(\text{posterior})$, the degree of freedom of data, and the statistical parameters AIC, BIC, and DIC, are presented in Table 2.

We obtain four spectra for the first pulse. We first fit the data with the CPL model and find that all α values are above 0, which are much higher than what is typically expected in the synchrotron emission model. We are then motivated to fit the observed spectrum with the single BB model, and we find that it can be fitted well by such a model (an example is shown in Figure S6). Also, comparing with the CPL model, the single BB has lower AIC, BIC, and DIC scores, indicating that the single BB is a preferred model to the data. We also try to add an additional component to the BB component and find that adding a CPL component to the BB neither improves of the GOF nor leads to constraints on the parameters of the new component. However, we find that adding a PL component to the BB can obtain a constraint on the parameters of the new component and an acceptable result of the GOF.

Next, we perform the time-resolved spectral fits for the second and the third pulses by both the Band and the CPL models. A total of 10 spectra in 2nd and 7 spectra in 3rd are obtained¹⁹. We find that the β parameter can not be well constrained for a majority of spectra, ranging within [3.0-8.0]. However, we almost can obtain a good fit result for all the spectra by the CPL model. The result is consistent with the finding in Yu et al. (2016). An example fit to the data in a one time bin of GRB 140206B comparing the Band model and the CPL model is shown in Figure S7 for the case of an unconstrained parameter β and in Figure S8 for the case of a constrained parameter β .

As discussed above, we adopt the following steps for the time-resolved spectral analysis for the remaining bursts (GRB 140329B, GRB 150330A, and GRB 160625B). GRB 140329B, GRB 150330A, and GRB 160625B were all triggered by GBM (8 keV-40 MeV) on board *Fermi*. GRB 140329B also has *Fermi*/IPN burst and LAT detection, and the intense high-energy photon flux of GRB 160625B also triggered the Large Area Telescope (LAT) on board *Fermi*, *Konus-Wind*, INTEGRAL/SPI-ACS,

This indicates that fewer spectra can be obtained and it is difficult to study their evolution properties. On the other hand, we also discard the time bins before triggered time, which are indicated by ellipsis dots in the tables for each analyzed bursts.

¹⁹ Three spectra are discarded since we require an S/N value >20 .

RHESSI and *CALET* (Zhang et al. 2018). Both GRB 140329B and GRB 150330A have two sub-bursts that include three well-separated pulses. The fluence in the energy range 10 keV-40 MeV for GRB 140329B is $(6.70 \pm 0.03) \times 10^{-5}$ erg cm⁻² and for GRB 150330A is $(1.44 \pm 0.06) \times 10^{-4}$ erg cm⁻². GRB 160625B is one of the few extremely bright bursts, composed of three sub-bursts separated by two quiescent times, and has a fluence of $(6.43 \pm 0.02) \times 10^{-4}$ erg cm⁻² in the energy range 10 keV-40 MeV. All three bursts show a short precursor before their main emission episodes, but the duration of precursors and the quiescent interval are quite different. GRB 140329B has a duration of the short precursor of ~ 1.6 s, and a quiescent interval of ~ 18 s, separated between the short precursor and the main burst. GRB 150330A has the longest duration of a precursor, with ~ 10 s. After the precursor, a very long quiescent interval is found before the main bursts arrival, with ~ 110 s. Similarly, a very long quiescent interval is also found in GRB 160625B, with ~ 180 s. However, the duration of precursor for GRB 160625B is short²⁰, with ~ 1 s, which is different from GRB 150330A but similar to GRB 140329B.

Since the first pulses/sub-bursts (hereinafter Part I) in our sample always are involved in a quasi-thermal spectral component, we therefore use all kinds of models that contain the BB component (e.g, single BB, PL+BB, CPL+BB, Band+BB) to perform the time-resolved spectral analysis and choose the best one via the hypothesis testing (an example of the null hypothesis testing between the single BB and the PL+BB model is reported in Table 6) and the AIC/BIC/DIC judgment (Figure S1). To choose the best model, we compare all the used models (together with the CPL model) by analyzing the statistical parameters for the brightest time bins (the highest S/N value) for each burst. We present these statistical parameters in Table 7, which includes the $-\ln(\text{posterior})$ for MCMC based on the Bayesian analysis, the AIC/BIC/DIC scores, and the degree of freedom of data, dof. Based on the statistical analysis, we also list the best model suggested for each burst in the table. Observationally, GRB spectra are typically fitted with standard empirical models containing a single Band function with or without an additional BB (Iyyani et al. 2015). However, we find that the Band+BB components to fit the data show unconstrained fit parameters for all the cases. Besides, in order to check the consistency of the results with the time-integrated spectral fitting, we also redo the spectral fits with the CPL model and find that α values are still very hard (above -2/3) for almost all the cases.

After the first pulses/sub-bursts, the subsequent pulses/sub-bursts (e.g. 2nd, 3rd, 4th, 5th, hereinafter Part II) in our sample typically show a featureless nonthermal spectrum; we thus apply the CPL model to perform the spectral fits. Similarly, we also redo the spectral fits with a BB component if we still find a case with a hard α index (above -2/3). However, we find that almost all the resolved spectra have a softer α index. Also, the CPL model can fit the data well for nearly all cases. The typical spectral fits (the BB for Part I and the CPL for Part II) for our sample are presented in Table 2, Table 3, Table 4, and Table 5.

As argued above, we find that the best models of each sub-burst for time-resolved spectral fits for our sample are as follows:

- GRB 140206B: single BB (part I), CPL (part II);
- GRB 140329B: PL+BB (part I), CPL (part II);

²⁰ The short duration of the precursor with such a long quiescent interval (e.g., GRB 160625B) gives it the appearance of a traditional short GRB, which is undoubtedly related to the main event. To confirm this, the properties between different sub-bursts need to be tested (Zhang et al. 2018).

- GRB 150330A: CPL+BB (part I), CPL (part II);
- GRB 160625B: PL+BB (part I), CPL (part II).

All the best models in the final choice for both Part I and Part II are based on the likelihood-ratio test, namely, hypothesis testing (see in Table 6 and §2.2.2). We apply the suggested best models to derive the characteristic temperature of the photosphere emission, which is used to derive the physical parameters of the photosphere (see §3). The detailed comparison between the single BB model and the PL plus BB model is based on the likelihood-ratio test; see Table 7.

Figures (3-5) present time evolution of α (CPL), E_c (CPL), temperature (BB), and BB flux F_{BB} based on the time-resolved spectrum for the remaining sample (GRB 140329B, GRB 150330A, GRB 160625B), together with their light curves of prompt emission and typical spectral fits to each sub-burst. The evolution of the observed BB temperature kT either a power-law (e.g. GRB 140206B and GRB 140329B) or a broken power-law decay (e.g. GRB 150330A and GRB 160625B). Initially, the temperature is constant with time; later on, it presents a power-law decay after a break, which is consistent with the typical evolution characteristics of kT , found in Ryde & Pe'er (2009). It is interesting to find that the temporal evolution of the observed BB flux F_{BB} , and the BB temperature track each other for all four bursts in our sample²¹ (Crider et al. 1997; Ryde & Pe'er 2009).

After obtaining the observed BB temperature kT , the observed BB flux F_{BB} , and the observed total flux F_{tot} (thermal + nonthermal) from the spectral fits, following Pe'er et al. (2007), we can derive the relevant photosphere properties (see §3 for a more detailed discussion): the isotropic equivalent luminosity of the thermal component L_{BB} , the Lorentz factor of the bulk motion of the flow at the photospheric radius η , and the physical size at the base of the flow r_0 .

2.6. Comparison of Spectral Characteristics with Different Scenarios

Before physics, the key point we need to address from data analysis is whether different phenomenological models (Band vs. CPL), types of spectrum (time-integrated vs. time-resolved), energy channels (e.g., one NaI-triggered detector vs. all), and fitting techniques (frequentist statistic by using the MLE vs. Bayesian statistic based on the MCMC) affect the results.

To account for this, we investigate the difference of α (or $E_{\text{pk}(c)}$) values based on these different scenarios (Figure 6). For different empirical model comparison (Band vs. CPL), we consider the investigation with the following three cases (Figure 6a):

- Case I: the time-integrated spectrum by using the total sample, and the MLE method (based on frequentist statistic), and all the triggered detectors.
- Case II: the time-resolved spectrum by using one single GRB (140206B), and the MCMC technique (based on the Bayesian statistic), and all the triggered detectors.
- Case III: the time-resolved spectrum by using one single GRB (140206B), and the MCMC technique (based on the Bayesian statistic), and one NaI-triggered detector.

We find that α values for the CPL model are slightly softer than the ones for the Band model (Case I), whereas the $E_{\text{pk}(c)}$, in general, present the same. Equivalently, the same result is also found in

²¹ Note that the lower S/N values for some spectra in Part I would cause an unconstrained spectral fitting and an unrealistic evolution picture, such as time bins (0.47-0.67) and (0.67-3.00) for GRB 140329B and (0.93-2.00) for GRB 160625B. Therefore, we need to be cautious when giving the physical interpretation of the data.

their time-integrated spectrum (Case II). Note that our sample meets our selection criteria whether by the Band model or by the CPL model fitting. For a more detailed discussion of a comparison with the Band function fits, see [Yu et al. \(2018\)](#).

Besides, we also check the consistency between different energy channels by using one triggered detector (Case III) to compare with all triggered detectors (Case II). One interesting finding is that the α values are more consistent with each other between these two models if only one NaI-triggered detector is used (marked with orange in Figure 6a). The time-resolved spectral fitting results of GRB 140206B are reported in Table 2.

For different fitting techniques (MLE based on the frequentist statistic vs. MCMC based on the Bayesian statistic), we compare the values of α based on the same CPL model with the following two groups of S/N range (Figure 6b):

- Group I: the time-resolved spectrum by using one single GRB (140206B) with $S/N \geq 20$ and using all the triggered detectors.
- Group II: the time-resolved spectrum by using one single GRB (140206B) with $S/N < 20$ and using all the triggered detectors.

We find that a majority of data points are consistent with each other (tightly distributed around the equal line) for $S/N \geq 20$ (Group I), and only two data points are exceptions. For $S/N < 20$ (Group II), we find that the data points present significant deviation, and with a larger error. This is because lower S/N values cannot ensure that there are enough photons to conduct an accurate spectral fitting. This is why we apply for the criterion of $S/N \geq 20$.

Likewise, based on the same CPL model, we also compare α values between different energy channels (using one NaI detector versus all, marked with blue in Figure 6b); this exhibits an apparent nonmonotonous relation. This implies that the result could be prominently affected by the selection effect.

On the other hand, we also compare the distributions of α (e.g., [Geng & Huang 2013](#)), and $E_{\text{pk}(c)}$ (e.g., [Schaefer 2003](#); [Preece et al. 2016](#)) between the Band and the CPL models and between the time-integrated and the time-resolved spectral fitting results, as presented in Figure 7. They are all well fitted with Gaussian distributions for each sample. For α -distribution by the CPL model, we have $\alpha = -0.89 \pm 0.32$ based on the time-integrated spectral fits and $\alpha = -0.88 \pm 0.25$ based on the time-resolved spectral fits. For α -distribution but by the Band model, we get $\alpha = -0.94 \pm 0.31$ based on the time-integrated spectral fits (Fig. 7a). Similarly, by the same analysis for E_c -distribution, we find $\log E_c = 2.34 \pm 0.27$ based on the time-integrated spectral fits by the CPL model, and $\log E_c = 2.29 \pm 0.25$ based on the time-resolved spectral fits also by the CPL model; and $\log E_{\text{pk}} = 2.48 \pm 0.25$ based on the time-integrated spectral fits but by the Band model (Fig. 7b).

The results indicate that, compared with the distributions based on the time-integrated spectral fits between the Band and the CPL models, the distributions based on the CPL model between the time-integrated and the time-resolved spectral fits are more consistent with each other, both in the $E_{\text{pk}(c)}$ -distribution and in the α -distribution.

3. PHYSICAL SCENARIO

There are two main mechanisms for the acceleration of a GRB jet: thermally driven or magnetically driven. The former one is relevant for a hot fireball and proceeds very rapidly, whereas the latter is

relevant for a Poynting-flux-dominated outflow and proceeds relatively more slowly (Gao & Zhang 2015). In this section, we constrain the outflow properties for those thermal pulses (Part I) to check the photosphere emission origin and confirm the optically thin synchrotron emission for the later pulses (Part II) based on some empirical relations.

3.1. Photosphere Emission Component and Determination of the Outflow Properties

In the early picture of the fireball model, the fireball is composed of the thermal photon and electron-positron pair (Goodman 1986; Paczynski 1986). As the fireball expands and the optical depth goes below unity (at the photosphere radius r_{ph}), the thermal energy of the photon will be emitted as BB emission and thus produce the photosphere emission. Later, it is found that a small amount of the baryon should be included in the fireball, namely, a baryonic fireball rather than the pure radiative fireball (Shemi & Piran 1990). Since the photon luminosity of the fireball is much larger than the Eddington luminosity, in other words, the radiation pressure exceeds self-gravity, the fireball must expand (Meszaros & Rees 1993; Piran et al. 1993). As the fireball expands rapidly, the thermal energy of photons will be converted into the kinetic energy of the baryons from an initial nozzle radius r_0 . According to the conservation of energy and entropy, the bulk Lorentz factor of the outflow increases with radius as $\Gamma \propto r$ while the comoving temperature of BB decreases as $T' \propto r^{-1}$, before the saturation radius $r_s = \eta r_0$, where the Lorentz factor reaches the maximum value $\eta \equiv L_w / \dot{M}c^2$. Here L_w is the isotropic equivalent luminosity, \dot{M} is the ejection mass, and c is the speed of light. Above the saturation radius r_s , the Lorentz factor keeps being constant.

The dissipation mechanism, e.g., internal shocks (Paczynski & Xu 1994; Rees & Meszaros 1994; Tang et al. 2017), magnetic reconnection (Giannios & Spruit 2005; Giannios 2006), or external shocks (Meszaros & Rees 1993; Dermer & Mitman 1999) for the nonthermal emission is still uncertain. However, it is clear that the thermal component originates from the photosphere. Therefore, once identifying a BB component in the observed spectrum, as following we can derive the physical parameters of the outflow as follows (considering the case without subphotospheric dissipation): r_0 , r_s , η , and r_{ph} .

Pe'er et al. (2007) developed a method to determine the initial size of r_0 , and Lorentz factor Γ of GRB fireballs using a thermal emission component. The method in Pe'er et al. (2007) can be applied for the pure fireball model (thermal γ photons+ e^\pm pair). Following Pe'er et al. (2007), once we know all the three observed quantities, the observed BB temperature T_{obs} , the observed BB flux F_{BB} , and the observed total flux F_{tot} (thermal+nonthermal), we can infer the values of the isotropic equivalent luminosity of the thermal component L_{BB} , the Lorentz factor of the bulk motion of the flow at the photospheric radius η , and the physical size at the base of the flow r_0 . This is because in the pure fireball model there are three unknowns, L_{BB} , η , and r_0 . For the bursts with known redshift and measured thermal flux, L_{BB} can be directly measured. The calculations of η and r_0 can follow Equation (4) and Equation (5) in Pe'er et al. (2007) if we know all these three observed quantities (F_{BB} , T_{obs} and F_{tot}).

3.1.1. Flux Ratio, $F_{\text{BB}}/F_{\text{tot}}$

The observed BB flux, F_{BB} , is calculated by integrating the intensity over the emitting surface

$$F_{\text{BB}} = \frac{2\pi}{d_L^2} \int d\mu \mu r_{\text{ph}}^2 D^4 (\sigma T'^4 / \pi), \quad (6)$$

where T' is the comoving temperature at the photospheric radius; $D = D(\theta)$ is the Doppler factor, $D = (\Gamma(1 - \beta\mu))^{-1}$; and so the observed BB temperature is $T = DT' = (\Gamma(1 - \beta\mu))^{-1}T'$, where θ is the angle to the line of sight, $\mu \equiv \cos\theta$, and $\Gamma = (1 - \beta^2)^{-1/2}$ is the outflow Lorentz factor.

The observed ratio of $F_{\text{BB}}/F_{\text{tot}}$ is shown in the left hand panel of Figure 8 for bursts with the best models of PL+BB or CPL+BB, where F_{tot} is the total flux. The evolution properties for this ratio vary from burst to burst. GRB 140329B nearly displays a constant ratio throughout the first sub-pulse with a thermal flux of about 30 per cent, while GRB 150330A show a single power-law decay with a thermal flux initially of about 80% and finally decreasing to about 10%. Interestingly, the thermal flux of GRB 160625B initially increases from about 40% and it peaks at about 50% at around 0.3 s, and finally decreasing to about 10%. The case is similar to GRB 110721A (Iyyani et al. 2013).

3.1.2. Parameter, \mathfrak{R}

Under the spherical symmetry (Pe'er et al. 2007), the ratio between the observed quantity F_{BB} and T , which is denoted as \mathfrak{R} , can be measured by (for $r_{\text{ph}} > r_s$)

$$\mathfrak{R} = \left(\frac{F_{\text{BB}}}{\sigma_{\text{SB}}T^4} \right)^{1/2} = \xi \frac{(1+z)^2 r_{\text{ph}}}{d_L \Gamma}, \quad (7)$$

where σ_{SB} is the Stefan-Boltzmann constant, and ξ is a numerical factor of the order of unity that can be obtained from angular integration, z is the redshift, and d_L is the luminosity distance. The ξ value is adopted as 1.06 in Pe'er et al. (2007). The observed BB normalization, $A(t)$, is related to \mathfrak{R} , $\mathfrak{R} = 2\pi c \hbar^{3/2} A(t)^{1/2}$, where \hbar is the reduced Planck constant.

For bursts with known redshifts, the parameters \mathfrak{R} can be interpreted as an effective transverse size of the emitting region (Ryde & Pe'er 2009). Therefore, a constant \mathfrak{R} means that the effective emitting area of the photosphere is time independent. This is the case for GRB 160625B as presented in the right panel of Figure 8. Moreover, \mathfrak{R} typically is observed to increase over a pulse (Ryde & Pe'er 2009), this is the case for most bursts in our sample, with two prominent cases of GRB 140329B and GRB 150330A.

To derive the parameters in the rest frame, the selected bursts should have known redshift. A redshift measurement of 2.73 is found for GRB 140206B (Malesani et al. 2014), and 1.406 is for GRB 160625B (Zhang et al. 2018). However, GRB 140329B and GRB 150330A are without known redshift. On the other hand, Iyyani et al. (2013) investigated how the different values of redshift affect the results and pointed out that, for different values of z , the estimated outflow parameters change within a factor, but the time evolution of the behavior of the parameters remains the same. We therefore assume an average value of GRBs (Bagoly et al. 2006), $z=2$, for the calculation (see also in Iyyani et al. 2013).

3.1.3. Lorentz Factor, Γ

The coasting values of the Lorentz factor ($r_{\text{ph}} > r_s$) are derived by (see also Equation(4) in Pe'er et al. 2007)

$$\Gamma \propto (F/\mathfrak{R})^{1/4} Y^{1/4}, \quad (8)$$

where Y is the ratio of total fireball energy to the energy emitted in gamma-rays.

As depicted in Figure 9, temporal evolution of the Lorentz factor either an approximately constant (e.g. GRB 140206B) or a monotonic decay behavior (e.g. GRB 140329B exhibits a monotonic decline throughout the pulse), or both (initially approximately constant and then decaying faster, e.g. GRB 150330A, GRB 160625B). The best fitting gives the power-law indices of 0.01 ± 0.07 for GRB 140206B and -0.51 ± 0.03 for GRB 140329B. We fit GRB 150330A and GRB 160625B with a smoothly broken power-law function, which gives the best fitting power-law indices of 0.69 ± 0.52 (before the break) and -0.52 ± 1.44 (after the break) for GRB150330A, and 0.37 ± 0.27 (before the break) and -0.89 ± 0.33 (after the break) for GRB 160625B.

The global view on the evolution of the Lorentz factor decays with time from a few hundred $Y^{1/4}$ down to below $100 Y^{1/4}$ (e.g., Fan & Wei 2011; Peng et al. 2014). The decreasing Lorentz factor may have several implications (Iyyani et al. 2013). Since \mathfrak{R} typically is observed to increase over a pulse, the decrease of the values of $\Gamma = \Gamma(t)$ is not surprising by realizing the fact that $\mathfrak{R} \sim L_0/\Gamma^4$; such a decrease must, therefore, be a common characteristic form over individual pulse structures in GRBs (Ryde & Pe'er 2009). This is because, during the rising phase of the pulse, both the total flux and \mathfrak{R} increase with nearly an approximate rate; the Lorentz factor thus is close to a constant or shows only a moderate decrease with time. However, Γ decays much faster during the decay phase since \mathfrak{R} continues to increase whereas the flux, instead, decreases (Iyyani et al. 2016).

3.1.4. Nozzle Radius, r_0

After obtaining \mathfrak{R} , the calculation of r_0 for the case of $r_{\text{ph}} > r_s$ is given by (see also in Equation (5) in Pe'er et al. 2007),

$$r_0 \propto (F_{\text{BB}}/FY)^{3/2} \mathfrak{R}. \quad (9)$$

Figure 10 presents the evolution of the radii (r_0 , r_s , r_{ph}). The nozzle radius, r_0 , presents a moderate decrease with time for GRB 140206B, GRB 150330A, and GRB 160625B, with a size of the order of from 10^8 to 10^9 cm. Interestingly, the r_0 of GRB 140329B increases by nearly two orders of magnitude throughout the first pulse.

3.1.5. Saturation Radius, r_s

Once we know r_0 , we can get an estimate of the saturation radius, r_s , which is given by

$$r_s = \Gamma r_0. \quad (10)$$

We find that r_{ph} is above r_s in the bursts of our sample, with a typical size of $\sim 10^{11}$ cm (see Figure 10).

3.1.6. Photospheric Radius, r_{ph}

Considering a relativistic bulk motion, for a photon propagating a distance ds , the optical depth, τ , is given by $\tau = \int_{r_{\text{ph}}}^{\infty} \frac{n\sigma_T}{2\Gamma^2} dr$, where σ_T is the Thomson cross section, n is the electron number density, and $ds = (1 - \beta \cos\theta)dr/\cos\theta$, with θ the angle from the line of sight, and considering the case of electron motion in the direction of photon, $\theta = 0$. Assuming that the Lorentz factor is constant (i.e. in the coast phase: $r > r_s$, $\Gamma \equiv \eta$), the optical depth can be integrated by covering the distance $\tau = \frac{L_0\sigma_T}{8\pi m_p c^3 \Gamma^2 \eta} \frac{1}{r}$; the photosphere radius ($\tau = 1$) therefore can be calculated by

$$r_{\text{ph}} = \frac{L_0\sigma_T}{8\pi m_p c^3 \Gamma_{\text{ph}}^3}, \quad (11)$$

where L_0 is the burst luminosity, which is given by $L_0 = 4\pi d_L^2 Y F_{\text{tot}}$, where d_L is the luminosity distance and F_{tot} is the total observed γ -ray flux (thermal+nonthermal).

As shown in Figure 10, the photospheric radius, r_{ph} , shows an increase with time for GRB 150330A while a moderate decrease with time for GRB 140206B, with the size ranging from $\sim 10^{12} Y^{1/4}$ cm to $\sim 10^{13} Y^{1/4}$ cm. GRB 140329B and GRB 160625B are without a significant variation throughout the pulses, exhibiting constant values of r_{ph} , with a size of the order of $10^{13} Y^{1/4}$ cm. The size scale and the moderate variation for the bursts are similar to the results found in some previous studies (Ryde et al. 2010; Guiriec et al. 2013; Iyyani et al. 2013).

3.1.7. Parameter Y

Parameter Y relates to the radiative efficiency (Y^{-1}) of the bursts, which is defined as

$$Y = \frac{L_0}{L_{\text{obs},\gamma}}, \quad (12)$$

where $L_{\text{obs},\gamma}$ is the observed γ -ray luminosity. As discussed in §3.1.3, since the estimations of Γ depend on the parameter Y (Equation 8), the determined evolution in $\Gamma(t)$ therefore could be attributed to corresponding variations in $Y(t)$.

Parameter Y can be inferred from afterglow measurement (Racusin et al. 2011; Wygoda et al. 2016). Wygoda et al. (2016) found that there is relatively small scatter in the estimates of the radiative efficiency of bursts with an average value of $Y \sim 2$, which suggests that large variations in Y within individual bursts are unlikely. Moreover, to investigate this further, Iyyani et al. (2013) assumed a constant Γ throughout the burst and found a large variation in Y within individual bursts in all analyzed bursts in their sample; the corresponding estimated value of Y increases with time from nearly 1 to 1000. Since the evolution in $Y(t)$ also affects the value of r_0 , they then calculated the r_0 based on such evolution of Y , and found that in all bursts r_0 decreases from $\sim 10^8$ to 10^3 cm, which is inapposite with the Schwarzschild radius of the central black hole, since the Schwarzschild radius is of the order of about $10^{6.5}$ cm (Paczynski 1998), and the inferred r_0 values are smaller than the Schwarzschild radius. Therefore, Iyyani et al. (2013) concluded that a large variation of Y cannot account for the observed decrease in Γ . The result confirms the finding in Wygoda et al. (2016).

None of the bursts were observed with afterglow (e.g., Li et al. 2012, 2015, 2018a) in Iyyani et al. (2013); this is why they made such an assumption. Fortunately, we find that one burst in our sample, GRB 140206B, has a good afterglow measurement. This could provide us with a clue to determine the parameter Y directly. GRB 140206B was found to have a black hole central engine (Li et al. 2018b), with prompt γ -ray energy $E_{\gamma,\text{iso}} = 30.68 \pm 1.12$, and isotropic kinetic energy $E_{\text{K},\text{iso}} = 46.28 \pm 8.34$, in units of 10^{52} erg. We therefore obtain an estimation of the parameter Y with afterglow emission for GRB 140206B as ~ 2.51 . This result also confirms well the findings in Iyyani et al. (2013) and Wygoda et al. (2016). It should also be noted that estimating Y from afterglow modeling may critically depend on the estimation of kinetic energy E_{K} . Here we consider only the X-ray band (Wygoda et al. 2016; Li et al. 2018b) to estimate E_{K} , which could also result in a significant underestimate of the true energy of the blast wave (e.g., Beniamini et al. 2015, 2016).

3.1.8. Correlation Analysis

Correlation analysis plays an important role in the understanding of GRB physics, as it provides clues to help for us to reveal their nature (e.g. the Amati relation; Amati et al. 2002). Figure 11 displays several correlations in the flow parameters.

In the top left panel of Figure 11, we show the observed BB flux, F_{BB} , as a function of the temperature, kT . This correlation is also known as the hardness-intensity correlation (Borgonovo & Ryde 2001; Ryde & Pe’er 2009). The energy flux is found to increase with the temperature in most cases in our sample (except for GRB 140206B, with only three time bins). Ryde & Pe’er (2009) analyze the correlation with a BATSE sample and point out that such a hardness–intensity correlation can be described as $F_{\text{BB}} \propto T^\delta$ with a power-law index of $\delta \simeq 4$, and this is the fundamental property of a BB emitter. In our cases, we find similar results; the best-fit results (see the dashed lines in Figure 11) show a power-law index of 3.95 ± 0.25 for GRB 160625B, 3.21 ± 1.11 for GRB 140329B, and 1.60 ± 0.41 for GRB 150330A.

In the top right panel of Figure 11, we display the parameter \mathfrak{R} plotted versus its temperature kT for these bursts. We find a tight negative correlation for all the bursts. The best fitting gives the power-law indices as -1.71 ± 0.57 for GRB 140329B, -1.10 ± 0.14 for GRB 150330A, and -0.38 ± 0.13 for GRB 160625B.

In the left bottom panel of Figure 11, we compare the BB luminosity L_{BB} with the nonthermal luminosity $L_{\text{Non-thermal}}$ within the bursts. We also find a hardness–intensity correlation in this; the BB luminosity is found to increase with the nonthermal luminosity, and the BB luminosity for all our bursts are found to be slightly below to the nonthermal luminosity. The best fitting gives the power-law indices as 0.81 ± 0.09 for GRB 140329B, and 1.57 ± 0.11 for GRB 160625B.

In the bottom right panel of Figure 11, we present the Lorentz factor Γ_{ph} against the the BB luminosity L_{BB} . A tight positive correlation is also found in our sample; the power-law indices typically range within $[0.25, 0.50]$. We obtain 0.44 ± 0.02 for GRB 140329B, 0.37 ± 0.04 for GRB 150330A, and 0.28 ± 0.02 for GRB 160625B.

3.2. Synchrotron Emission Component

Phenomenologically, most GRBs can be explained by an observed nonthermal spectrum, that is, the synchrotron component. In this section, we study another case in which a cold Poynting flux fully dominated outflow for the following pulses (Part II) of our sample.

We revisited the method that was applied in Iyyani et al. (2016) for our sample. We first simply review the basic points of synchrotron emission²². The dissipation of the kinetic energy of the outflow at a certain radius accelerates the electrons to some characteristic Lorentz factor, and the observed peak energy of synchrotron emission from these electrons can be written as

$$E_{\text{syn}} = \frac{3}{2} \hbar \frac{qB}{m_e c} \gamma_e^2 \frac{\Gamma}{(1+z)}, \quad (13)$$

where \hbar is the reduced Plank constant, q and m_e are the charge and the mass of an electron, respectively, and B is the magnetic field intensity in the comoving frame. The observed flux from synchrotron emission is given by

$$F_{\text{syn}} = \frac{\sigma_T c \Gamma^2 \gamma_e^2 B^2 N_e}{24\pi^2 d_L^2}, \quad (14)$$

²² Here note that the model is based on implicitly assuming isotropic synchrotron emission in the comoving frame. However, there have been various works in recent years suggesting that there should be bulk relativistic motions in the comoving frame, either due to “mini-jets” (e.g., Lyutikov & Blandford 2003; Giannios et al. 2009; Kumar & Narayan 2009; Lazar et al. 2009; Barniol Duran et al. 2016; Beniamini et al. 2018) or due to a striped wind magnetic field geometry (e.g., Beniamini & Granot 2016). Specifically, this effect can have important implications on the pulse width.

where N_e is the number of radiating electrons. The electrons will cool when they emit radiation, and the radiative cooling time is given by

$$t_{\text{cool}} = \frac{6\pi m_e c}{\sigma_T B^2 \pi^2 \Gamma \gamma_e^2 (1 + \mathcal{Y})}, \quad (15)$$

where \mathcal{Y} is the Compton \mathcal{Y} -parameter. The dynamical time can be defined as²³

$$t_{\text{dyn}} \simeq \frac{R}{2\Gamma^2 c}. \quad (16)$$

There are two cases: (i) fast-cooling, $t_{\text{dyn}} > t_{\text{cool}}$, where the electrons lose all their energy by synchrotron radiation within the dynamical time, and all the electrons cool fast down to ν_c (characteristic frequency); and (ii) slow-cooling, $t_{\text{dyn}} < t_{\text{cool}}$, where the electrons do not efficiently radiate and therefore do not lose their energy within the dynamical time.

The synchrotron emission model is troubled by many uncertain parameters. In general, it is difficult to constrain all relevant parameters precisely, since there are only a few observed qualities. One thing we usually need to think is how to effectively constrain the synchrotron emission model parameters through a finite number of observations.

Assuming that the properties of the outflow are the same at the photosphere and at the dissipation site, we can give a constraint for the $B\gamma_e^2$ in each time bin from Equation (13),

$$B\gamma_e^2 = \frac{E_{\text{syn}}(1+z)4\pi m_e c}{\Gamma 3hq}. \quad (17)$$

We show them as the black lines in Figure 12, where constraints obtained for three time bins are plotted: one before (earliest), one at, and one after (latest) the peak photon flux in order to capture the time evolution.

Furthermore, Equation (13) is substituted into Equation (17), and therefore we can obtain the expression of the cooling time, t_{cool} , as a function of γ_e (see the right-hand y-axis in Figure 12),

$$\frac{\gamma_e^3}{(1+\mathcal{Y})t_{\text{cool}}} = \frac{8\pi m_e c \sigma_T E_{\text{syn}}^2 (1+z)^2}{27\Gamma h^2 q^2}. \quad (18)$$

The cooling timescale, t_{cool} , is very sensitive to the change in γ_e as described in Equation (18), resulting in longer cooling times for large values of γ_e .

Over the blue lines, we mark the dynamical time given by Equation (16) for r_{ph} and t_{pulse} with green and red stars, as well as the dynamical time for 10^{14} cm (gray star). There are three regimes: (i) The red area lines show the values of γ_e and B that result in $t_{\text{cool}} < t_{\text{dyn}}(r_{\text{ph}})$ for all allowed values of $r_d > r_{\text{ph}}$, which indicates that the electrons are always in the fast-cooling regime. (ii) The width of the pulse of the bursts, t_{pulse} , can give an upper limit of the dynamical time, which corresponds to an upper limit of the allowed dissipation radius, $r_{d,\text{max}} = 2\Gamma^2 c t_{\text{pulse}}$. Therefore, the orange area lines represent that the values of γ_e and B will always result in $t_{\text{cool}} < t_{\text{pulse}}$, which is in the slow-cooling regime for the allowed values of r_d . (iii) Finally, the black area lines represent the values of γ_e and B for the case $t_{\text{dyn}}(r_{\text{ph}}) < t_{\text{cool}} < t_{\text{pulse}}$, which can result in synchrotron emission for electrons cooling

²³ Equation (16) only holds if the width of the emitting shell is determined by the causal length scale (Beniamini & Piran 2013).

either fast or slow depending on what the corresponding dynamical time is and where the dissipation occurs.

On the other hand, since the observed peak energy of synchrotron emission (here assuming that the peak energies of synchrotron emission are the same as derived from the CPL model) can be derived from the spectral fits. According to Equation (17), one has $B\gamma_e^2 \propto \Gamma^{-1}$. Analytically in prior articles (Beniamini & Piran 2013; Uhm & Zhang 2014) it is suggested that both B , and γ_e , evolve during the burst. One question is, if we assume a constant Γ throughout a burst, how is the evolution characteristic of $B\gamma_e^2$? Since Γ has a typical value of a few hundred, one can therefore reliably estimate the typical values of $B\gamma_e^2$. We thus can study the evolution of $B\gamma_e^2$ in all time bins within bursts.

To investigate this further, we illustrate the evolution of $B\gamma_e^2$ within bursts for different Γ values ($\Gamma=100, 300, 600, 1000$) for all the analyzed bursts in Figure S9. We find that $B\gamma_e^2$ indeed decreases with time and has a narrow distribution, typically ranging from 10^{11} to 10^{12} for all the cases. This, in turn, suggests that Γ decreases during the bursts. Also, if considering a lower limit on B being between 10^{-3} and 10^{-4} G, and therefore an upper limit on γ_e lying at \sim few time 10^7 , this result is consistent with the finding in Iyyani et al. (2016), or if considering a typical value of $B \sim 10^3$ G, thereby γ_e lying at $\sim 10^4$. Furthermore, we also show the distributions of $B\gamma_e^2$ for these typical values of Γ in Figure S9. All the distributions can well fitted by the Gaussian function. The typical fits give $\log B\gamma_e^2=11.81\pm 0.19$ for $\Gamma=100$, $\log B\gamma_e^2=11.26\pm 0.18$ for $\Gamma=300$, $\log B\gamma_e^2=10.95\pm 0.19$ for $\Gamma=600$, and $\log B\gamma_e^2=10.83\pm 0.18$ for $\Gamma=1000$.

4. DISCUSSION AND CONCLUSION

4.1. Magnetization parameter, σ_0 , and the Hybrid jet system

The physical scenarios discussed above indeed always focus on the extreme cases: either a pure hot fireball dominated outflow or a Poynting flux fully dominated outflow. However, another more natural possibility is that the central engine of GRB jets is more likely to be a hybrid system, which is involved in both a hot fireball component and a cold Poynting flux component simultaneously (e.g., Ryde 2005; Giannios 2006; Battelino et al. 2007; Ryde & Pe’er 2009; Guiriec et al. 2011; Axelsson et al. 2012; Iyyani et al. 2013; Burgess et al. 2014; Gao & Zhang 2015; Bégué & Pe’er 2015; Nappo et al. 2017; Beniamini & Giannios 2017). Based on this fact, a theory of photosphere emission for a hybrid outflow with a hot fireball component and a cold Poynting flux component has been developed in Gao & Zhang (2015). Two parameters are used to describe the hybrid outflow: the dimensionless entropy for the hot component $\eta = L_{\text{hot}}/\dot{M}c^2$ and the magnetization parameter for the Poynting flux component $\sigma_0 \equiv L_{\text{Poynting}}/L_{\text{hot}}$. The different combinations of the parameters (η, σ_0) ²⁴ mainly correspond to three types of observation: (i) if $\eta \gg 1$ and $\sigma_0 \ll 1$, a pure hot fireball is obtained (e.g., the most typical case, GRB 090902B with dominated BB component); (ii) if η is smaller and σ_0 is larger, the photosphere emission component becomes subdominant with a nonthermal component (e.g., GRB 110721A, which can be best fitted by the Band function plus a BB.); (iii) if η is close to unity and $\sigma_0 \gg 1$, the outflow is fully dominated by the Poynting flux (e.g., GRB 080916C). In

²⁴ Note that in the “hybrid” models, changing (η, σ_0) may result in completely different dynamics for the jet. For example, for magnetically dominated jets, the Lorentz factor no longer evolves linearly with radius (Drenkhahn 2002; Giannios & Uzdensky 2019). This can have significant effects on both the resulting radiation of both the thermal component (Beniamini & Giannios 2017) and the application to data in Xiao et al. (2018).

Gao & Zhang (2015), the photosphere parameters for these different regimes of (η, σ_0) are derived. However, for the hybrid model, further constraints by observation are required.

4.2. Polarization, Future Prospects

Theoretically, photon polarization is an extra important tool to diagnose jet composition and radiation mechanism (Toma et al. 2009; Lundman et al. 2013; Zhang 2014). Thus, the transition of the jet composition in quite a number of GRBs found in this work can be tested by the observation of polarization. This test cannot be achieved by the current polarization data (e.g., the POLAR detect; Zhang et al. 2019), which is eager for future observations. Interestingly, two bursts (GRB 160625B, and GRB 160820A) in our sample are reported to have the observation of polarization (Troja et al. 2017; Chand et al. 2018). Besides, the corresponding X-ray, optical, and other energy-band afterglows for these bursts may also be different, which requires further observations to confirm in the future.

4.3. Conclusion

In this paper, we systematically searched for evidence of the transition from fireball to Poynting-flux-dominated outflow of GRBs with *Fermi* data. We first fit the time-integrated spectra for the bursts with the Band and the CPL models, respectively, and found that α is much harder (close to 0) for Part I (the first pulse/sub-burst). We then further fit the time-resolved spectra in each slice with the CPL model and also found that the results are consistent with the former analysis. Such a photon index is beyond the so-called synchrotron line of death ($\alpha=-2/3$, Preece et al. 1998), and is much harder than the typical α value ($\alpha=-1.0$) of long GRBs, thus suggesting a significant contribution of thermal emission from the fireball photosphere (Ryde et al. 2010; Mészáros & Rees 2000). Furthermore, it is interesting to find that three bursts exhibit a thermal precursor before the main bursts (Murakami et al. 1991). Part II (the following pulses/sub-bursts) cannot be fitted by a Plank function but can be well fitted by the empirical CPL function, suggesting a synchrotron origin. The average α of the time-integrated spectra for Part II is consistent with the typical α distribution.

In summary, after performing a detailed spectral analysis, except for GRB 160625B, we find three more bursts whose spectral properties of the pulses/sub-bursts are quite different, showing the transition from thermal emission to nonthermal emission between well-separated pulses/sub-bursts within a single GRB. Such a transition is likely to be the evidence of the change of jet composition from a hot fireball to a cold Poynting-flux-dominated outflow. The main results can be drawn as follows:

- 43 bright *Fermi* bursts exhibit at least two clear pulses in their prompt emission light curves in our sample. In total, 9 out of 43 bursts ($\sim 21\%$) are found to have a transition from fireball (thermal) to Poynting-flux-dominated (non-thermal) outflow based on the time-integrated spectra. This indicates that such a transition is commonly detected in the bright multipulse *Fermi* bursts.
- Among these bursts, we select four cases (including GRB 160625B) with adequate data to perform the detailed time-resolved spectral analysis. Three out of four bursts present an early precursor before the main burst, which shows that a thermal characteristic exists in both their time-integrated spectrum and time-resolved spectra. Moreover, we also find that the duration of the early thermal component is much shorter than that of the nonthermal component, which implies that the thermal process proceeds more rapidly than the nonthermal one.

- Part I, indeed, can be well fitted by the model that contains a BB component. Based on the model of thermal+ nonthermal components, we derive outflow properties, which are consistent with the typical observation from the photosphere emission. Part II can be well explained by the optically thin synchrotron emission component.
- Other interesting results:
 - (1) The spectral evolution could be more prominent to occur in later pulses.
 - (2) The low-energy power-law index α , obtained from the CPL model, is slightly softer than that from the Band model.
 - (3) We have introduced a new, more reasonable time-bin method of the time-resolved spectra, which combines the advantages of both the traditional S/N and the BBlocks techniques.
 - (4) We find that, in comparing with the distributions of the different empirical models (the Band and the CPL) based on the same type of spectrum (time-integrated), the distributions of different type of spectra (time-integrated and time-resolved) based on the same model (the CPL) are more consistent with each other, whether by the $E_{\text{pk}(c)}$ -distribution or by the α -distribution.

We conclude that *a good fraction of the multipulse Fermi bursts present implication of a transition from fireball to Poynting-flux-dominated outflow.*

I am grateful to Felix Ryde, Shabnam Iyyani, Damien Bégué, Bing Zhang, Yu Wang, Bin-Bin Zhang, Asaf Pe’er, Pawan Kumar, Jin-Jun Geng, Yan-Zhi Meng, Yong-Feng Huang, Li-Ping Xin, Shuang-Nan Zhang, and Gregory Vereshchagin for useful discussions, and I appreciate to the referee for the constructive report. I also thank the following people who provided indirect help on the subject: Xue-Feng Wu, Xiang-Yu Wang, Zi-Gao Dai, Thomas Pak-Hin, Yi-Zhong Fan, Da-Ming Wei, Wei-Min Gu, Jian-Yan Wei, and Remo Ruffini. This research made use of the High Energy Astrophysics Science Archive Research Center (HEASARC) Online Service at the NASA/Goddard Space Flight Center (GSFC). Part of this work made use of our personal Python library.

Facilities: Fermi/GBM

Software: 3ML([Vianello et al. 2015](#))

REFERENCES

- Abdo, A. A., Ackermann, M., Ajello, M., et al. 2010, ApJ, 712, 558, doi: [10.1088/0004-637X/712/1/558](https://doi.org/10.1088/0004-637X/712/1/558)
- Ackermann, M., Ajello, M., Asano, K., et al. 2011, ApJ, 729, 114, doi: [10.1088/0004-637X/729/2/114](https://doi.org/10.1088/0004-637X/729/2/114)
- Acuner, Z., & Ryde, F. 2018, MNRAS, 475, 1708, doi: [10.1093/mnras/stx3106](https://doi.org/10.1093/mnras/stx3106)
- Akaike, H. 1974, IEEE Transactions on Automatic Control, 19, 716
- Amati, L., Frontera, F., Tavani, M., et al. 2002, A&A, 390, 81, doi: [10.1051/0004-6361:20020722](https://doi.org/10.1051/0004-6361:20020722)
- Andrae, R., Schulze-Hartung, T., & Melchior, P. 2010, arXiv e-prints. <https://arxiv.org/abs/1012.3754>
- Arnaud, K., Smith, R., & Siemiginowska, A. 2011, Handbook of X-ray Astronomy

- Arnaud, K. A. 1996, in *Astronomical Society of the Pacific Conference Series*, Vol. 101, *Astronomical Data Analysis Software and Systems V*, ed. G. H. Jacoby & J. Barnes, 17
- Axelsson, M., Baldini, L., Barbiellini, G., et al. 2012, *ApJL*, 757, L31, doi: [10.1088/2041-8205/757/2/L31](https://doi.org/10.1088/2041-8205/757/2/L31)
- Bagoly, Z., Mészáros, A., Balázs, L. G., et al. 2006, *A&A*, 453, 797, doi: [10.1051/0004-6361:20054322](https://doi.org/10.1051/0004-6361:20054322)
- Band, D., Matteson, J., Ford, L., et al. 1993, *ApJ*, 413, 281, doi: [10.1086/172995](https://doi.org/10.1086/172995)
- Barniol Duran, R., Leng, M., & Giannios, D. 2016, *MNRAS*, 455, L6, doi: [10.1093/mnras/slv140](https://doi.org/10.1093/mnras/slv140)
- Battelino, M., Ryde, F., Omodei, N., & Band, D. L. 2007, in *American Institute of Physics Conference Series*, Vol. 921, *The First GLAST Symposium*, ed. S. Ritz, P. Michelson, & C. A. Meegan, 478–479
- Bégué, D., & Pe’er, A. 2015, *ApJ*, 802, 134, doi: [10.1088/0004-637X/802/2/134](https://doi.org/10.1088/0004-637X/802/2/134)
- Bégué, D., Siutsou, I. A., & Vereshchagin, G. V. 2013, *ApJ*, 767, 139, doi: [10.1088/0004-637X/767/2/139](https://doi.org/10.1088/0004-637X/767/2/139)
- Beloborodov, A. M. 2010, *MNRAS*, 407, 1033, doi: [10.1111/j.1365-2966.2010.16770.x](https://doi.org/10.1111/j.1365-2966.2010.16770.x)
- Beniamini, P., Barniol Duran, R., & Giannios, D. 2018, *MNRAS*, 476, 1785, doi: [10.1093/mnras/sty340](https://doi.org/10.1093/mnras/sty340)
- Beniamini, P., & Giannios, D. 2017, *MNRAS*, 468, 3202, doi: [10.1093/mnras/stx717](https://doi.org/10.1093/mnras/stx717)
- Beniamini, P., & Granot, J. 2016, *MNRAS*, 459, 3635, doi: [10.1093/mnras/stw895](https://doi.org/10.1093/mnras/stw895)
- Beniamini, P., Nava, L., Duran, R. B., & Piran, T. 2015, *MNRAS*, 454, 1073, doi: [10.1093/mnras/stv2033](https://doi.org/10.1093/mnras/stv2033)
- Beniamini, P., Nava, L., & Piran, T. 2016, *MNRAS*, 461, 51, doi: [10.1093/mnras/stw1331](https://doi.org/10.1093/mnras/stw1331)
- Beniamini, P., & Piran, T. 2013, *ApJ*, 769, 69, doi: [10.1088/0004-637X/769/1/69](https://doi.org/10.1088/0004-637X/769/1/69)
- . 2014, *MNRAS*, 445, 3892, doi: [10.1093/mnras/stu2032](https://doi.org/10.1093/mnras/stu2032)
- Borgonovo, L., & Ryde, F. 2001, *ApJ*, 548, 770, doi: [10.1086/319008](https://doi.org/10.1086/319008)
- Burgess, J. M. 2014, *MNRAS*, 445, 2589, doi: [10.1093/mnras/stu1925](https://doi.org/10.1093/mnras/stu1925)
- Burgess, J. M., Bégué, D., Bacelj, A., et al. 2018, *arXiv e-prints*, <https://arxiv.org/abs/1810.06965>
- Burgess, J. M., Preece, R. D., Baring, M. G., et al. 2011, *ApJ*, 741, 24, doi: [10.1088/0004-637X/741/1/24](https://doi.org/10.1088/0004-637X/741/1/24)
- Burgess, J. M., Preece, R. D., Connaughton, V., et al. 2014, *ApJ*, 784, 17, doi: [10.1088/0004-637X/784/1/17](https://doi.org/10.1088/0004-637X/784/1/17)
- Cash, W. 1979, *ApJ*, 228, 939, doi: [10.1086/156922](https://doi.org/10.1086/156922)
- Chand, V., Chattopadhyay, T., Iyyani, S., et al. 2018, *ApJ*, 862, 154, doi: [10.3847/1538-4357/aacd12](https://doi.org/10.3847/1538-4357/aacd12)
- Crider, A., Liang, E. P., Smith, I. A., et al. 1997, *ApJL*, 479, L39, doi: [10.1086/310574](https://doi.org/10.1086/310574)
- Daigne, F., Bošnjak, Ž., & Dubus, G. 2011, *A&A*, 526, A110, doi: [10.1051/0004-6361/201015457](https://doi.org/10.1051/0004-6361/201015457)
- Daigne, F., & Mochkovitch, R. 1998, *MNRAS*, 296, 275, doi: [10.1046/j.1365-8711.1998.01305.x](https://doi.org/10.1046/j.1365-8711.1998.01305.x)
- Deng, W., & Zhang, B. 2014, *ApJ*, 785, 112, doi: [10.1088/0004-637X/785/2/112](https://doi.org/10.1088/0004-637X/785/2/112)
- Dermer, C. D., & Mitman, K. E. 1999, *ApJL*, 513, L5, doi: [10.1086/311898](https://doi.org/10.1086/311898)
- Di Matteo, T., Perna, R., & Narayan, R. 2002, *ApJ*, 579, 706, doi: [10.1086/342832](https://doi.org/10.1086/342832)
- Drenkhahn, G. 2002, *A&A*, 387, 714, doi: [10.1051/0004-6361:20020390](https://doi.org/10.1051/0004-6361:20020390)
- Fan, Y.-Z., & Wei, D.-M. 2011, *ApJ*, 739, 47, doi: [10.1088/0004-637X/739/1/47](https://doi.org/10.1088/0004-637X/739/1/47)
- Gao, H., & Zhang, B. 2015, *ApJ*, 801, 103, doi: [10.1088/0004-637X/801/2/103](https://doi.org/10.1088/0004-637X/801/2/103)
- Geng, J. J., & Huang, Y. F. 2013, *ApJ*, 764, 75, doi: [10.1088/0004-637X/764/1/75](https://doi.org/10.1088/0004-637X/764/1/75)
- Geng, J.-J., Huang, Y.-F., Wu, X.-F., Zhang, B., & Zong, H.-S. 2018, *ApJS*, 234, 3, doi: [10.3847/1538-4365/aa9e84](https://doi.org/10.3847/1538-4365/aa9e84)
- Ghisellini, G., & Celotti, A. 1999, *ApJL*, 511, L93, doi: [10.1086/311845](https://doi.org/10.1086/311845)
- Giannios, D. 2006, *A&A*, 457, 763, doi: [10.1051/0004-6361:20065000](https://doi.org/10.1051/0004-6361:20065000)
- . 2012, *MNRAS*, 422, 3092, doi: [10.1111/j.1365-2966.2012.20825.x](https://doi.org/10.1111/j.1365-2966.2012.20825.x)
- Giannios, D., & Spruit, H. C. 2005, *A&A*, 430, 1, doi: [10.1051/0004-6361:20047033](https://doi.org/10.1051/0004-6361:20047033)
- Giannios, D., & Uzdensky, D. A. 2019, *MNRAS*, 484, 1378, doi: [10.1093/mnras/stz082](https://doi.org/10.1093/mnras/stz082)
- Giannios, D., Uzdensky, D. A., & Begelman, M. C. 2009, *MNRAS*, 395, L29, doi: [10.1111/j.1745-3933.2009.00635.x](https://doi.org/10.1111/j.1745-3933.2009.00635.x)
- Goldstein, A., Preece, R. D., Mallozzi, R. S., et al. 2013, *ApJS*, 208, 21, doi: [10.1088/0067-0049/208/2/21](https://doi.org/10.1088/0067-0049/208/2/21)

- Goodman, J. 1986, *ApJL*, 308, L47, doi: [10.1086/184741](https://doi.org/10.1086/184741)
- Götz, D., Laurent, P., Antier, S., et al. 2014, *MNRAS*, 444, 2776, doi: [10.1093/mnras/stu1634](https://doi.org/10.1093/mnras/stu1634)
- Greiner, J., Burgess, J. M., Savchenko, V., & Yu, H.-F. 2016, *ApJL*, 827, L38, doi: [10.3847/2041-8205/827/2/L38](https://doi.org/10.3847/2041-8205/827/2/L38)
- Gu, W.-M., Liu, T., & Lu, J.-F. 2006, *ApJL*, 643, L87, doi: [10.1086/505140](https://doi.org/10.1086/505140)
- Guiriec, S., Connaughton, V., Briggs, M. S., et al. 2011, *ApJL*, 727, L33, doi: [10.1088/2041-8205/727/2/L33](https://doi.org/10.1088/2041-8205/727/2/L33)
- Guiriec, S., Daigne, F., Hascoët, R., et al. 2013, *ApJ*, 770, 32, doi: [10.1088/0004-637X/770/1/32](https://doi.org/10.1088/0004-637X/770/1/32)
- Guiriec, S., Kouveliotou, C., Daigne, F., et al. 2015, *ApJ*, 807, 148, doi: [10.1088/0004-637X/807/2/148](https://doi.org/10.1088/0004-637X/807/2/148)
- Hou, S.-J., Zhang, B.-B., Meng, Y.-Z., et al. 2018, *ApJ*, 866, 13, doi: [10.3847/1538-4357/aadc07](https://doi.org/10.3847/1538-4357/aadc07)
- Hu, Y.-D., Liang, E.-W., Xi, S.-Q., et al. 2014, *ApJ*, 789, 145, doi: [10.1088/0004-637X/789/2/145](https://doi.org/10.1088/0004-637X/789/2/145)
- Iyyani, S., Ryde, F., Burgess, J. M., Pe'er, A., & Bégué, D. 2016, *MNRAS*, 456, 2157, doi: [10.1093/mnras/stv2751](https://doi.org/10.1093/mnras/stv2751)
- Iyyani, S., Ryde, F., Axelsson, M., et al. 2013, *MNRAS*, 433, 2739, doi: [10.1093/mnras/stt863](https://doi.org/10.1093/mnras/stt863)
- Iyyani, S., Ryde, F., Ahlgren, B., et al. 2015, *MNRAS*, 450, 1651, doi: [10.1093/mnras/stv636](https://doi.org/10.1093/mnras/stv636)
- Kaneko, Y., Preece, R. D., Briggs, M. S., et al. 2006, *ApJS*, 166, 298, doi: [10.1086/505911](https://doi.org/10.1086/505911)
- Kass, R. E., & Raftery, A. E. 1995, *J Am Stat Assoc*, 90, 773
- Katz, J. I. 1994, *ApJ*, 422, 248, doi: [10.1086/173723](https://doi.org/10.1086/173723)
- Kumar, P., & McMahon, E. 2008, *MNRAS*, 384, 33, doi: [10.1111/j.1365-2966.2007.12621.x](https://doi.org/10.1111/j.1365-2966.2007.12621.x)
- Kumar, P., & Narayan, R. 2009, *MNRAS*, 395, 472, doi: [10.1111/j.1365-2966.2009.14539.x](https://doi.org/10.1111/j.1365-2966.2009.14539.x)
- Kumar, P., & Zhang, B. 2015, *PhR*, 561, 1, doi: [10.1016/j.physrep.2014.09.008](https://doi.org/10.1016/j.physrep.2014.09.008)
- Lazar, A., Nakar, E., & Piran, T. 2009, *ApJL*, 695, L10, doi: [10.1088/0004-637X/695/1/L10](https://doi.org/10.1088/0004-637X/695/1/L10)
- Lazzati, D., & Begelman, M. C. 2010, *ApJ*, 725, 1137, doi: [10.1088/0004-637X/725/1/1137](https://doi.org/10.1088/0004-637X/725/1/1137)
- Li, L., Wang, Y., Shao, L., et al. 2018a, *ApJS*, 234, 26, doi: [10.3847/1538-4365/aaa02a](https://doi.org/10.3847/1538-4365/aaa02a)
- Li, L., Wu, X.-F., Lei, W.-H., et al. 2018b, *ApJS*, 236, 26, doi: [10.3847/1538-4365/aabaf3](https://doi.org/10.3847/1538-4365/aabaf3)
- Li, L., Liang, E.-W., Tang, Q.-W., et al. 2012, *ApJ*, 758, 27, doi: [10.1088/0004-637X/758/1/27](https://doi.org/10.1088/0004-637X/758/1/27)
- Li, L., Wu, X.-F., Huang, Y.-F., et al. 2015, *ApJ*, 805, 13, doi: [10.1088/0004-637X/805/1/13](https://doi.org/10.1088/0004-637X/805/1/13)
- Liu, T., Gu, W.-M., Xue, L., & Lu, J.-F. 2007, *ApJ*, 661, 1025, doi: [10.1086/513689](https://doi.org/10.1086/513689)
- Liu, T., Gu, W.-M., & Zhang, B. 2017, *NewAR*, 79, 1, doi: [10.1016/j.newar.2017.07.001](https://doi.org/10.1016/j.newar.2017.07.001)
- Lloyd, N. M., & Petrosian, V. 2000, *ApJ*, 543, 722, doi: [10.1086/317125](https://doi.org/10.1086/317125)
- Lu, R.-J., Wei, J.-J., Liang, E.-W., et al. 2012, *ApJ*, 756, 112, doi: [10.1088/0004-637X/756/2/112](https://doi.org/10.1088/0004-637X/756/2/112)
- Lundman, C., Pe'er, A., & Ryde, F. 2013, *MNRAS*, 428, 2430, doi: [10.1093/mnras/sts219](https://doi.org/10.1093/mnras/sts219)
- Lyutikov, M., & Blandford, R. 2003, *arXiv Astrophysics e-prints*
- Malesani, D., Xu, D., Fynbo, J. P. U., et al. 2014, *GRB Coordinates Network, Circular Service*, No. 15800, #1 (2014), 15800
- Meegan, C., Lichti, G., Bhat, P. N., et al. 2009, *ApJ*, 702, 791, doi: [10.1088/0004-637X/702/1/791](https://doi.org/10.1088/0004-637X/702/1/791)
- Meng, Y.-Z., Geng, J.-J., Zhang, B.-B., et al. 2018, *ApJ*, 860, 72, doi: [10.3847/1538-4357/aac2d9](https://doi.org/10.3847/1538-4357/aac2d9)
- Meszáros, P., & Rees, M. J. 1993, *ApJ*, 405, 278, doi: [10.1086/172360](https://doi.org/10.1086/172360)
- Mészáros, P., & Rees, M. J. 2000, *ApJ*, 530, 292, doi: [10.1086/308371](https://doi.org/10.1086/308371)
- Meszáros, P., Rees, M. J., & Papatthanassiou, H. 1994, *ApJ*, 432, 181, doi: [10.1086/174559](https://doi.org/10.1086/174559)
- Murakami, T., Inoue, H., Nishimura, J., van Paradijs, J., & Fenimore, E. E. 1991, *Nature*, 350, 592, doi: [10.1038/350592a0](https://doi.org/10.1038/350592a0)
- Nappo, F., Pescalli, A., Oganessian, G., et al. 2017, *A&A*, 598, A23, doi: [10.1051/0004-6361/201628801](https://doi.org/10.1051/0004-6361/201628801)
- Nava, L., Ghirlanda, G., Ghisellini, G., & Celotti, A. 2011, *MNRAS*, 415, 3153, doi: [10.1111/j.1365-2966.2011.18928.x](https://doi.org/10.1111/j.1365-2966.2011.18928.x)
- Oganessian, G., Nava, L., Ghirlanda, G., & Celotti, A. 2017, *ApJ*, 846, 137, doi: [10.3847/1538-4357/aa831e](https://doi.org/10.3847/1538-4357/aa831e)
- Paczynski, B. 1986, *ApJL*, 308, L43, doi: [10.1086/184740](https://doi.org/10.1086/184740)
- Paczyński, B. 1998, in *American Institute of Physics Conference Series*, Vol. 428, *Gamma-Ray Bursts*, 4th Hunstville Symposium, ed. C. A. Meegan, R. D. Preece, & T. M. Koshut, 783–787

- Paczynski, B., & Xu, G. 1994, *ApJ*, 427, 708, doi: [10.1086/174178](https://doi.org/10.1086/174178)
- Pe'er, A. 2008, *ApJ*, 682, 463, doi: [10.1086/588136](https://doi.org/10.1086/588136)
- . 2015, *Advances in Astronomy*, 2015, 907321, doi: [10.1155/2015/907321](https://doi.org/10.1155/2015/907321)
- Pe'er, A., Mészáros, P., & Rees, M. J. 2007, *Philosophical Transactions of the Royal Society of London Series A*, 365, 1171, doi: [10.1098/rsta.2006.1986](https://doi.org/10.1098/rsta.2006.1986)
- Pe'er, A., & Ryde, F. 2017, *International Journal of Modern Physics D*, 26, 1730018, doi: [10.1142/S021827181730018X](https://doi.org/10.1142/S021827181730018X)
- Pe'er, A., Ryde, F., Wijers, R. A. M. J., Mészáros, P., & Rees, M. J. 2007, *ApJL*, 664, L1, doi: [10.1086/520534](https://doi.org/10.1086/520534)
- Pe'er, A., Zhang, B.-B., Ryde, F., et al. 2012, *MNRAS*, 420, 468, doi: [10.1111/j.1365-2966.2011.20052.x](https://doi.org/10.1111/j.1365-2966.2011.20052.x)
- Peng, F.-K., Liang, E.-W., Wang, X.-Y., et al. 2014, *ApJ*, 795, 155, doi: [10.1088/0004-637X/795/2/155](https://doi.org/10.1088/0004-637X/795/2/155)
- Piran, T., Shemi, A., & Narayan, R. 1993, *MNRAS*, 263, 861, doi: [10.1093/mnras/263.4.861](https://doi.org/10.1093/mnras/263.4.861)
- Popham, R., Woosley, S. E., & Fryer, C. 1999, *ApJ*, 518, 356, doi: [10.1086/307259](https://doi.org/10.1086/307259)
- Preece, R., Goldstein, A., Bhat, N., et al. 2016, *ApJ*, 821, 12, doi: [10.3847/0004-637X/821/1/12](https://doi.org/10.3847/0004-637X/821/1/12)
- Preece, R. D., Briggs, M. S., Mallozzi, R. S., et al. 1998, *ApJL*, 506, L23, doi: [10.1086/311644](https://doi.org/10.1086/311644)
- . 2000, *ApJS*, 126, 19, doi: [10.1086/313289](https://doi.org/10.1086/313289)
- Preparata, G., Ruffini, R., & Xue, S.-S. 1998, *A&A*, 338, L87
- . 2002, *arXiv Astrophysics e-prints*
- Racusin, J. L., Oates, S. R., Schady, P., et al. 2011, *ApJ*, 738, 138, doi: [10.1088/0004-637X/738/2/138](https://doi.org/10.1088/0004-637X/738/2/138)
- Rees, M. J., & Meszaros, P. 1994, *ApJL*, 430, L93, doi: [10.1086/187446](https://doi.org/10.1086/187446)
- Rees, M. J., & Mészáros, P. 2005, *ApJ*, 628, 847, doi: [10.1086/430818](https://doi.org/10.1086/430818)
- Ruffini, R., Salmonson, J. D., Wilson, J. R., & Xue, S.-S. 1999, *A&A*, 350, 334
- . 2000, *A&A*, 359, 855
- Ryan, G., van Eerten, H., MacFadyen, A., & Zhang, B.-B. 2015, *ApJ*, 799, 3, doi: [10.1088/0004-637X/799/1/3](https://doi.org/10.1088/0004-637X/799/1/3)
- Ryde, F. 2005, *ApJL*, 625, L95, doi: [10.1086/431239](https://doi.org/10.1086/431239)
- Ryde, F., & Pe'er, A. 2009, *ApJ*, 702, 1211, doi: [10.1088/0004-637X/702/2/1211](https://doi.org/10.1088/0004-637X/702/2/1211)
- Ryde, F., Axelsson, M., Zhang, B. B., et al. 2010, *ApJL*, 709, L172, doi: [10.1088/2041-8205/709/2/L172](https://doi.org/10.1088/2041-8205/709/2/L172)
- Sari, R., Narayan, R., & Piran, T. 1996, *ApJ*, 473, 204, doi: [10.1086/178136](https://doi.org/10.1086/178136)
- Sari, R., Piran, T., & Narayan, R. 1998, *ApJL*, 497, L17, doi: [10.1086/311269](https://doi.org/10.1086/311269)
- Scargle, J. D., Norris, J. P., Jackson, B., & Chiang, J. 2013, *ApJ*, 764, 167, doi: [10.1088/0004-637X/764/2/167](https://doi.org/10.1088/0004-637X/764/2/167)
- Schaefer, B. E. 2003, *ApJL*, 583, L71, doi: [10.1086/368106](https://doi.org/10.1086/368106)
- Schwarz, G. 1978, *Annals of Statistics*, 6, 461
- Shemi, A., & Piran, T. 1990, *ApJL*, 365, L55, doi: [10.1086/185887](https://doi.org/10.1086/185887)
- Tang, Q.-W., Wang, X.-Y., & Liu, R.-Y. 2017, *ApJ*, 844, 56, doi: [10.3847/1538-4357/aa7a58](https://doi.org/10.3847/1538-4357/aa7a58)
- Thompson, C. 1994, *MNRAS*, 270, 480, doi: [10.1093/mnras/270.3.480](https://doi.org/10.1093/mnras/270.3.480)
- Toma, K., Wu, X.-F., & Mészáros, P. 2011, *MNRAS*, 415, 1663, doi: [10.1111/j.1365-2966.2011.18807.x](https://doi.org/10.1111/j.1365-2966.2011.18807.x)
- Toma, K., Sakamoto, T., Zhang, B., et al. 2009, *ApJ*, 698, 1042, doi: [10.1088/0004-637X/698/2/1042](https://doi.org/10.1088/0004-637X/698/2/1042)
- Troja, E., Rosswog, S., & Gehrels, N. 2010, *ApJ*, 723, 1711, doi: [10.1088/0004-637X/723/2/1711](https://doi.org/10.1088/0004-637X/723/2/1711)
- Troja, E., Lipunov, V. M., Mundell, C. G., et al. 2017, *Nature*, 547, 425, doi: [10.1038/nature23289](https://doi.org/10.1038/nature23289)
- Uhm, Z. L., & Zhang, B. 2014, *Nature Physics*, 10, 351, doi: [10.1038/nphys2932](https://doi.org/10.1038/nphys2932)
- Vereshchagin, G. V. 2014, *International Journal of Modern Physics D*, 23, 1430003, doi: [10.1142/S0218271814300031](https://doi.org/10.1142/S0218271814300031)
- Vianello, G., Lauer, R. J., Younk, P., et al. 2015, *arXiv e-prints*, <https://arxiv.org/abs/1507.08343>
- Wang, Y.-Z., Wang, H., Zhang, S., et al. 2017, *ApJ*, 836, 81, doi: [10.3847/1538-4357/aa56c6](https://doi.org/10.3847/1538-4357/aa56c6)
- Wei, J.-J., Zhang, B.-B., Shao, L., Wu, X.-F., & Mészáros, P. 2017, *ApJL*, 834, L13, doi: [10.3847/2041-8213/834/2/L13](https://doi.org/10.3847/2041-8213/834/2/L13)
- Wygoda, N., Guetta, D., Mandich, M. A., & Waxman, E. 2016, *ApJ*, 824, 127, doi: [10.3847/0004-637X/824/2/127](https://doi.org/10.3847/0004-637X/824/2/127)

- Xiao, D., Peng, Z.-k., Zhang, B.-B., & Dai, Z.-G. 2018, *ApJ*, 867, 52,
doi: [10.3847/1538-4357/aae52f](https://doi.org/10.3847/1538-4357/aae52f)
- Xu, M., & Huang, Y. F. 2012, *A&A*, 538, A134,
doi: [10.1051/0004-6361/201117754](https://doi.org/10.1051/0004-6361/201117754)
- Xue, L., Liu, T., Gu, W.-M., & Lu, J.-F. 2013, *ApJS*, 207, 23,
doi: [10.1088/0067-0049/207/2/23](https://doi.org/10.1088/0067-0049/207/2/23)
- Yu, H.-F., Dereli-Bégué, H., & Ryde, F. 2018, arXiv e-prints,
<https://arxiv.org/abs/1810.07313>
- Yu, H.-F., Preece, R. D., Greiner, J., et al. 2016, *A&A*, 588, A135,
doi: [10.1051/0004-6361/201527509](https://doi.org/10.1051/0004-6361/201527509)
- Zhang, B. 2011, *Comptes Rendus Physique*, 12, 206, doi: [10.1016/j.crhy.2011.03.004](https://doi.org/10.1016/j.crhy.2011.03.004)
- . 2014, *International Journal of Modern Physics D*, 23, 1430002,
doi: [10.1142/S021827181430002X](https://doi.org/10.1142/S021827181430002X)
- Zhang, B., & Yan, H. 2011, *ApJ*, 726, 90,
doi: [10.1088/0004-637X/726/2/90](https://doi.org/10.1088/0004-637X/726/2/90)
- Zhang, B.-B., van Eerten, H., Burrows, D. N., et al. 2015, *ApJ*, 806, 15,
doi: [10.1088/0004-637X/806/1/15](https://doi.org/10.1088/0004-637X/806/1/15)
- Zhang, B.-B., Zhang, B., Liang, E.-W., et al. 2011, *ApJ*, 730, 141,
doi: [10.1088/0004-637X/730/2/141](https://doi.org/10.1088/0004-637X/730/2/141)
- Zhang, B.-B., Zhang, B., Castro-Tirado, A. J., et al. 2018, *Nature Astronomy*, 2, 69,
doi: [10.1038/s41550-017-0309-8](https://doi.org/10.1038/s41550-017-0309-8)
- Zhang, S.-N., Kole, M., Bao, T.-W., et al. 2019, *Nature Astronomy*,
doi: [10.1038/s41550-018-0664-0](https://doi.org/10.1038/s41550-018-0664-0)

Table 1. Results of the Time-integrated Spectral Fits of Our Total Sample

Burst ID	$t_1 \sim t_2$ (s)	Sequence	α	E_c (keV)	Model	Detector	Selected by	$-\ln(\text{likelihood})/\text{dof}$
(1)	(2)	(3)	(4)	(5)	(6)	(7)	(8)	(9)
081009140	0.0~8.0	1st	$-1.12^{+0.03}_{-0.03}$	55^{+18}_{-17}	CPL	n3,b1	PeakFlux	1134/212
081009140	36.0~50.0	2nd	$-1.50^{+0.70}_{-0.70}$	19^{+14}_{-8}	CPL	n3,b1	PeakFlux	1248/212
081215784	0.0~2.9	1st	$-0.72^{+0.18}_{-0.18}$	688^{+40}_{-35}	CPL	n9,na,nb,b1	PeakFlux	1838/438
081215784	2.9~4.4	2nd	$-0.58^{+0.04}_{-0.04}$	210^{+15}_{-14}	CPL	n9,na,nb,b1	PeakFlux	1295/438
081215784	4.4~8.0	3rd	$-0.75^{+0.03}_{-0.03}$	250^{+16}_{-15}	CPL	n9,na,nb,b1	PeakFlux	1844/438
090618353	0.0~45.0	1st	$-0.87^{+0.09}_{-0.09}$	154^{+26}_{-22}	CPL	n4,b0	PeakFlux	1659/212
090618353	45.0~76.0	2nd	$-1.03^{+0.02}_{-0.02}$	241^{+11}_{-10}	CPL	n4,b0	PeakFlux	1606/212
090618353	76.0~103.0	3rd	$-1.11^{+0.02}_{-0.02}$	141^{+6}_{-6}	CPL	n4,b0	PeakFlux	1494/212
090618353	103.0~116.0	4th	$-1.33^{+0.06}_{-0.06}$	100^{+12}_{-11}	CPL	n4,b0	PeakFlux	1246/212
090926181	0.0~8.0	1st	$-0.60^{+0.01}_{-0.01}$	267^{+6}_{-6}	CPL	n3,n6,n7,b1	Fluence	2202/343
090926181	8.0~20.0	2nd	$-0.89^{+0.01}_{-0.01}$	225^{+6}_{-6}	CPL	n3,n6,n7,b1	Fluence	2266/343
091127976	0.0~1.0	1st	$-1.15^{+0.03}_{-0.03}$	108^{+7}_{-6}	CPL	n6,n7,n9,b1	PeakFlux	905/341
091127976	1.0~2.0	2nd	$-1.37^{+0.03}_{-0.03}$	276^{+32}_{-28}	CPL	n6,n7,n9,b1	PeakFlux	881/341
091127976	6.5~8.5	3rd	$-1.89^{+0.08}_{-0.08}$	60^{+9}_{-8}	CPL	n6,n7,n9,b1	PeakFlux	1112/341
100719989	0.0~3.4	1st	$-0.34^{+0.04}_{-0.04}$	235^{+17}_{-16}	CPL	n4,n5,b0	PeakFlux	1015/228
100719989	3.4~10.0	2nd	$-0.51^{+0.04}_{-0.04}$	148^{+10}_{-9}	CPL	n4,n5,b0	PeakFlux	1197/228
100719989	20.0~24.0	3rd	$-0.85^{+0.11}_{-0.11}$	230^{+60}_{-50}	CPL	n4,n5,b0	PeakFlux	945/228
100826957	-1.0~50.0	1st	$-0.79^{+0.02}_{-0.02}$	323^{+22}_{-20}	CPL	n7,n8,b1	Fluence	2146/230
100826957	58.0~110.0	2nd	$-1.12^{+0.03}_{-0.03}$	278^{+32}_{-29}	CPL	n7,n8,b1	Fluence	2034/230
100829876	0.0~1.4	1st	$-0.42^{+0.07}_{-0.07}$	113^{+11}_{-10}	CPL	n2,b0	PeakFlux	805/221
100829876	1.4~1.9	2nd	$-0.69^{+0.11}_{-0.11}$	200^{+50}_{-40}	CPL	n2,b0	PeakFlux	577/199
101014175	0.0~16.0	1st	$-0.98^{+0.01}_{-0.01}$	200^{+8}_{-7}	CPL	n6,n7,b1	Fluence	2108/325
101014175	16.0~40.0	2nd	$-1.38^{+0.02}_{-0.02}$	280^{+25}_{-23}	CPL	n6,n7,b1	Fluence	2242/325
101014175	98.0~120.0	3rd	$-1.15^{+0.05}_{-0.05}$	162^{+20}_{-18}	CPL	n6,n7,b1	Fluence	2234/325
101014175	155.0~170.0	4th	$-1.12^{+0.08}_{-0.08}$	370^{+159}_{-110}	CPL	n6,n7,b1	Fluence	2056/324
101014175	195.0~230.0	4th	$-0.88^{+0.29}_{-0.29}$	390^{+140}_{-40}	CPL	n6,n7,b1	Fluence	2600/324
110301214	0.0~3.5	1st	$-0.81^{+0.02}_{-0.02}$	108^{+3}_{-3}	CPL	n7,n8,nb,b1	PeakFlux	1686/341
110301214	3.7~8.0	2nd	$-1.11^{+0.03}_{-0.03}$	103^{+5}_{-5}	CPL	n7,n8,nb,b1	PeakFlux	1755/341
110625881	-1.0~9.7	1st	$-0.66^{+0.12}_{-0.12}$	193^{+40}_{-34}	CPL	n7,n8,nb,b1	PeakFlux	2556/439
110625881	9.7~18.0	2nd	$-0.87^{+0.03}_{-0.03}$	204^{+15}_{-14}	CPL	n7,n8,nb,b1	PeakFlux	2492/439
110625881	20.0~27.0	3rd	$-0.79^{+0.02}_{-0.02}$	142^{+5}_{-5}	CPL	n7,n8,nb,b1	PeakFlux	2455/439
110625881	27.0~32.0	4th	$-1.04^{+0.04}_{-0.04}$	179^{+15}_{-14}	CPL	n7,n8,b1	PeakFlux	2128/439
110825102	0.0~14.0	1st	$-1.21^{+0.05}_{-0.05}$	182^{+22}_{-20}	CPL	n3,n6,n7,b1	PeakFlux	2341/342
110825102	14.0~21.0	2nd	$-0.91^{+0.02}_{-0.02}$	260^{+14}_{-13}	CPL	n3,n6,n7,b1	PeakFlux	2122/342

Table 1 continued on next page

Table 1 (continued)

Burst ID	$t_1 \sim t_2$ (s)	Sequence	α	E_c (keV)	Model	Detector	Selected by	$-\ln(\text{likelihood})/\text{dof}$
(1)	(2)	(3)	(4)	(5)	(6)	(7)	(8)	(9)
110903009	0.0~2.7	1st	$-1.30^{+0.23}_{-0.23}$	54^{+19}_{-14}	CPL	n2,n5,b0	PeakFlux	1408/326
110903009	2.7~7.0	2nd	$-1.36^{+0.11}_{-0.11}$	33^{+4}_{-3}	CPL	n2,n5,b0	PeakFlux	1551/326
110903009	19.9~28.0	3rd	$-1.42^{+0.08}_{-0.08}$	270^{+10}_{-70}	CPL	n2,n5,b0	PeakFlux	1860/326
120204054	1.0~40.0	1st	$-0.95^{+0.03}_{-0.03}$	172^{+11}_{-10}	CPL	n0,n1,n3,b0	PeakFlux	2616/441
120204054	40.0~52.0	2nd	$-1.19^{+0.02}_{-0.02}$	240^{+17}_{-15}	CPL	n0,n1,n3,b0	PeakFlux	3765/441
120328268	0.0~16.8	1st	$-0.78^{+0.02}_{-0.02}$	222^{+12}_{-11}	CPL	n7,n9,nb,b1	PeakFlux	3111/437
120328268	16.8~40.0	2nd	$-1.02^{+0.03}_{-0.03}$	198^{+14}_{-13}	CPL	n7,n9,nb,b1	PeakFlux	3214/437
120728434	-1.0~4.0	1st	$-0.69^{+0.27}_{-0.27}$	120^{+60}_{-40}	CPL	n1,n2,n5,b0	Fluence	2203/438
120728434	4.0~55.0	2nd	$-0.12^{+0.05}_{-0.05}$	53^{+2}_{-2}	CPL	n1,n2,n5,b0	Fluence	6463/438
120728434	65.0~95.0	3rd	$-0.26^{+0.04}_{-0.04}$	447^{+14}_{-14}	CPL	n1,n2,n5,b0	Fluence	5956/438
130504978	0.0~22.0	1st	$-0.94^{+0.02}_{-0.02}$	810^{+80}_{-80}	CPL	n2,n9,na,b1	Fluence	3020/440
130504978	22.0~42.0	2nd	$-1.15^{+0.02}_{-0.02}$	700^{+80}_{-70}	CPL	n2,n9,na,b1	Fluence	2919/440
130504978	45.0~59.0	3rd	$-1.48^{+0.05}_{-0.05}$	830^{+400}_{-280}	CPL	n2,n9,na,b1	Fluence	2596/440
130504978	59.0~74.0	4th	$-1.22^{+0.02}_{-0.02}$	640^{+80}_{-70}	CPL	n2,n9,na,b1	Fluence	2739/440
130504978	74.0~84.0	5th	$-1.39^{+0.07}_{-0.07}$	260^{+70}_{-60}	CPL	n2,n9,na,b1	Fluence	2361/440
130606497	0.0~12.0	1st	$-0.87^{+0.02}_{-0.02}$	580^{+40}_{-40}	CPL	n7,n8,b1	Fluence	1509/228
130606497	12.0~22.0	2nd	$-1.33^{+0.01}_{-0.01}$	3100^{+700}_{-600}	CPL	n7,n8,b1	Fluence	1454/228
130606497	35.0~48.0	3rd	$-1.04^{+0.02}_{-0.02}$	290^{+20}_{-18}	CPL	n7,n8,b1	Fluence	1438/228
130606497	48.0~63.0	4th	$-0.92^{+0.03}_{-0.03}$	207^{+12}_{-11}	CPL	n7,n8,b1	Fluence	1484/228
131127592	0.0~5.4	1st	$-1.03^{+0.03}_{-0.03}$	309^{+28}_{-26}	CPL	n1,n2,n5,b0	PeakFlux	2132/442
131127592	5.4~15.5	2nd	$-1.15^{+0.03}_{-0.03}$	241^{+18}_{-16}	CPL	n1,n2,n5,b0	PeakFlux	2523/442
131127592	15.5~20.0	3rd	$-1.01^{+0.04}_{-0.04}$	135^{+11}_{-10}	CPL	n1,n2,n5,b0	PeakFlux	2040/442
140206275	0.0~4.7	1st	$0.23^{+0.10}_{-0.10}$	109^{+11}_{-10}	CPL	n0,n1,n3,b0	PeakFlux	1902/441
140206275	4.7~25.0	2nd	$-0.86^{+0.01}_{-0.01}$	349^{+14}_{-13}	CPL	n0,n1,n3,b0	PeakFlux	3136/441
140206275	25.0~50.0	3rd	$-1.21^{+0.03}_{-0.03}$	219^{+17}_{-15}	CPL	n0,n1,n3,b0	PeakFlux	3065/441
140213807	-1.0~5.0	1st	$-1.19^{+0.03}_{-0.03}$	255^{+24}_{-22}	CPL	n0,n1,b0	PeakFlux	2356/442
140213807	5.0~12.0	2nd	$-1.15^{+0.04}_{-0.04}$	83^{+5}_{-5}	CPL	n0,n1,b0	PeakFlux	2454/442
140329295	-1.0~1.6	1st	$-0.59^{+0.14}_{-0.14}$	114^{+24}_{-20}	CPL	n8,nb,b1	PeakFlux	1101/326
140329295	19.0~22.8	2nd	$-0.77^{+0.03}_{-0.03}$	203^{+11}_{-10}	CPL	n8,nb,b1	PeakFlux	1428/326
140329295	22.8~28.7	3rd	$-0.86^{+0.02}_{-0.02}$	227^{+9}_{-9}	CPL	n8,nb,b1	PeakFlux	1687/326
140416060	-1.0~5.4	1st	$-1.14^{+0.07}_{-0.07}$	123^{+16}_{-14}	CPL	n2,b0	PeakFlux	989/225
140416060	5.4~18.0	2nd	$-1.20^{+0.04}_{-0.04}$	144^{+11}_{-10}	CPL	n2,b0	PeakFlux	1221/225
140416060	18.0~50.0	3rd	$-1.26^{+0.06}_{-0.06}$	148^{+19}_{-17}	CPL	n2,b0	PeakFlux	1513/225
140508128	0.0~10.0	1st	$-0.91^{+0.03}_{-0.03}$	325^{+28}_{-26}	CPL	na,b1	PeakFlux	1200/211
140508128	23.0~29.0	2nd	$-0.72^{+0.05}_{-0.05}$	152^{+15}_{-14}	CPL	na,b1	PeakFlux	1011/211
140508128	38.0~42.0	3rd	$-1.23^{+0.07}_{-0.07}$	200^{+40}_{-40}	CPL	na,b1	PeakFlux	878/211

Table 1 continued on next page

Table 1 (*continued*)

Burst ID	$t_1 \sim t_2$ (s)	Sequence	α	E_c (keV)	Model	Detector	Selected by	$-\ln(\text{likelihood})/\text{dof}$
(1)	(2)	(3)	(4)	(5)	(6)	(7)	(8)	(9)
140508128	46.5~48.2	4th	$-0.51^{+0.20}_{-0.20}$	51^{+11}_{-9}	CPL	na,b1	PeakFlux	577/211
140523129	0.0~2.6	1st	$-0.64^{+0.05}_{-0.05}$	292^{+35}_{-31}	CPL	n3,n4,n5,b0	PeakFlux	1809/442
140523129	2.6~6.5	2nd	$-0.53^{+0.04}_{-0.04}$	237^{+17}_{-16}	CPL	n3,n4,n5,b0	PeakFlux	2088/442
140523129	6.5~11.7	3rd	$-0.82^{+0.03}_{-0.03}$	185^{+11}_{-10}	CPL	n3,n4,n5,b0	PeakFlux	2240/442
140523129	11.7~23.0	4th	$-1.20^{+0.04}_{-0.04}$	120^{+11}_{-10}	CPL	n3,n4,n5,b0	PeakFlux	2681/442
140810782	0.0~20.0	1st	$-0.67^{+0.07}_{-0.07}$	207^{+30}_{-27}	CPL	n2,n5,b0	Fluence	2335/327
140810782	20.0~41.0	2nd	$-0.66^{+0.05}_{-0.05}$	278^{+29}_{-26}	CPL	n2,n5,b0	Fluence	2428/327
140810782	42.0~55.0	3rd	$-0.76^{+0.04}_{-0.04}$	171^{+14}_{-13}	CPL	n2,n5,b0	Fluence	2165/327
150118409	0.0~40.0	1st	$-0.94^{+0.01}_{-0.01}$	631^{+35}_{-33}	CPL	n1,n2,n5,b0	PeakFlux	3555/441
150118409	40.0~52.0	2nd	$-0.88^{+0.03}_{-0.03}$	580^{+50}_{-50}	CPL	n1,n2,n5,b0	PeakFlux	2714/441
150201574	0.0~4.2	1st	$-0.81^{+0.02}_{-0.02}$	161^{+6}_{-6}	CPL	n3,n4,b0	PeakFlux	1591/316
150201574	4.2~8.5	2nd	$-1.03^{+0.02}_{-0.02}$	119^{+4}_{-4}	CPL	n3,n4,b0	PeakFlux	2180/316
150330828	-1.0~10.0	1st	$-0.30^{+0.08}_{-0.08}$	190^{+22}_{-20}	CPL	n1,n2,n5,b0	PeakFlux	2600/444
150330828	123.5~142.2	2nd	$-0.95^{+0.01}_{-0.01}$	330^{+11}_{-10}	CPL	n1,n2,n5,b0	PeakFlux	3178/444
150330828	142.2~155.0	3rd	$-1.10^{+0.02}_{-0.02}$	214^{+13}_{-12}	CPL	n1,n2,n5,b0	PeakFlux	2737/444
151227218	0.0~4.2	1st	$-1.02^{+0.08}_{-0.08}$	250^{+60}_{-50}	CPL	n1,n2,n5,b0	PeakFlux	1883/442
151227218	20.0~39.0	2nd	$-1.26^{+0.02}_{-0.02}$	530^{+50}_{-50}	CPL	n1,n2,n5,b0	PeakFlux	2978/442
151227218	42.0~46.0	3rd	$-1.25^{+0.08}_{-0.08}$	190^{+50}_{-40}	CPL	n1,n2,n5,b0	PeakFlux	1856/442
160422499	0.0~3.1	1st	$-1.17^{+0.02}_{-0.02}$	378^{+26}_{-24}	CPL	n0,n1,n5,b0	PeakFlux	1878/440
160422499	3.2~15.0	2nd	$-0.93^{+0.01}_{-0.01}$	225^{+6}_{-6}	CPL	n0,n1,n5,b0	PeakFlux	2887/440
160509374	-1.0~5.0	1st	$-1.12^{+0.08}_{-0.08}$	500^{+200}_{-140}	CPL	n0,n1,n3,b0	Fluence	2015/443
160509374	5.0~30.0	2nd	$-0.89^{+0.01}_{-0.01}$	382^{+10}_{-10}	CPL	n0,n1,n3,b0	Fluence	3509/443
160625945	0.0~2.0	1st	$-0.29^{+0.13}_{-0.13}$	40^{+4}_{-4}	CPL	n6,n7,n9,b1	PeakFlux	1400/439
160625945	180.0~192.0	2nd	$-0.68^{+0.01}_{-0.01}$	565^{+12}_{-12}	CPL	n6,n7,n9,b1	PeakFlux	4308/439
160625945	192.0~198.0	3rd	$-0.63^{+0.01}_{-0.01}$	324^{+5}_{-5}	CPL	n6,n7,n9,b1	PeakFlux	3318/439
160625945	198.0~215.0	4th	$-0.71^{+0.01}_{-0.01}$	352^{+6}_{-6}	CPL	n6,n7,n9,b1	PeakFlux	3947/439
160802259	0.0~7.0	1st	$-0.53^{+0.03}_{-0.03}$	210^{+10}_{-10}	CPL	n2,b0	PeakFlux	1220/225
160802259	14.0~20.0	2nd	$-0.88^{+0.06}_{-0.06}$	126^{+15}_{-14}	CPL	n2,b0	PeakFlux	1099/225
160816730	0.0~7.0	1st	$-0.80^{+0.04}_{-0.04}$	163^{+12}_{-11}	CPL	n6,n7,n9,b1	PeakFlux	2169/441
160816730	7.0~17.0	2nd	$-0.64^{+0.03}_{-0.03}$	182^{+9}_{-8}	CPL	n6,n7,n9,b1	PeakFlux	2430/441
170808936	0.0~13.5	1st	$-0.88^{+0.01}_{-0.01}$	2350^{+9}_{-8}	CPL	n1,n2,n5,b0	Fluence+Peak	2729/442
170808936	13.5~20.0	2nd	$-0.98^{+0.01}_{-0.01}$	280^{+9}_{-9}	CPL	n1,n2,n5,b0	Fluence+Peak	2328/442
171102107	-2.0~3.0	1st	$-0.48^{+0.19}_{-0.19}$	37^{+7}_{-6}	CPL	n0,n1,n2,b0	Fluence	2061/442
171102107	3.0~10.0	2nd	$-1.05^{+0.29}_{-0.29}$	160^{+17}_{-80}	CPL	n0,n1,n2,b0	Fluence	2264/442
171102107	25.0~42.0	3rd	$-1.22^{+0.09}_{-0.09}$	530^{+300}_{-190}	CPL	n0,n1,n2,b0	Fluence	2869/442
171102107	42.0~62.0	4th	$-0.83^{+0.03}_{-0.03}$	141^{+8}_{-7}	CPL	n0,n1,n2,b0	Fluence	3083/442

Table 1 continued on next page

Table 1 (*continued*)

Burst ID	$t_1 \sim t_2$	Sequence	α	E_c	Model	Detector	Selected by	$-\ln(\text{likelihood})/\text{dof}$
(1)	(s)	(3)	(4)	(keV)	(6)	(7)	(8)	(9)
171119992	0.0~20.0	1st	$-0.93^{+0.20}_{-0.20}$	290^{+150}_{-100}	CPL	n2,b0	PeakFlux	1399/225
171119992	20.0~35.0	2nd	$-1.21^{+0.24}_{-0.24}$	210^{+160}_{-90}	CPL	n2,b0	PeakFlux	1301/225
171120556	0.0~7.0	1st	$-0.86^{+0.07}_{-0.07}$	209^{+35}_{-30}	CPL	n0,n1,n3,b0	PeakFlux	2371/442
171120556	15.4~20.0	2nd	$-1.50^{+0.00}_{-0.00}$	125^{+1}_{-1}	CPL	n0,n1,n3,b0	PeakFlux	2001/442
171227000	0.0~24.0	1st	$-0.71^{+0.01}_{-0.01}$	884^{+30}_{-29}	CPL	n5,b0	PeakFlux	1687/223
171227000	24.0~60.0	2nd	$-1.05^{+0.03}_{-0.03}$	346^{+34}_{-31}	CPL	n5,b0	PeakFlux	1580/223
180113011	0.0~2.8	1st	$-0.83^{+0.03}_{-0.03}$	630^{+70}_{-60}	CPL	n3,n4,b0	PeakFlux	1342/326
180113011	2.8~5.4	2nd	$-0.75^{+0.04}_{-0.04}$	460^{+50}_{-50}	CPL	n3,n4,b0	PeakFlux	1328/326
180113418	0.0~19.6	1st	$-0.73^{+0.01}_{-0.01}$	388^{+12}_{-11}	CPL	n1,n2,n9,b0	PeakFlux	3402/443
180113418	19.6~33.2	2nd	$-0.74^{+0.02}_{-0.02}$	223^{+9}_{-8}	CPL	n1,n2,n9,b0	PeakFlux	2930/443
180120207	0.0~13.0	1st	$-0.96^{+0.02}_{-0.02}$	147^{+6}_{-6}	CPL	n9,na,nb,b1	PeakFlux	2830/438
180120207	13.0~30.0	2nd	$-1.19^{+0.02}_{-0.02}$	160^{+7}_{-7}	CPL	n9,na,nb,b1	PeakFlux	2998/438

Table 2. Results of the Time-resolved Spectral Fits of GRB 140206B

$t_1 \sim t_2$	S/N	Blackbody Fitting				Cutoff Power-Law Fitting				Band Function Fitting			
		kT (keV)	$-\ln(\text{posterior})/\text{AIC}/\text{BIC}/\text{DIC}$	α	E_c (keV)	$-\ln(\text{posterior})/\text{AIC}/\text{BIC}/\text{DIC}$	E_c (keV)	E_{pk} (keV)	β	$-\ln(\text{posterior})/\text{AIC}/\text{BIC}/\text{DIC}$			
1st													
-1.00~-0.04	2.73	
-0.04~-0.46	13.87	$55.23^{+2.52}_{-2.48}$	-599/1202/1210/1231	$0.53^{+0.12}_{-0.11}$	$93.5^{+5.0}_{-5.4}$	-609/1225/1237/1212	$256.2^{+19.2}_{-18.9}$	$-6.77^{+2.20}_{-2.24}$	-614/1237/1253/1227				
0.46~-1.81	9.94	$45.05^{+2.71}_{-2.73}$	-1179/2361/2369/2391	$0.35^{+0.15}_{-0.14}$	$88.5^{+8.4}_{-8.3}$	-1191/2388/2401/2370	$206.2^{+30.6}_{-34.0}$	$5.47^{+2.94}_{-3.07}$	-1196/2400/2416/2370				
1.81~-4.70	5.50	$44.15^{+3.26}_{-3.18}$	-1676/3356/3364/3387	$0.23^{+0.20}_{-0.19}$	$87.3^{+9.4}_{-9.8}$	-1692/3390/3403/3376	$444.4^{+123.6}_{-269.4}$	$-5.78^{+2.69}_{-2.81}$	-1696/3399/3416/2851				
2nd													
4.70~5.81	2.58				
5.81~7.63	17.32				
7.63~8.79	24.76				
8.79~11.84	59.56				
11.84~12.57	38.80				
12.57~13.24	54.54				
13.24~14.60	94.85				
14.60~15.82	76.58				
15.82~17.34	68.64				
17.34~18.84	56.33				
18.84~19.62	31.30				
19.62~25.00	60.64				
3rd													
25.00~27.66	36.38				
27.66~29.21	41.52				
29.21~31.53	62.81				
31.53~33.11	39.98				
33.11~34.99	33.28				
34.99~38.15	33.63				
38.15~43.48	30.88				
43.48~50.00	13.14				

MULTIPULSE *Fermi* GAMMA-RAY BURST

Table 3. Results of the Time-resolved Spectral Fits of GRB 140329B

$t_1 \sim t_2$ (s)	S/N	Blackbody Fitting		Cutoff Power-Law Fitting		
		kT (keV)	$-\ln(\text{posterior})/\text{AIC}/\text{BIC}/\text{DIC}$	α	E_c (keV)	$-\ln(\text{posterior})/\text{AIC}/\text{BIC}/\text{DIC}$
The 1st Sub-Burst						
-1.00~-0.12	0.69
-0.12~-0.01	8.09
-0.01~0.25	39.54	$40.15^{+1.00}_{-1.00}$	-509/1022/1030/1037	$-0.47^{+0.07}_{-0.07}$	$160.1^{+14.9}_{-14.8}$	-377/760/771/747
0.25~0.47	20.46	$20.62^{+0.80}_{-0.81}$	-221/446/454/458	$-0.56^{+0.17}_{-0.16}$	$76.7^{+13.5}_{-13.7}$	-202/409/421/392
0.47~0.67	9.51	$13.75^{+1.79}_{-1.81}$	-145/294/302/303	Unconstrained	Unconstrained	Unconstrained
0.67~3.00	4.17	$12.19^{+2.42}_{-2.43}$	-1114/2231/2239/2237	Unconstrained	Unconstrained	Unconstrained
The 2nd Sub-Burst						
19.00~19.53	2.97
19.53~20.06	31.94	$-0.97^{+0.05}_{-0.05}$	$734.8^{+138.2}_{-138.4}$	-561/1128/1140/1112
20.06~20.93	56.75	$-0.86^{+0.04}_{-0.04}$	$282.7^{+24.3}_{-24.3}$	-848/1702/1714/1688
20.93~21.17	41.04	$-0.96^{+0.06}_{-0.06}$	$293.0^{+38.3}_{-39.3}$	-321/647/659/632
21.17~22.33	110.39	$-0.91^{+0.02}_{-0.02}$	$266.0^{+13.0}_{-13.2}$	-1171/2348/2360/2334
22.33~22.77	52.77	$-1.00^{+0.04}_{-0.04}$	$256.8^{+25.9}_{-25.4}$	-557/1120/1132/1105
22.77~22.80	19.71
The 3rd Sub-Burst						
22.80~23.64	94.55	$-0.93^{+0.02}_{-0.02}$	$325.6^{+18.6}_{-18.8}$	-982/1970/1982/1955
23.64~23.95	92.21	$-0.75^{+0.03}_{-0.03}$	$440.5^{+25.5}_{-25.7}$	-613/1232/1244/1217
23.95~24.10	59.71	$-0.86^{+0.04}_{-0.04}$	$405.0^{+36.7}_{-37.3}$	-308/622/634/606
24.10~24.14	38.36	$-0.67^{+0.07}_{-0.07}$	$312.0^{+40.3}_{-41.0}$	-22/49/61/33
24.14~24.34	76.44	$-0.90^{+0.03}_{-0.03}$	$389.9^{+32.9}_{-32.7}$	-408/822/833/805
24.34~24.61	73.29	$-0.86^{+0.04}_{-0.04}$	$268.7^{+20.0}_{-20.0}$	-457/919/931/904
24.61~25.00	71.01	$-0.94^{+0.04}_{-0.04}$	$266.2^{+22.2}_{-22.2}$	-579/1164/1176/1149
25.00~25.28	47.44	$-1.01^{+0.06}_{-0.05}$	$242.6^{+30.7}_{-30.4}$	-371/749/760/733
25.28~25.86	52.16	$-1.12^{+0.05}_{-0.05}$	$217.5^{+25.2}_{-26.0}$	-591/1188/1200/1172
25.86~26.59	43.36	$-1.02^{+0.07}_{-0.07}$	$161.5^{+21.3}_{-21.1}$	-684/1374/1386/1359
26.59~27.63	34.66	$-1.16^{+0.08}_{-0.08}$	$168.0^{+28.4}_{-28.4}$	-768/1542/1553/1526
27.63~28.70	20.92	$-1.16^{+0.15}_{-0.15}$	$127.6^{+33.9}_{-37.0}$	-785/1576/1588/1550

Table 4. Results of the Time-resolved Spectral Fits of GRB 150330A

$t_1 \sim t_2$ (s)	S/N	Blackbody Fitting		Cutoff Power-Law Fitting		
		kT (keV)	$-\ln(\text{posterior})/\text{AIC}/\text{BIC}/\text{DIC}$	α	E_c (keV)	$-\ln(\text{posterior})/\text{AIC}/\text{BIC}/\text{DIC}$
The 1st Sub-Burst						
-1.00~0.17	1.95
-0.17~1.39	16.58	$57.64^{+2.42}_{-2.44}$	-1371/2745/2754/2776	$0.25^{+0.19}_{-0.20}$	$130.9^{+22.4}_{-20.5}$	-1382/2771/2783/2679
1.39~3.16	36.78	$67.30^{+1.76}_{-1.77}$	-1664/3331/3340/3361	$-0.25^{+0.07}_{-0.07}$	$246.9^{+23.0}_{-23.3}$	-1567/3140/3152/3124
3.16~4.43	20.37	$41.04^{+1.56}_{-1.56}$	-1287/2578/2587/2606	$-0.29^{+0.12}_{-0.11}$	$145.8^{+21.6}_{-20.9}$	-1272/2551/2563/2533
4.43~6.20	50.40	$43.18^{+0.83}_{-0.82}$	-1787/3578/3586/3603	$-0.40^{+0.05}_{-0.05}$	$175.7^{+13.5}_{-13.6}$	-1581/3168/3180/3153
6.20~7.63	22.11	$30.95^{+1.08}_{-1.09}$	-1326/2656/2664/2681	$-0.20^{+0.14}_{-0.14}$	$88.3^{+12.2}_{-11.9}$	-1319/2644/2656/2622
7.63~10.00	12.71	$17.83^{+1.08}_{-1.08}$	-1653/3309/3318/3332	$-0.81^{+0.26}_{-0.24}$	$107.3^{+21.7}_{-43.6}$	-1654/3314/3326/3224
The 2nd Sub-Burst						
123.50~124.51	8.70
124.51~125.37	18.72
125.37~127.19	42.29	$-0.85^{+0.05}_{-0.05}$	$433.7^{+59.3}_{-59.0}$	-1589/3185/3197/3162
127.19~128.90	73.12	$-0.91^{+0.03}_{-0.03}$	$654.4^{+63.9}_{-63.2}$	-1663/3333/3345/3312
128.90~129.34	45.93	$-0.82^{+0.05}_{-0.05}$	$455.2^{+63.5}_{-64.1}$	-788/1583/1595/1562
129.34~130.08	69.90	$-0.84^{+0.03}_{-0.03}$	$379.7^{+32.9}_{-33.6}$	-1073/2153/2165/2132
130.08~131.01	96.65	$-0.85^{+0.02}_{-0.02}$	$475.4^{+32.9}_{-32.9}$	-1371/2749/2761/2127
131.01~131.52	102.21	$-1.05^{+0.02}_{-0.02}$	$1529.5^{+197.2}_{-197.5}$	-1087/2180/2193/2153
131.52~131.78	58.68	$-1.00^{+0.04}_{-0.04}$	$478.3^{+74.0}_{-75.4}$	-588/1182/1194/1158
131.78~132.53	81.67	$-0.98^{+0.03}_{-0.03}$	$350.4^{+29.6}_{-29.8}$	-1108/2223/2235/2200
132.53~133.41	97.59	$-0.95^{+0.03}_{-0.03}$	$322.7^{+22.4}_{-21.9}$	-1259/2523/2536/2501
133.41~133.89	97.39	$-0.92^{+0.03}_{-0.03}$	$337.8^{+25.2}_{-25.6}$	-960/1926/1939/1904
133.89~134.25	68.98	$-1.01^{+0.04}_{-0.04}$	$347.5^{+37.9}_{-37.5}$	-695/1397/1409/1374
134.25~134.88	66.71	$-1.05^{+0.04}_{-0.04}$	$264.2^{+28.7}_{-30.0}$	-964/1935/1947/1912
134.88~135.70	57.96	$-0.90^{+0.05}_{-0.05}$	$585.5^{+100.5}_{-101.7}$	-789/1584/1597/1562
135.70~136.55	74.48	$-0.99^{+0.04}_{-0.04}$	$217.8^{+18.6}_{-18.6}$	-1179/2364/2376/2343
136.55~136.95	58.99	$-0.98^{+0.05}_{-0.05}$	$225.3^{+25.0}_{-25.6}$	-681/1368/1380/1346
136.95~137.56	87.39	$-0.96^{+0.03}_{-0.03}$	$265.1^{+21.2}_{-20.8}$	-1025/2056/2069/2034
137.56~138.00	57.35	$-1.10^{+0.05}_{-0.05}$	$278.9^{+36.1}_{-36.3}$	-702/1409/1422/1386
138.00~139.06	66.38	$-1.03^{+0.04}_{-0.04}$	$198.8^{+19.4}_{-19.2}$	-1236/2477/2490/2456
139.06~140.95	64.34	$-1.05^{+0.04}_{-0.04}$	$172.4^{+16.0}_{-15.7}$	-1607/3221/3233/3201
140.95~142.20	39.32	$-1.20^{+0.06}_{-0.06}$	$246.8^{+45.1}_{-45.8}$	-1252/2510/2523/2488
The 3rd Sub-Burst						
142.20~144.93	50.59	$-1.24^{+0.05}_{-0.05}$	$225.0^{+32.1}_{-32.8}$	-1825/3656/3669/3635
144.93~145.56	34.18	$-1.07^{+0.08}_{-0.08}$	$210.1^{+37.9}_{-39.5}$	-858/1723/1735/1701
145.56~145.70	23.86	$-1.30^{+0.13}_{-0.12}$	$927.6^{+197.5}_{-612.5}$	-192/391/403/338
145.70~146.93	86.01	$-0.98^{+0.03}_{-0.03}$	$267.2^{+20.6}_{-20.7}$	-1427/2859/2872/2838
146.93~148.17	70.48	$-1.09^{+0.04}_{-0.04}$	$226.9^{+23.6}_{-23.2}$	-1373/2753/2765/2731
148.17~150.52	78.14	$-1.14^{+0.04}_{-0.04}$	$191.2^{+17.0}_{-17.2}$	-1797/3599/3612/3578
150.52~151.31	34.03	$-1.28^{+0.09}_{-0.09}$	$245.6^{+60.9}_{-63.9}$	-960/1927/1939/1902
151.31~153.26	36.32	$-1.21^{+0.07}_{-0.07}$	$185.2^{+33.0}_{-33.4}$	-1568/3141/3154/3120
153.26~155.00	23.30	$-1.39^{+0.12}_{-0.12}$	$370.7^{+132.8}_{-174.8}$	-1446/2897/2909/2862

Table 5. Results of the Time-resolved Spectral Fits of GRB 160625B

$t_1 \sim t_2$ (s)	S/N	Blackbody Fitting		Cutoff Power-Law Fitting		
		kT (keV)	$-\ln(\text{posterior})/\text{AIC}/\text{BIC}/\text{DIC}$	α	E_c (keV)	$-\ln(\text{posterior})/\text{AIC}/\text{BIC}/\text{DIC}$
The 1st Sub-Burst						
-1.00~0.12	2.72
-0.12~0.04	11.51	$15.67^{+0.80}_{-0.80}$	-106/217/225/234	$-0.21^{+0.27}_{-0.28}$	$38.9^{+7.9}_{-7.4}$	-115/236/249/181
0.04~0.21	21.50	$14.28^{+0.44}_{-0.43}$	-211/426/434/440	$-0.22^{+0.19}_{-0.18}$	$36.0^{+4.7}_{-4.7}$	-203/412/424/386
0.21~0.34	29.48	$18.03^{+0.43}_{-0.42}$	-170/343/352/359	$-0.18^{+0.14}_{-0.13}$	$44.2^{+4.2}_{-4.4}$	-139/283/296/265
0.34~0.68	36.63	$16.15^{+0.29}_{-0.29}$	-535/1073/1082/1089	$-0.09^{+0.12}_{-0.12}$	$37.0^{+3.1}_{-3.0}$	-489/983/996/966
0.68~0.93	15.92	$12.45^{+0.49}_{-0.49}$	-255/514/522/529	$-0.29^{+0.24}_{-0.26}$	$31.4^{+5.3}_{-5.2}$	-256/519/531/481
0.93~2.00	2.83	$6.71^{+1.26}_{-1.31}$	-990/1985/1993/1995	Unconstrained	Unconstrained	Unconstrained
The 2nd Sub-Burst						
187.00~187.36	27.16	$-0.91^{+0.03}_{-0.03}$	$2056.0^{+353.7}_{-351.8}$	-724/1453/1466/1430
187.36~187.88	50.06	$-0.85^{+0.05}_{-0.05}$	$1459.3^{+356.0}_{-367.7}$	-1109/2223/2236/2196
187.88~188.09	52.80	$-0.84^{+0.02}_{-0.02}$	$1581.2^{+163.9}_{-163.0}$	-638/1283/1295/1258
188.09~188.23	53.09	$-0.83^{+0.03}_{-0.03}$	$1728.5^{+191.1}_{-190.0}$	-496/998/1010/972
188.23~188.35	62.07	$-0.79^{+0.02}_{-0.02}$	$1472.5^{+120.3}_{-122.2}$	-459/924/937/899
188.35~188.71	132.93	$-0.76^{+0.01}_{-0.01}$	$1255.0^{+53.0}_{-52.6}$	-1491/2989/3001/2963
188.71~189.48	222.36	$-0.71^{+0.01}_{-0.01}$	$798.3^{+22.6}_{-23.0}$	-2630/5266/5279/5242
189.48~189.88	156.48	$-0.68^{+0.01}_{-0.01}$	$595.1^{+22.1}_{-22.2}$	-1570/3145/3157/3121
189.88~190.27	129.50	$-0.71^{+0.02}_{-0.02}$	$561.6^{+24.2}_{-24.2}$	-1366/2739/2751/2716
190.27~190.64	105.03	$-0.72^{+0.02}_{-0.02}$	$485.0^{+23.1}_{-23.3}$	-1152/2310/2322/2287
190.64~191.46	131.97	$-0.70^{+0.02}_{-0.02}$	$377.7^{+13.4}_{-13.1}$	-1684/3374/3387/3353
191.46~192.98	149.30	$-0.74^{+0.01}_{-0.01}$	$325.7^{+9.8}_{-9.7}$	-2204/4414/4427/4393
192.98~193.69	124.78	$-0.64^{+0.02}_{-0.02}$	$321.4^{+10.6}_{-10.5}$	-1504/3015/3027/2994
193.69~194.24	124.26	$-0.64^{+0.02}_{-0.02}$	$394.8^{+13.5}_{-13.5}$	-1412/2830/2843/2809
194.24~195.41	195.01	$-0.64^{+0.01}_{-0.01}$	$390.3^{+8.6}_{-8.5}$	-2342/4691/4703/4669
195.41~195.91	121.36	$-0.65^{+0.02}_{-0.02}$	$378.3^{+13.4}_{-13.5}$	-1360/2727/2739/2706
195.91~196.69	138.84	$-0.65^{+0.01}_{-0.01}$	$359.2^{+10.8}_{-10.8}$	-1698/3402/3414/3381
196.69~197.26	90.53	$-0.73^{+0.02}_{-0.02}$	$334.9^{+15.6}_{-15.4}$	-1252/2509/2522/2488
197.26~197.92	117.08	$-0.68^{+0.02}_{-0.02}$	$418.7^{+14.8}_{-14.9}$	-1442/2890/2902/2868
197.92~198.30	98.33	$-0.68^{+0.02}_{-0.02}$	$438.9^{+19.2}_{-19.3}$	-1050/2105/2118/2084
198.30~198.45	50.87	$-0.70^{+0.04}_{-0.04}$	$337.7^{+26.7}_{-26.8}$	-420/846/858/825
198.45~198.71	53.71	$-0.74^{+0.03}_{-0.03}$	$318.6^{+23.4}_{-23.8}$	-691/1387/1400/1366
198.71~198.97	67.75	$-0.64^{+0.03}_{-0.03}$	$390.0^{+23.1}_{-23.4}$	-732/1471/1483/1450
198.97~199.83	139.11	$-0.65^{+0.01}_{-0.01}$	$412.6^{+12.0}_{-12.3}$	-1740/3487/3499/3466
199.83~200.11	89.67	$-0.58^{+0.02}_{-0.02}$	$438.8^{+19.1}_{-19.1}$	-884/1773/1786/1753
200.11~201.20	195.06	$-0.70^{+0.01}_{-0.01}$	$615.2^{+16.3}_{-16.0}$	-2687/5379/5392/5356
201.20~202.49	178.57	$-0.67^{+0.01}_{-0.01}$	$421.8^{+9.8}_{-9.6}$	-2303/4613/4625/4591
202.49~203.38	122.69	$-0.74^{+0.01}_{-0.01}$	$398.2^{+13.8}_{-13.8}$	-1718/3442/3454/3420
203.38~204.65	108.96	$-0.79^{+0.02}_{-0.02}$	$369.8^{+14.1}_{-14.2}$	-1880/3767/3779/3745
204.65~204.91	63.36	$-0.70^{+0.03}_{-0.03}$	$449.0^{+29.1}_{-29.2}$	-704/1413/1426/1392
204.91~206.30	113.25	$-0.70^{+0.02}_{-0.02}$	$326.4^{+10.9}_{-10.9}$	-1924/3855/3867/3835
206.30~207.80	84.56	$-0.76^{+0.02}_{-0.02}$	$253.9^{+11.3}_{-11.3}$	-1846/3698/3710/3679
207.80~208.65	53.47	$-0.83^{+0.03}_{-0.04}$	$238.1^{+18.4}_{-18.3}$	-1340/2685/2698/2665
208.65~211.64	80.40	$-0.89^{+0.02}_{-0.02}$	$282.8^{+13.3}_{-13.6}$	-2277/4560/4572/4540
211.64~212.58	31.33	$-0.99^{+0.06}_{-0.06}$	$224.7^{+30.5}_{-30.5}$	-1231/2467/2480/2447
212.58~213.88	22.09	$-1.13^{+0.06}_{-0.06}$	$260.5^{+46.4}_{-47.5}$	-1392/2791/2803/2770
213.88~218.00	22.46	$-1.16^{+0.06}_{-0.06}$	$364.2^{+77.1}_{-76.7}$	-2185/4377/4389/4356

Table 6. Results of the Time-resolved Spectral Fits of Our Sample (Part I): BB vs. PL+BB

$t_1 \sim t_2$ (s)	S/N	Blackbody Fitting		Power-law Plus Blackbody Fitting			Null Hypothesis Probability	Support Model
		kT (keV)	$-\ln(\text{posterior})/\text{AIC/BIC/DIC}$	Index	kT (keV)	$-\ln(\text{posterior})/\text{AIC/BIC/DIC}$		
140206B								
-0.04~0.46	13.87	$55.23^{+2.52}_{-2.48}$	-599/1202/1210/1231	$-2.99^{+0.53}_{-0.43}$	$56.8^{+2.6}_{-2.6}$	-602/1211/1228/1225	$< 10^{-4}$	BB
0.46~1.81	9.94	$45.05^{+2.71}_{-2.73}$	-1179/2361/2369/2391	$-3.90^{+0.91}_{-0.84}$	$45.2^{+2.6}_{-2.6}$	-1182/2371/2388/2396	$< 10^{-4}$	BB
1.81~4.70	5.50	$44.15^{+5.26}_{-5.18}$	-1676/3356/3364/3387	$-3.87^{+0.65}_{-0.72}$	$45.0^{+5.3}_{-5.8}$	-1681/3369/3386/3392	$< 10^{-4}$	BB
140329B								
-0.01~0.25	39.54	$40.15^{+1.00}_{-1.00}$	-509/1022/1030/1037	$-1.54^{+0.03}_{-0.03}$	$42.2^{+1.8}_{-1.8}$	-394/796/811/798	1	PL+BB
0.25~0.47	20.46	$20.62^{+0.80}_{-0.81}$	-221/446/454/458	$-1.73^{+0.08}_{-0.08}$	$21.5^{+1.6}_{-1.6}$	-197/402/417/402	1	PL+BB
0.47~0.67	9.51	$13.75^{+1.79}_{-1.81}$	-145/294/302/303	$-1.90^{+0.13}_{-0.07}$	$15.0^{+26.2}_{-13.7}$	-109/226/241/-55259	1	PL+BB
0.67~3.00	4.17	$12.19^{+2.42}_{-2.43}$	-1114/2231/2239/2237	$-2.11^{+0.29}_{-0.28}$	$5.7^{+8.7}_{-4.5}$	-1106/2220/2235/-5331	1	PL+BB
150330A								
-0.17~1.39	16.58	$57.64^{+2.42}_{-2.44}$	-1371/2745/2754/2776	$-1.69^{+0.20}_{-0.22}$	$59.3^{+2.9}_{-2.9}$	-1374/2755/2772/2774	$< 10^{-4}$	BB
1.39~3.16	36.78	$67.30^{+1.76}_{-1.77}$	-1664/3331/3340/3361	$-1.46^{+0.04}_{-0.04}$	$73.8^{+2.5}_{-2.5}$	-1595/3198/3214/3213	1	PL+BB
3.16~4.43	20.37	$41.04^{+1.56}_{-1.56}$	-1287/2578/2587/2606	$-1.49^{+0.07}_{-0.07}$	$43.1^{+2.2}_{-2.3}$	-1269/2547/2563/2561	1	PL+BB
4.43~6.20	50.40	$43.18^{+0.83}_{-0.82}$	-1787/3578/3586/3603	$-1.45^{+0.02}_{-0.02}$	$45.7^{+1.4}_{-1.4}$	-1612/3232/3249/3244	1	PL+BB
6.20~7.63	22.11	$30.95^{+1.08}_{-1.09}$	-1326/2656/2664/2681	$-1.62^{+0.10}_{-0.10}$	$32.3^{+1.6}_{-1.6}$	-1311/2629/2646/2642	1	PL+BB
7.63~10.00	12.71	$17.83^{+1.08}_{-1.08}$	-1653/3309/3318/3332	$-1.70^{+0.11}_{-0.11}$	$18.8^{+2.1}_{-2.2}$	-1639/3287/3303/3295	1	PL+BB
160625B								
-0.12~0.04	11.51	$15.67^{+0.80}_{-0.80}$	-106/217/225/234	$-2.59^{+0.40}_{-0.38}$	$17.5^{+1.2}_{-1.2}$	-111/230/246/238	$< 10^{-4}$	BB
0.04~0.21	21.50	$14.28^{+0.44}_{-0.43}$	-211/426/434/440	$-1.94^{+0.13}_{-0.13}$	$15.0^{+0.9}_{-0.8}$	-200/409/425/405	0.99	PL+BB
0.21~0.34	29.48	$18.03^{+0.43}_{-0.42}$	-170/343/352/359	$-2.24^{+0.15}_{-0.16}$	$20.7^{+0.7}_{-0.7}$	-142/291/308/284	1	PL+BB
0.34~0.68	36.63	$16.15^{+0.29}_{-0.29}$	-535/1073/1082/1089	$-2.09^{+0.10}_{-0.10}$	$17.9^{+0.5}_{-0.5}$	-489/986/1003/982	1	PL+BB
0.68~0.93	15.92	$12.45^{+0.49}_{-0.49}$	-255/514/522/529	$-2.42^{+0.28}_{-0.31}$	$14.1^{+0.9}_{-0.9}$	-254/517/533/509	0.63	PL+BB
0.93~2.00	2.83	$6.71^{+1.26}_{-1.31}$	-990/1985/1993/1995	$-3.75^{+0.99}_{-0.85}$	$6.4^{+1.7}_{-1.5}$	-986/1981/1997/1981	0.98	PL+BB

Table 7. Comparison of Different Models of Our Sample (Part I) with the Brightest Time Bin

GRB Name	Single BB ^a	CPL ^b	PL+BB ^c	CPL+BB ^d	Band+BB ^e	Best Model Suggested
(1)	(2)	(3)	(4)	(5)	(6)	(7)
140206B						
-ln(posterior)	-599	-609	-601	Unconstrained ^f	Unconstrained	Single BB
AIC	1202	1225	1211	Unconstrained	Unconstrained	
BIC	1210	1237	1227	Unconstrained	Unconstrained	
DIC	1231	1212	1225	Unconstrained	Unconstrained	
dof	439	438	437	436	435	
140329B						
-ln(posterior)	-509	-377	-394	-371	Unconstrained	PL+BB
AIC	1022	760	796	753	Unconstrained	
BIC	1030	771	811	772	Unconstrained	
DIC	1037	747	798	750	Unconstrained	
dof	324	323	322	321	320	
150330A						
-ln(posterior)	-1787	-1582	-1608	-1574	Unconstrained	CPL+BB
AIC	3578	3169	3223	3158	Unconstrained	
BIC	3586	3182	3240	3178	Unconstrained	
DIC	3603	3153	3244	2866	Unconstrained	
dof	442	441	440	439	438	
160625B						
-ln(posterior)	-535	-489	-489	-479	Unconstrained	PL+BB
AIC	1073	983	986	968	Unconstrained	
BIC	1082	996	1003	988	Unconstrained	
DIC	1089	966	982	970	Unconstrained	
dof	437	436	435	434	433	

^aSingle BB model fitting.

^bCut power-law model fitting.

^cSimple power-law plus BB model fitting.

^dCut power-law plus BB model fitting.

^eBand plus BB model fitting.

^fParameters cannot be constrained with the model.

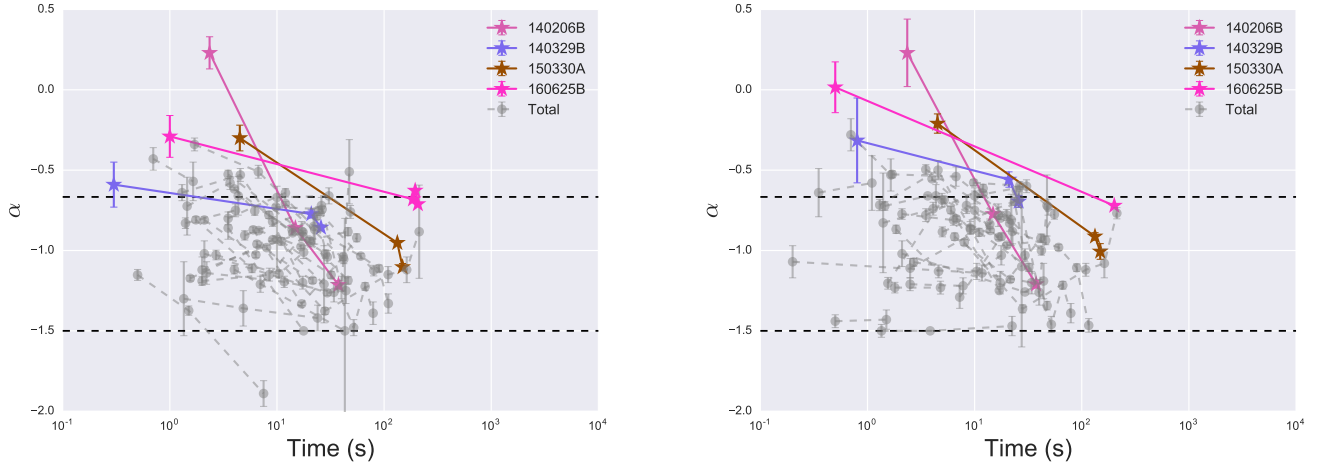


Figure 1. Temporal evolution of α based on the time-integrated spectra for each pulse/sub-burst for our global sample. Each data point represents one pulse/sub-burst, and they are connected by solid lines within one single burst. Two horizontal dashed lines represent the limiting values of $\alpha=-2/3$ and $\alpha=-3/2$ for electrons in the slow- and fast-cooling regimes, respectively. Left panel: for the CPL model; right panel: for the Band model.

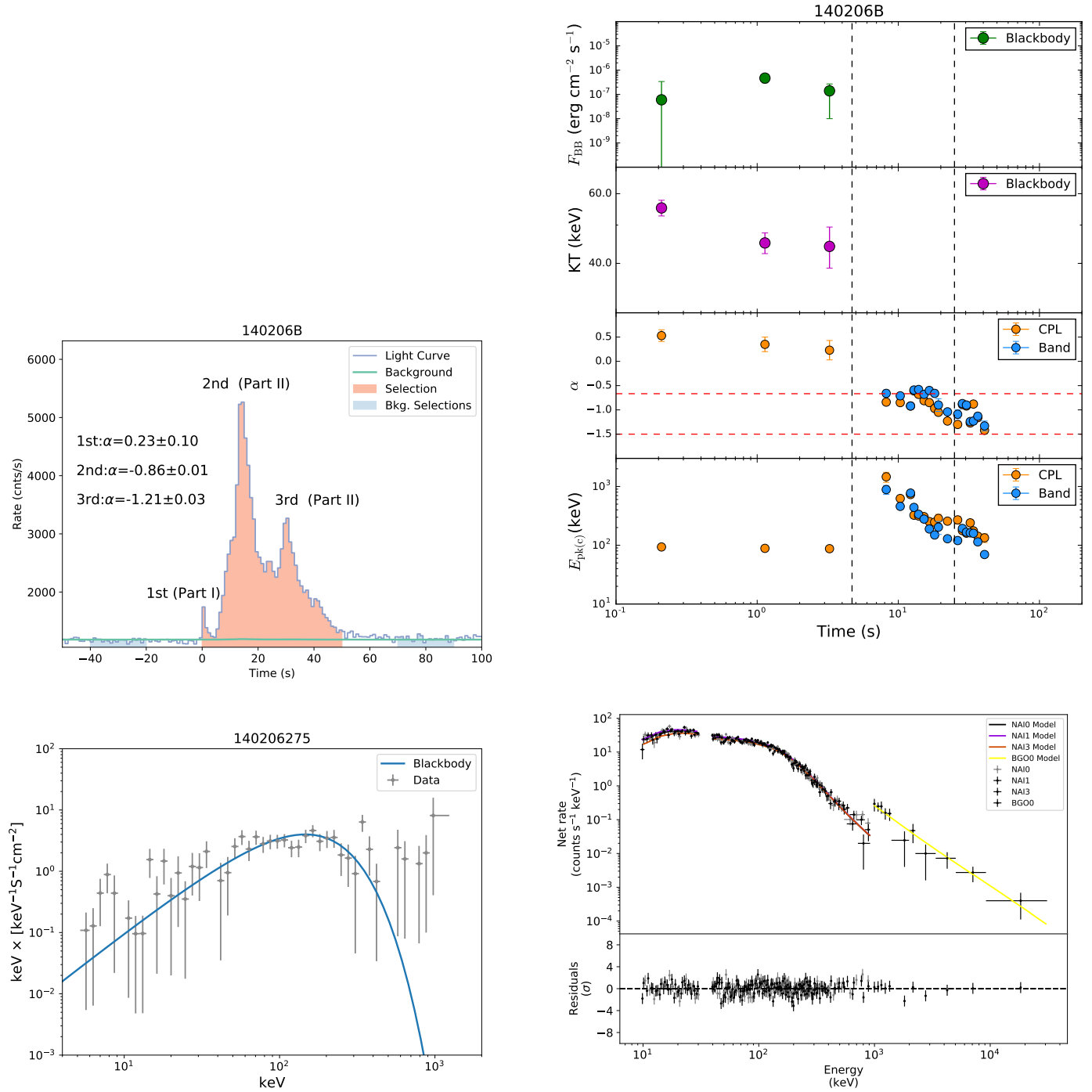


Figure 2. Top left panel: light curve of the prompt emission of GRB 140206B, along with the source selection, the background selections, and the best background fits. Top right panel: temporal evolution of α (Band and CPL), $E_{\text{pk}(c)}$ (Band and CPL), BB temperature, and BB flux F_{BB} based on the time-resolved spectrum for GRB 140206B. Three pulses/sub-bursts are divided by two vertical black dashed lines. Two horizontal red dashed lines represent the limiting values of $\alpha = -2/3$ and $\alpha = -3/2$ for electrons in the slow- and fast-cooling regimes, respectively. Bottom left panel: typical spectral fits using the brightest time bin (-0.04, 0.46) for Part I. Bottom right panel: typical spectral fits using the brightest time bin (13.24, 14.60) for Part II.

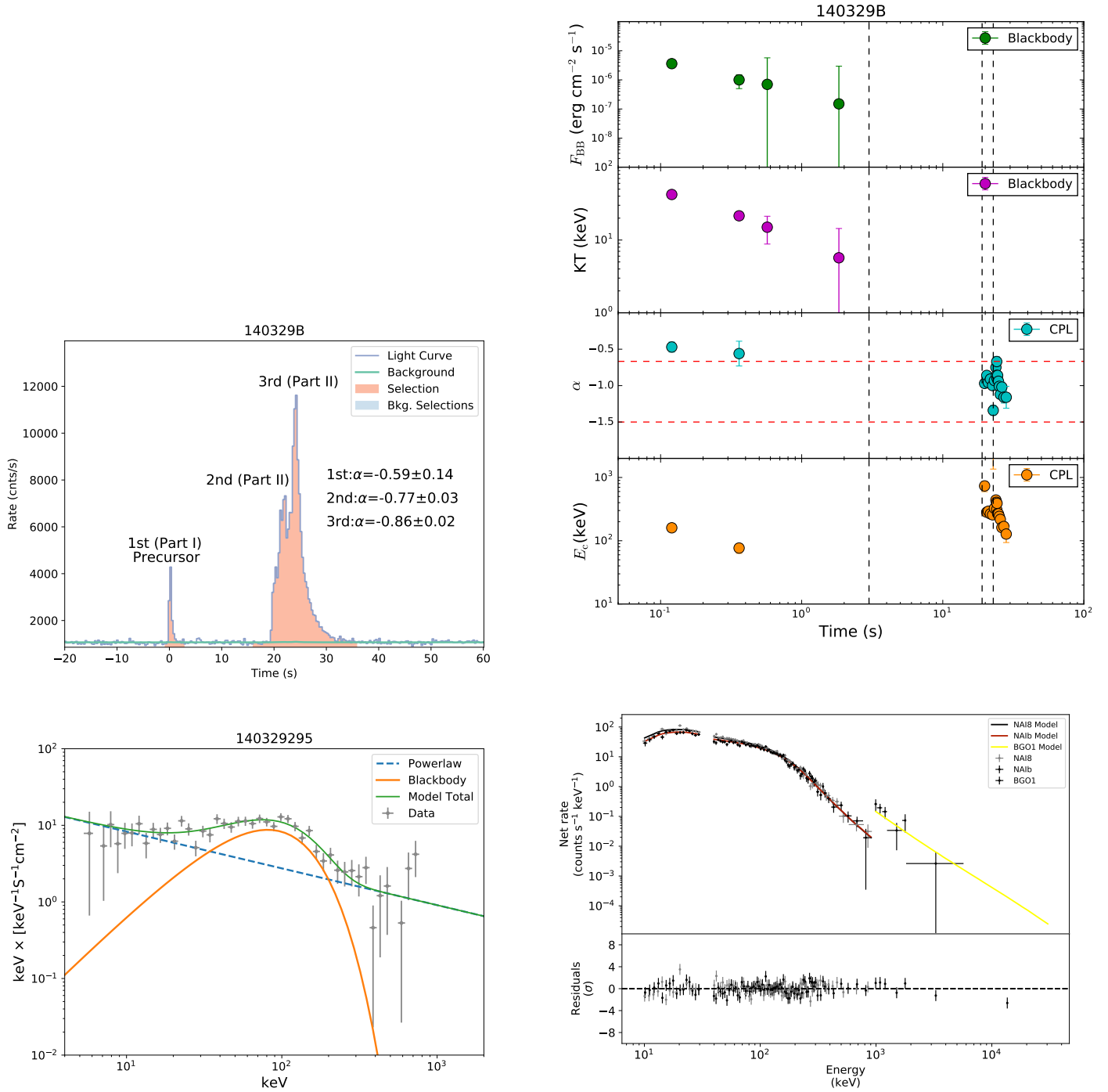


Figure 3. Same as Figure 2 but for GRB 140329B. The brightest time bins (highest S/N values) for Part I (-0.01-0.25) and for Part II (21.17-22.77) are used.

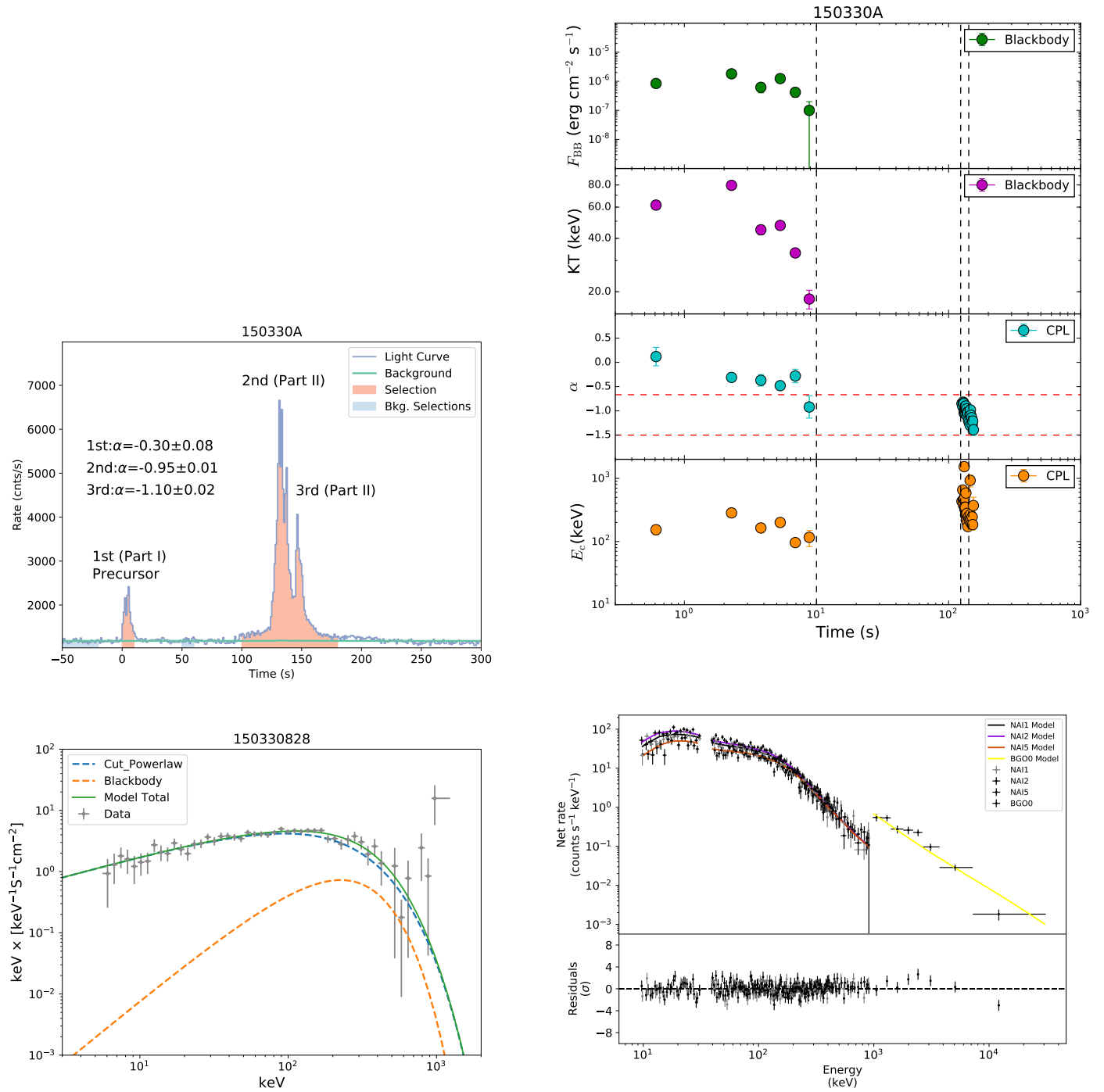


Figure 4. Same as Figure 2 but for GRB 150330A. The brightest time bins for Part I (4.43-6.20) and for Part II (131.01-131.52) are used.

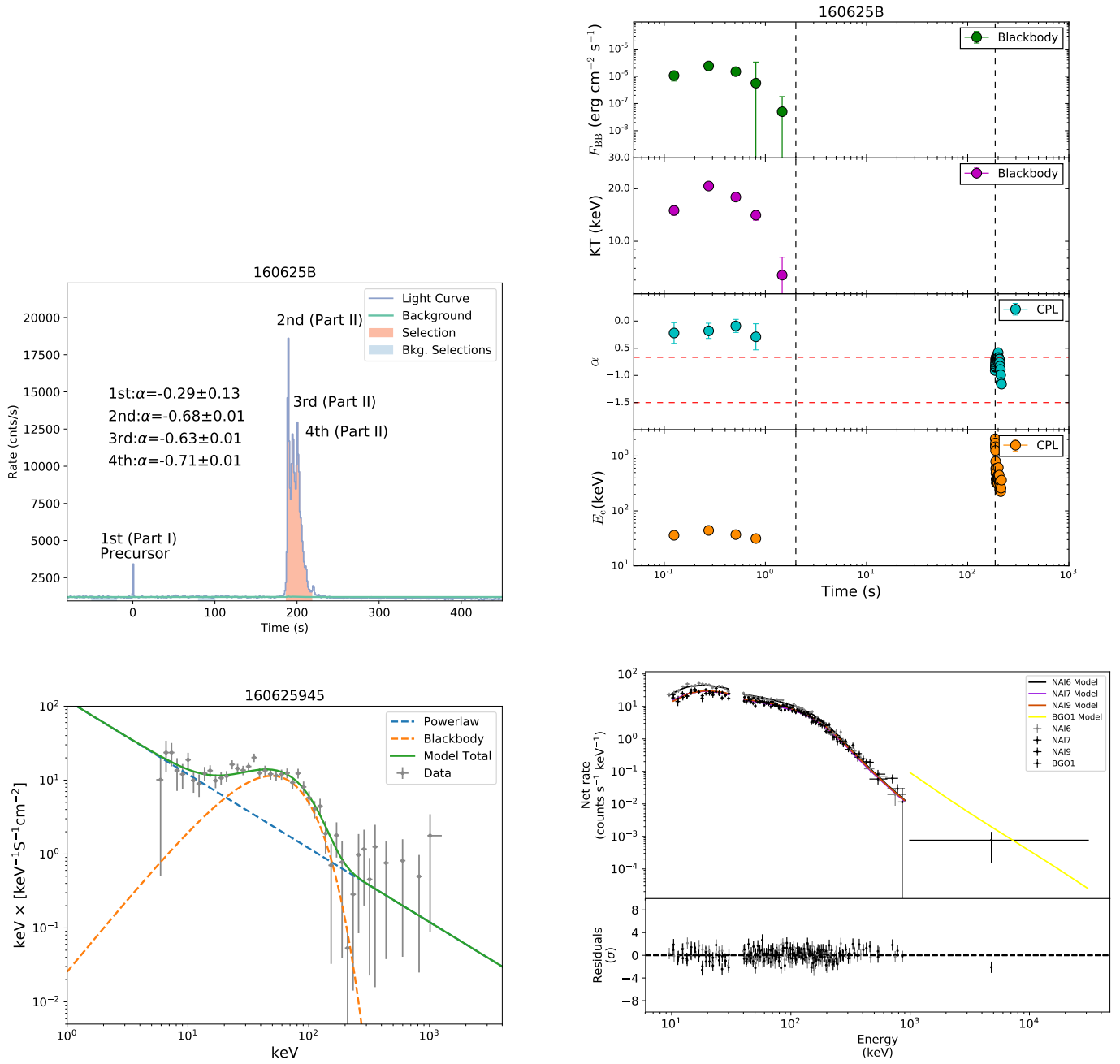


Figure 5. Same as Figure 2 but for GRB 160625B. Time bins for Part I (0.34-0.68) and for Part II (208.65-211.64) are used.

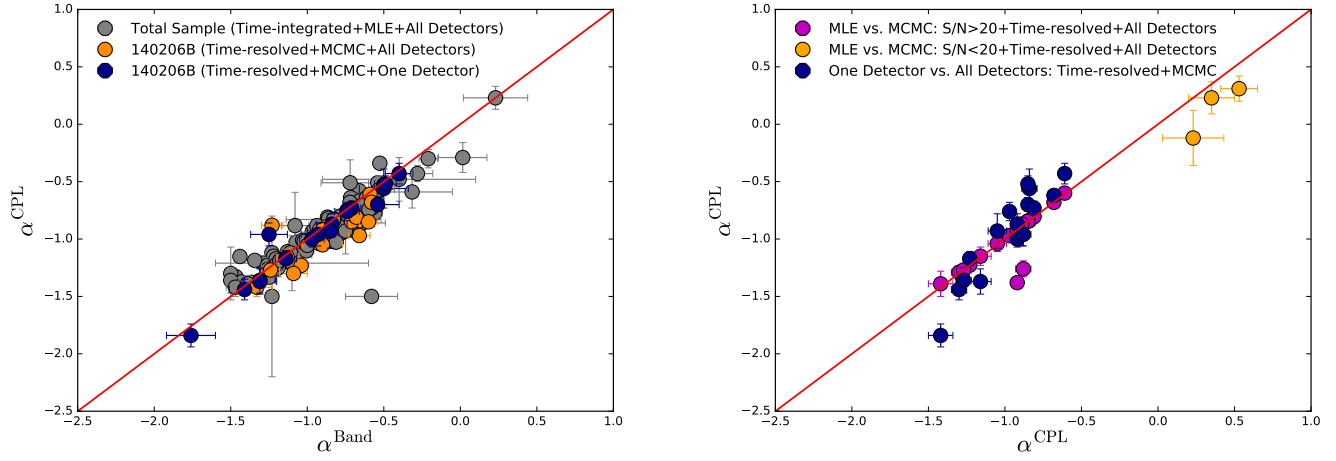


Figure 6. Correlation analysis of α for different cases. The left panel investigates the difference of α between the Band and the CPL models with three different cases. The right panel compares α also with three different scenarios but based on the same CPL model.

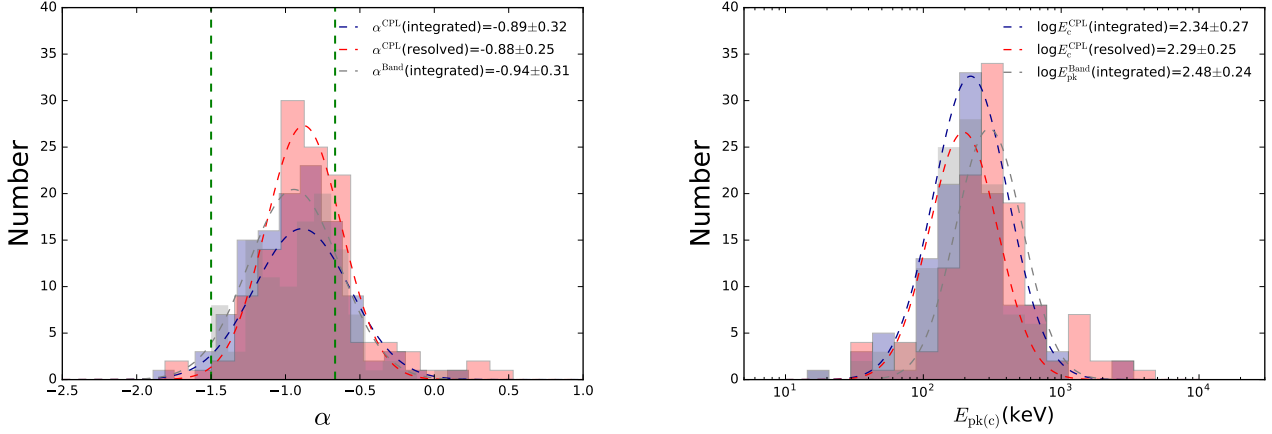


Figure 7. Comparisons of α -distributions (left panel) and $E_{\text{pk}(c)}$ -distributions (right panel) in different scenarios (Band or CPL, time-resolved or time-integrated). Based on the CPL model and the time-integrated spectral fit results, the best Gaussian fits give $\alpha^{\text{CPL}}=0.89\pm0.32$ and $\log E_c^{\text{CPL}}=2.34\pm0.27$; based on the CPL model and the time-resolved spectral fit results, we have $\alpha^{\text{CPL}}=0.88\pm0.25$ and $\log E_c^{\text{CPL}}=2.29\pm0.25$; based on the Band model and the time-integrated spectral fit results, we have $\alpha^{\text{Band}}=0.94\pm0.31$ and $\log E_{\text{pk}}^{\text{Band}}=2.48\pm0.24$. Two vertical green dashed lines represent the limiting values of $\alpha=-2/3$ and $\alpha=-3/2$ for electrons in the slow- and fast-cooling regimes, respectively.

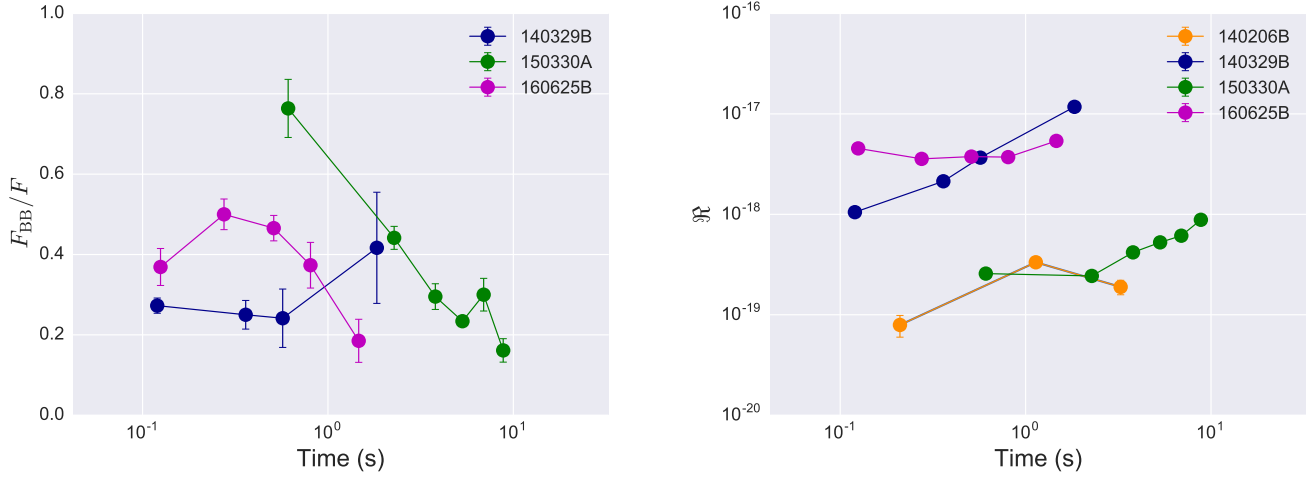


Figure 8. Left panel: evolution of the fraction of thermal flux to total flux, F_{BB}/F . Right panel: evolution of the parameter $\mathfrak{R} = (F_{\text{BB}}/\sigma T^4)^{1/2}$. Different colors represent in each individual burst: GRB 140206B (orange), GRB 140329B (blue), GRB 150330A (green), GRB 160625B (pink).

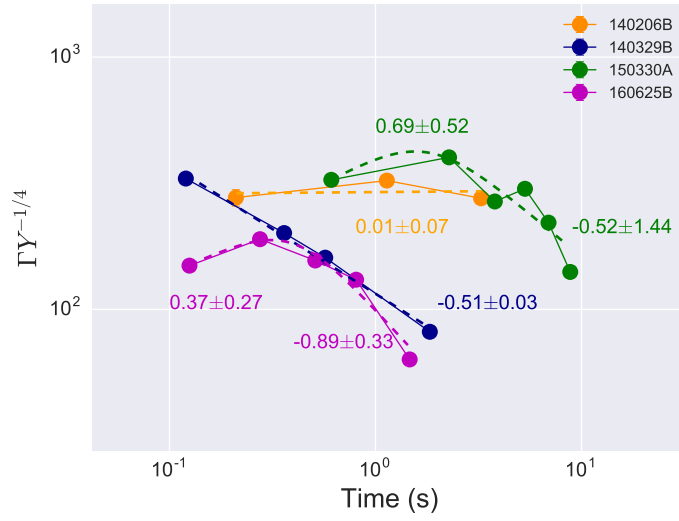


Figure 9. Temporal evolution of the Lorentz factor, Γ . Color conventions are the same as in Figure 8. GRB 140206B presents a constant behavior with best-fitting power-law index 0.01 ± 0.07 , while GRB 140329B shows monotonic decay with the index -0.51 ± 0.03 . GRB 150330A and GRB 160625B exhibit a smoothly broken power-law decay feature, with the power-law indices 0.69 ± 0.52 and -0.52 ± 1.44 before and after break for GRB 150330A; and 0.37 ± 0.27 and -0.89 ± 0.33 before and after break for GRB 160625B.

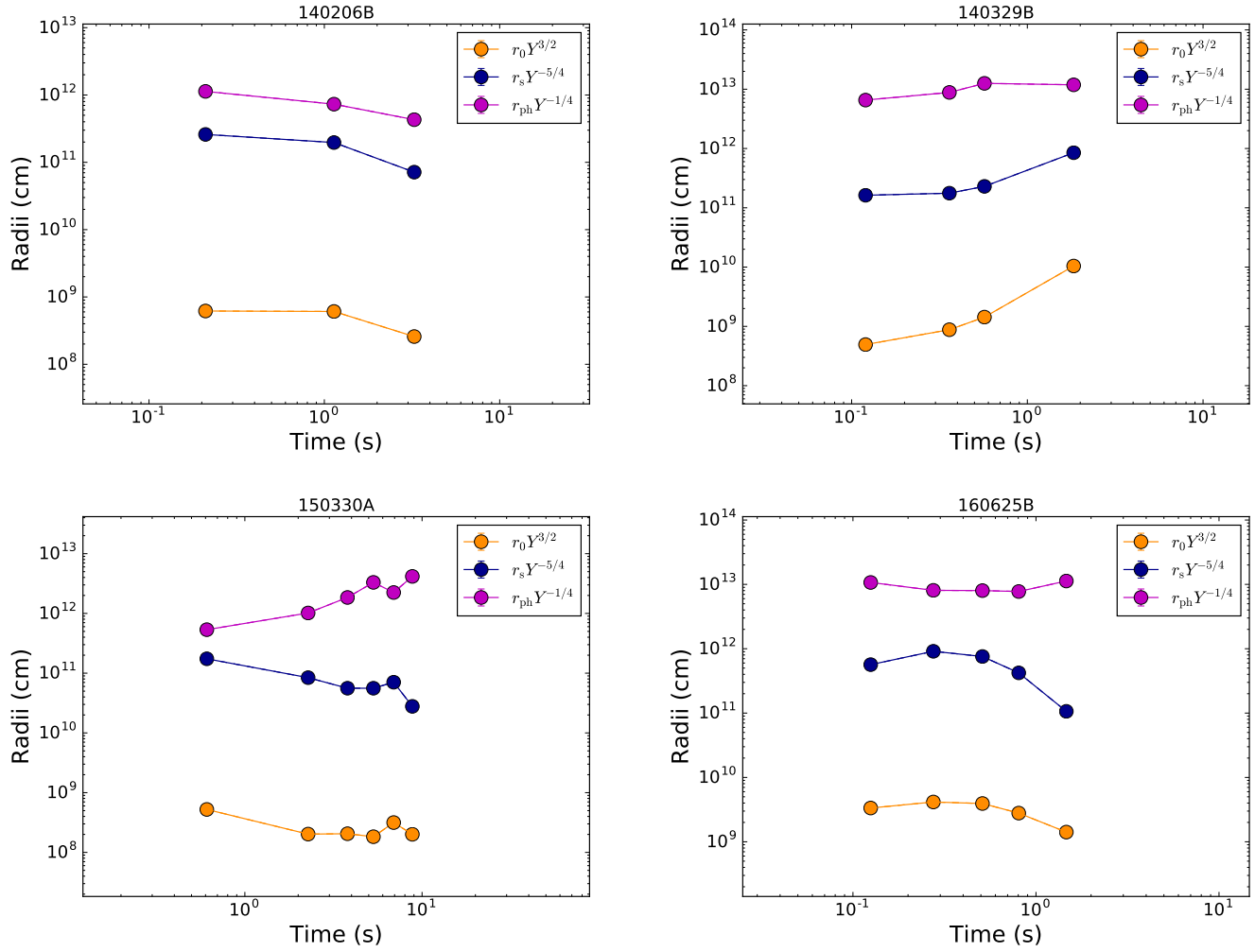


Figure 10. Temporal evolution of the photospheric radius r_{ph} , saturation radius r_s , and nozzle radius r_0 . Different colors represent in different characteristic radii: r_0 (orange), r_s (blue), r_{ph} (pink).

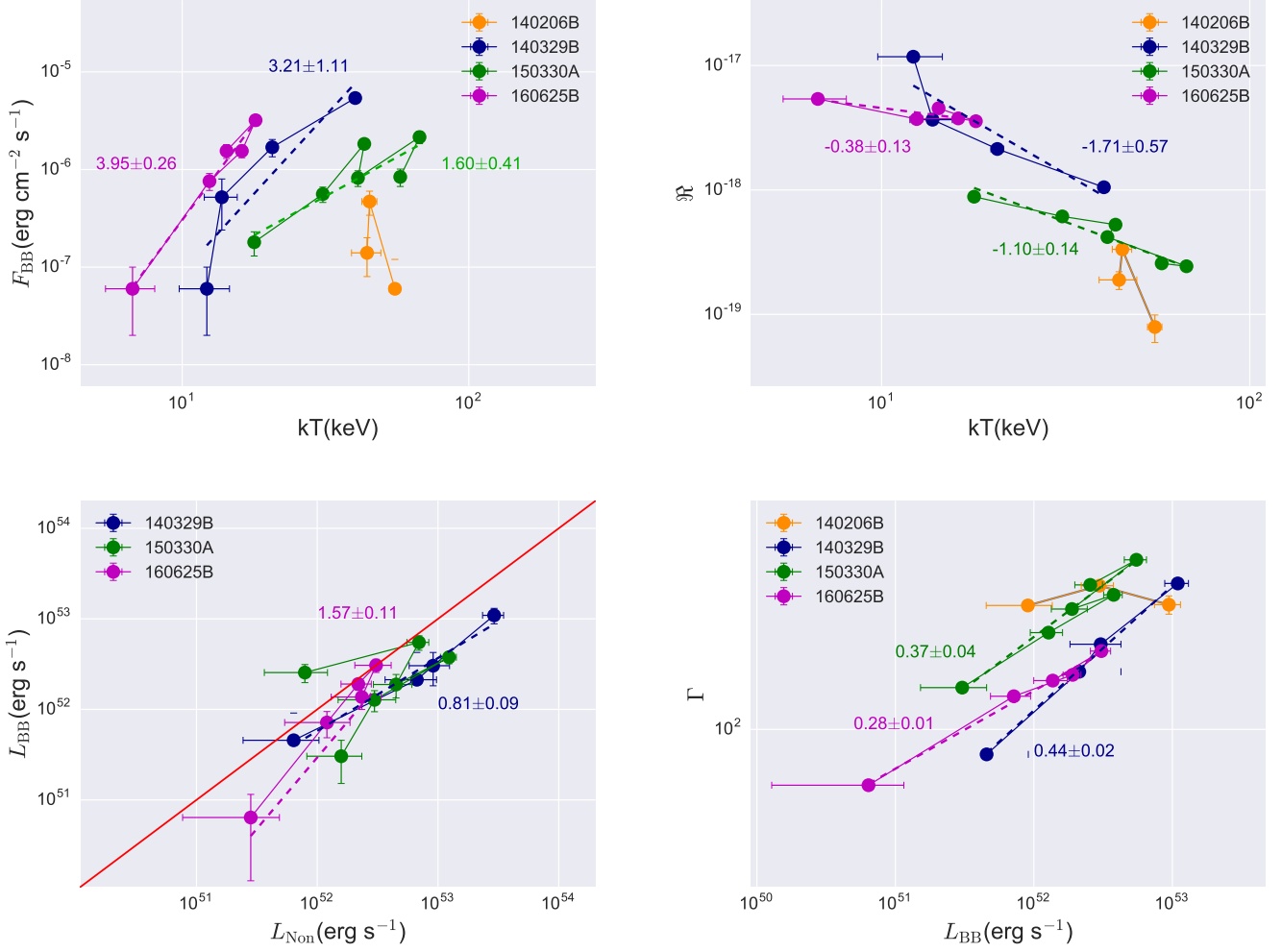


Figure 11. Scatter plots of several characteristic parameters of photosphere emission: F_{BB} vs. kT (top left panel), \mathcal{R} vs. kT (top right panel), L_{BB} vs. L_{Non} (bottom right panel), and Γ vs. L_{BB} (bottom left panel). Color conventions are the same as in Figure 8. $F_{\text{BB}}-kT$, $\mathcal{R}-kT$, $L_{\text{BB}}-L_{\text{Non}}$ and $\Gamma-L_{\text{BB}}$ are all found to have the hardness-intensity correlations. For $F_{\text{BB}}-kT$ correlation, the best-fitting results give a power-law index of 3.21 ± 0.25 for GRB 140329B, 1.60 ± 0.41 for GRB 150330A, and 3.95 ± 0.26 for GRB 160625B; For $\mathcal{R}-kT$ correlation, we have -1.71 ± 0.57 for GRB 140329B, -1.10 ± 0.14 for GRB 150330A, and -0.38 ± 0.13 for GRB 160625B; For $L_{\text{BB}}-L_{\text{Non}}$ correlation, we obtain 0.81 ± 0.09 for GRB 140329B, and 1.57 ± 0.11 for GRB 160625B, the solid line in the panel represents the equal line. For $\Gamma-L_{\text{BB}}$ correlation, we have 0.44 ± 0.02 for GRB 140329B, 0.37 ± 0.04 for GRB 150330A, and 0.28 ± 0.01 for GRB 160625B.

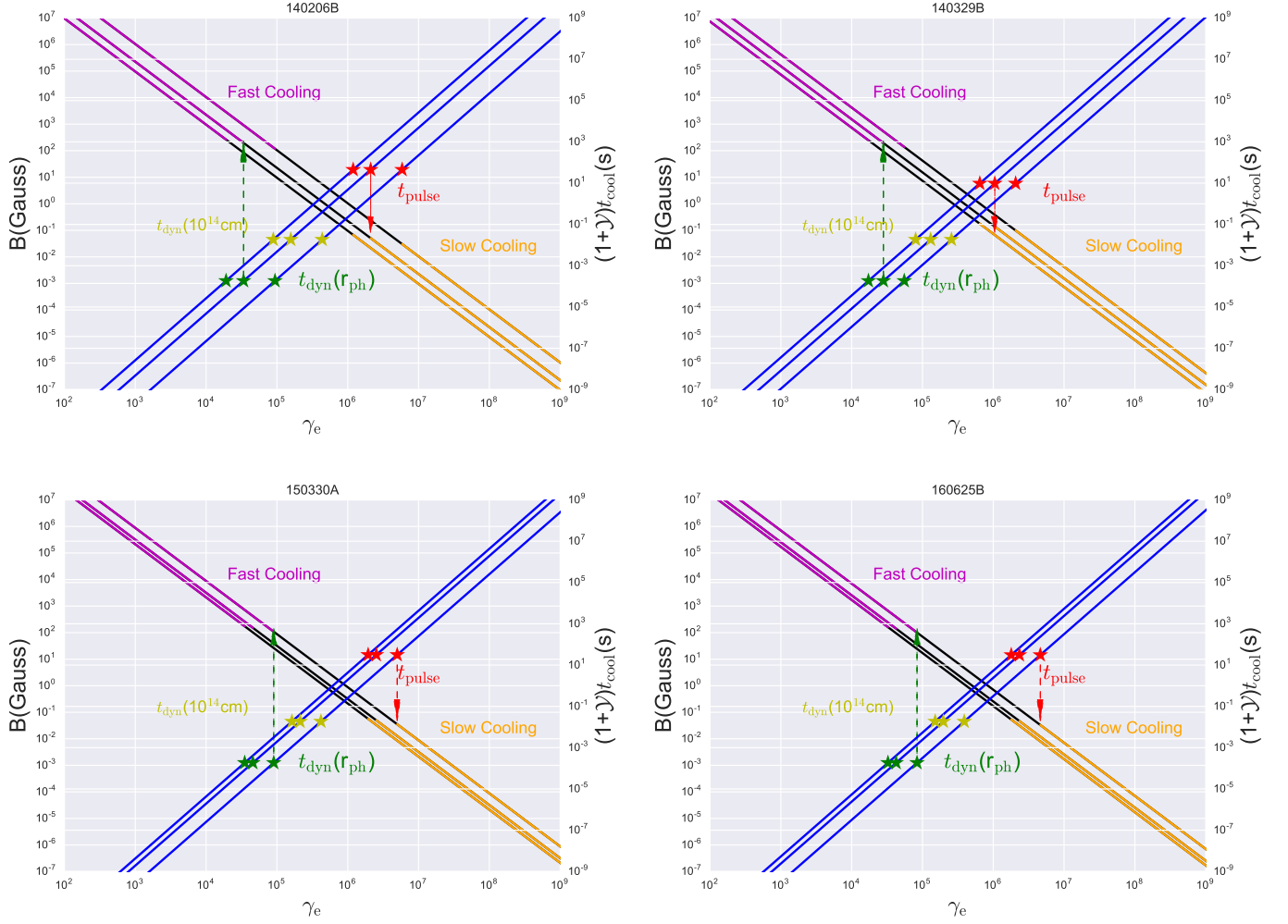


Figure 12. Allowed relations between B and γ_e based on synchrotron emission. The left y-axis (B as a function of γ_e : purple, black, and orange lines) shows the constraints obtained for $B\gamma_e^2$ from Equation (17) for three time bins: one before (earliest), one at, and one after (latest) the peak of the prompt emission light curve. The right y-axis displays t_{cool} as a function of γ_e (blue lines). The dynamical time for different characteristic radii (r_{ph} : grey star; 10^{14} cm: blue star) and t_{pulse} (red star) are marked with different colors. The red area lines show the values of γ_e and B that result in $t_{\text{cool}} < t_{\text{dyn}}(r_{\text{ph}})$ for all allowed values of $r_d > r_{\text{ph}}$, which indicates that the electrons are always in the fast-cooling regime. The orange area lines represent that the values of γ_e and B will always result in $t_{\text{cool}} < t_{\text{pulse}}$, which is in the slow-cooling regime for the allowed values of r_d . The black area lines represent the values of γ_e and B for the case $t_{\text{dyn}}(r_{\text{ph}}) < t_{\text{cool}} < t_{\text{pulse}}$, which can result in synchrotron emission for electrons cooling either fast or slow depending on what the corresponding dynamical time is and where the dissipation occurs.

APPENDIX

In this Appendix, we provide additional figures, including model comparison with different criteria (Figure S1), examples of the GBM light curve (Figure S2), parameter relations for difference pulses/sub-bursts (Figures S3 and S4), temporal evolution of S/N of GRB 140206B (Figure S5), examples of the MCMC fit using the different spectral models (Figures S6–S8), and the temporal evolution of $B\gamma_e^2$ for various typical Γ values (Figure S9).

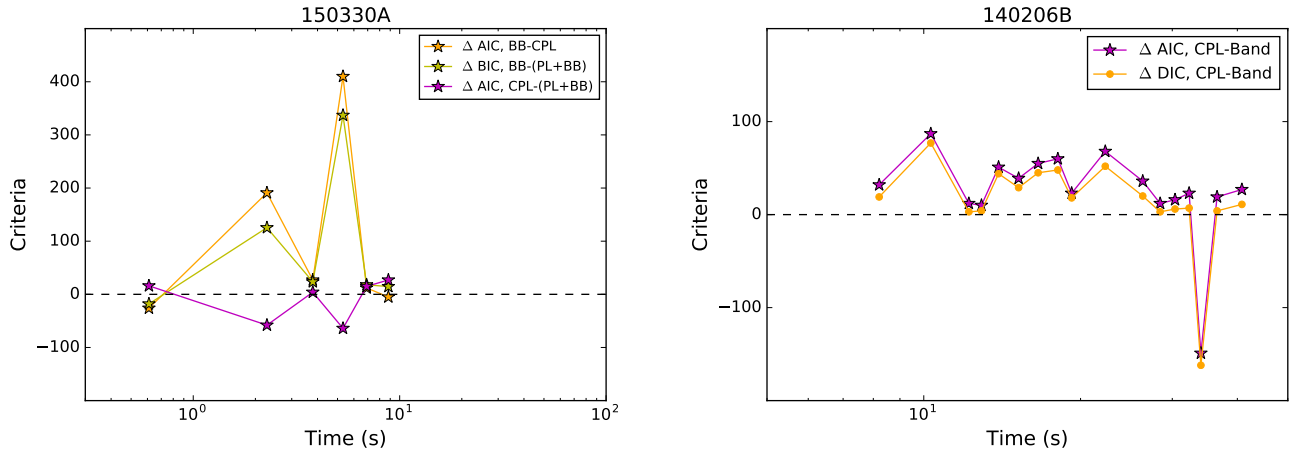


Figure S1. Temporal evolution of the Δ AIC/BIC/DIC, which is derived from comparing two different empirical models and based on the time-resolved spectral fitting results. The left-hand panel: data is derived from GRB 150330A (Part I); the right-hand panel: data is derived from GRB 140206B (Part II). Different color represents different empirical models, and the horizontal dashed lines either represent the value of Δ AIC/BIC/DIC=0.

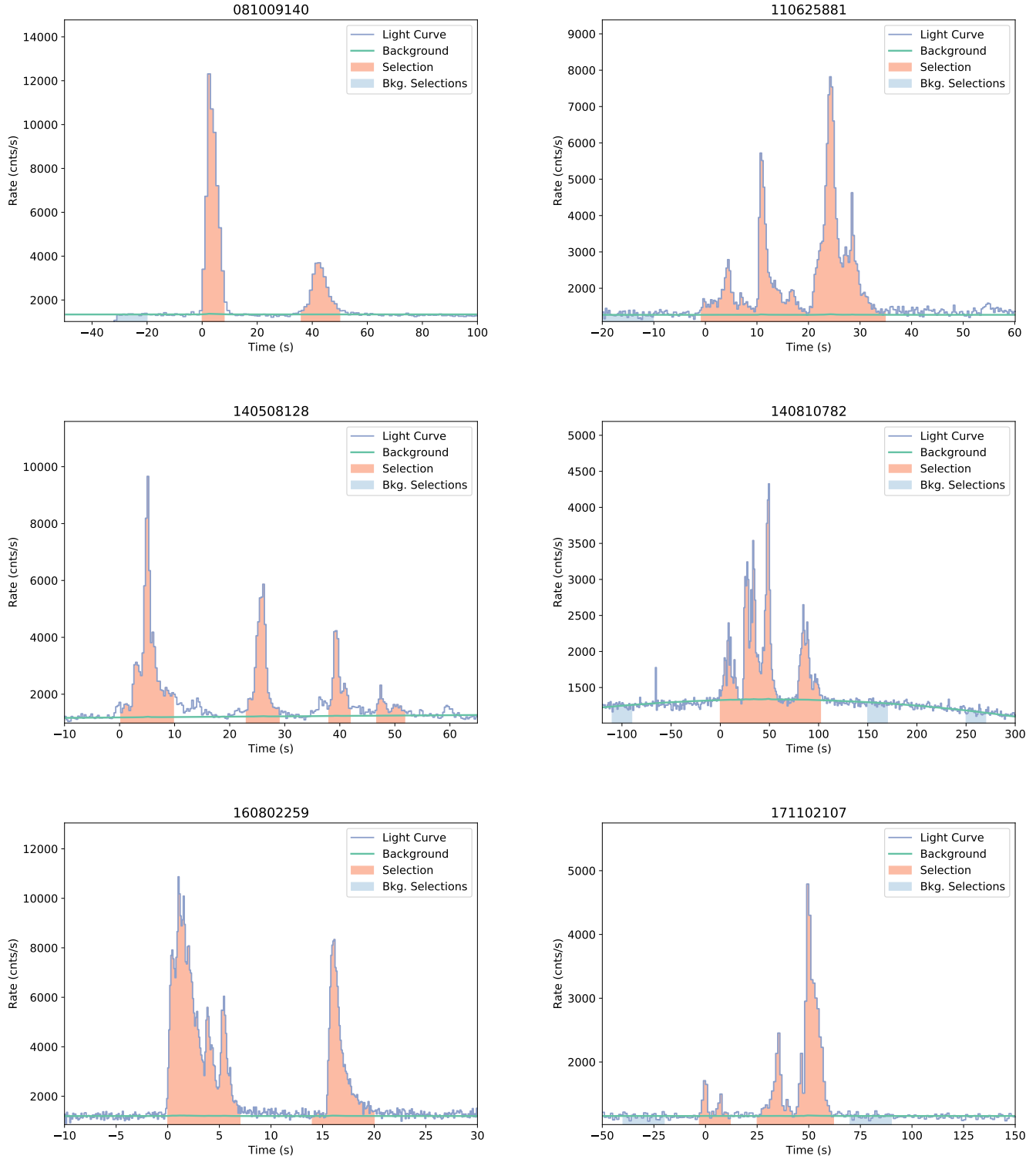


Figure S2. Examples of the light curve of the prompt emission, which exhibit clear multi-pulses/sub-bursts in our sample, along with the source selection, the background selections, and the best background fits.

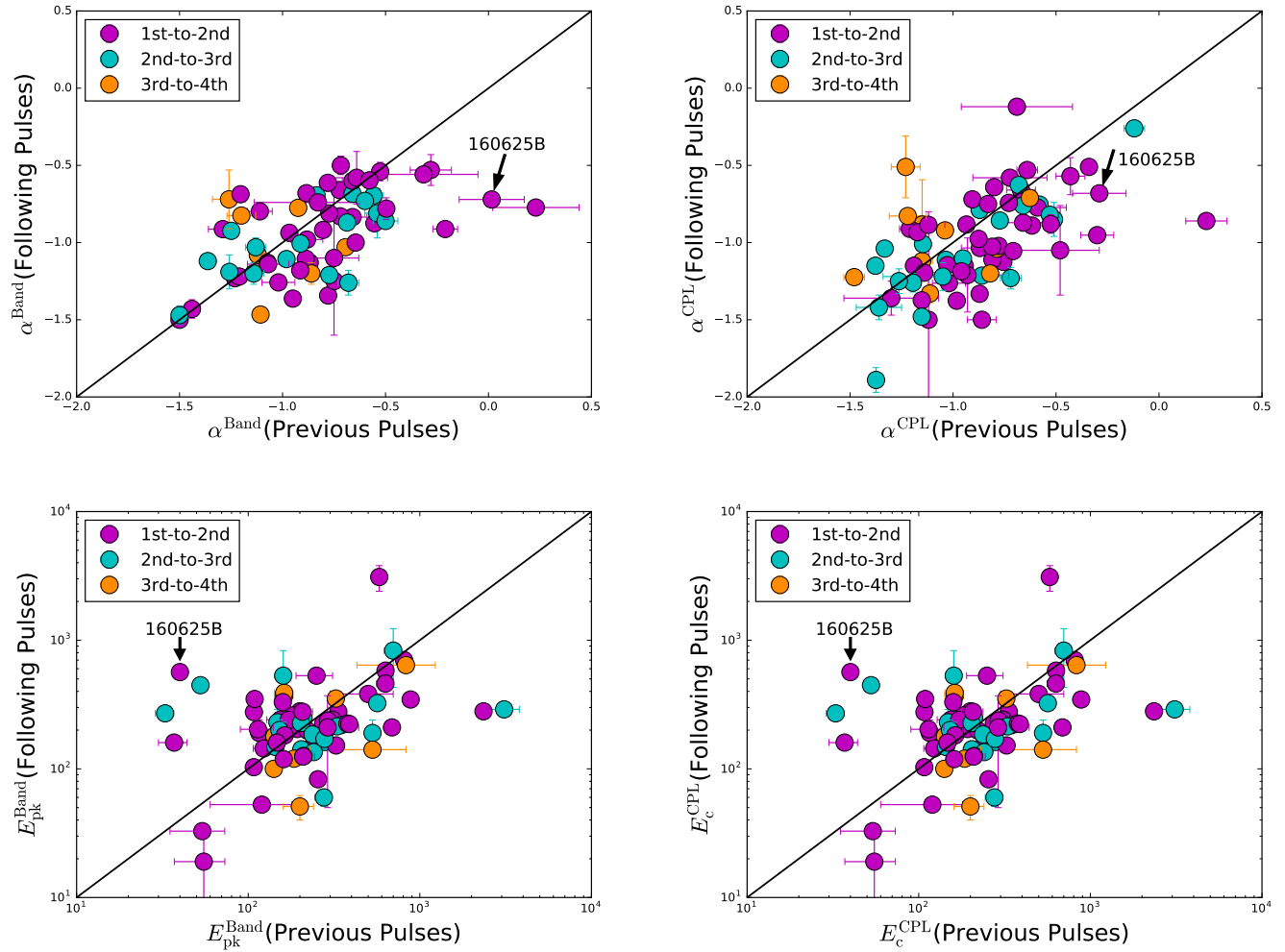


Figure S3. Relations of α (top panels) and $E_{\text{pk}(c)}$ (bottom panels) for different pulses/sub-bursts: 1st to 2nd (pink), 2nd to 3rd (cyan), and 3rd to 4th (orange), all of which are based on the time-integrated spectral fit results. Top left and bottom left panels are for the Band model, and top right and bottom right panels are for the CPL model. GRB 160625B for the case is labeled with the arrows.

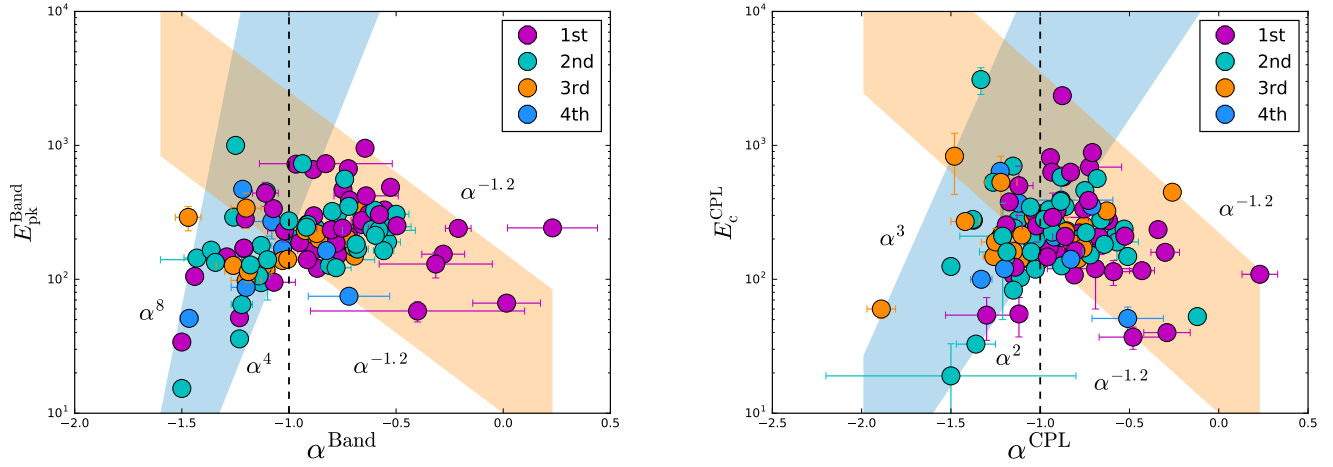


Figure S4. $E_{\text{pk}}-\alpha$ relation for different pulses/sub-bursts: 1st (pink), 2nd (cyan), 3rd (orange), and 4th (blue), which are based on the time-integrated spectral fitting results. One vertical dashed line represents the typical value of $\alpha=-1.0$. The left panel is for the Band model, and the right panel is for the CPL model.

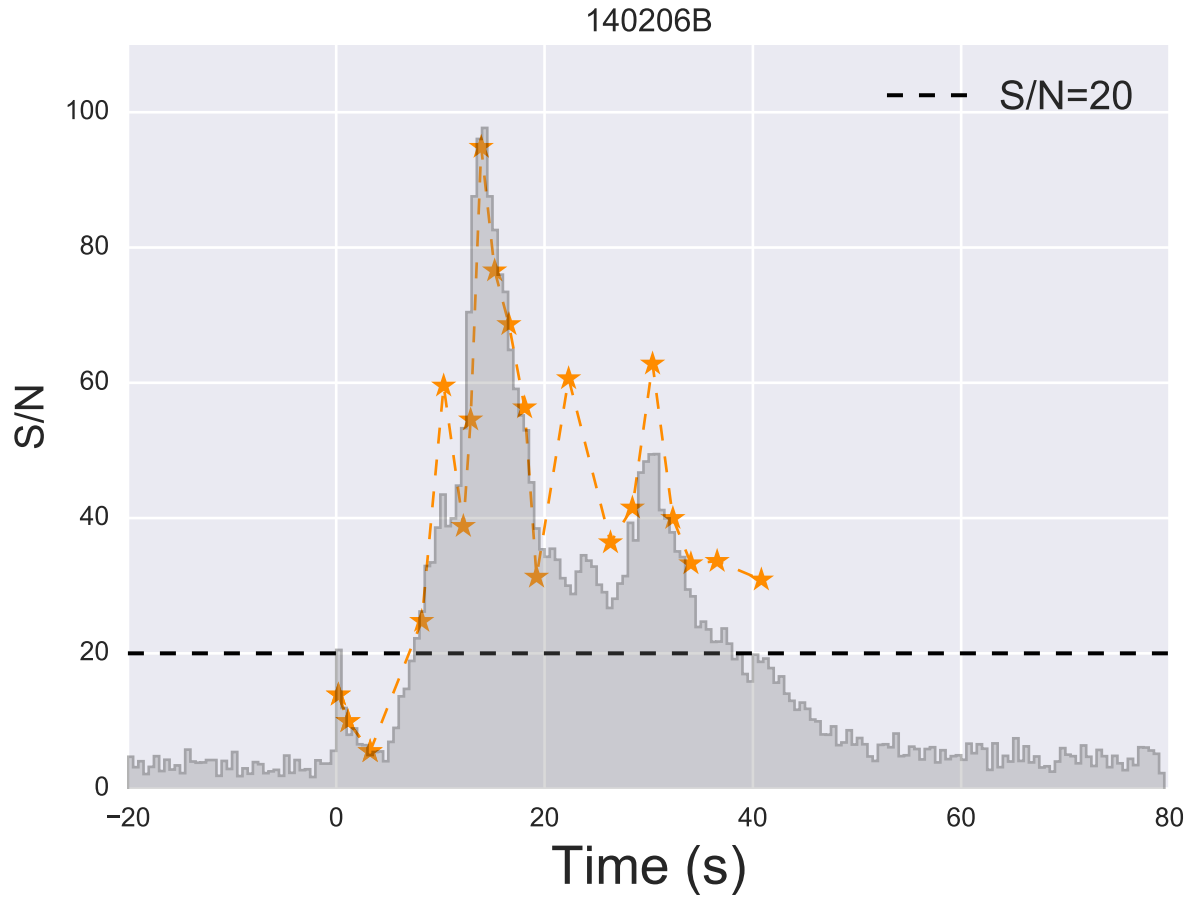


Figure S5. Light curve of the prompt emission of GRB 140206B (the right-hand y-axis), along with temporal evolution of the S/N (yellow stars and the left-hand y-axis). The horizontal dashed line represents an S/N value of 20.

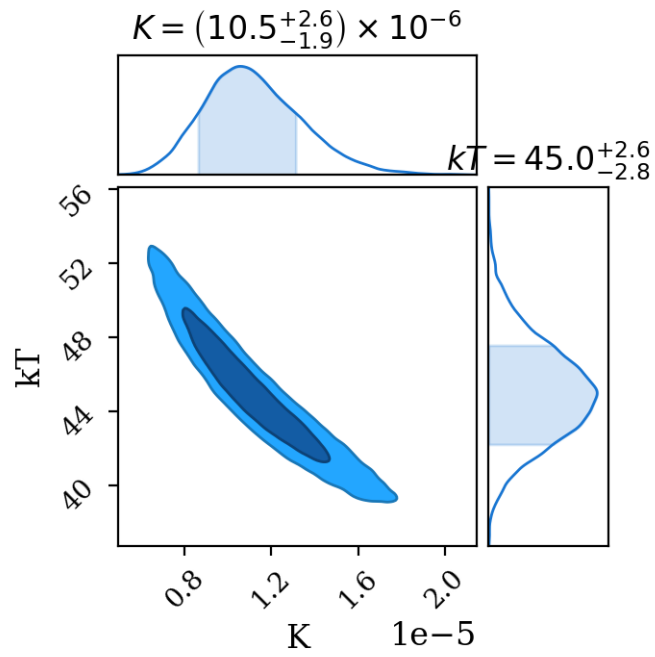


Figure S6. Example fit to the data in one time bin (between 0.46s and 1.81s) of GRB 140206B using the BB model.

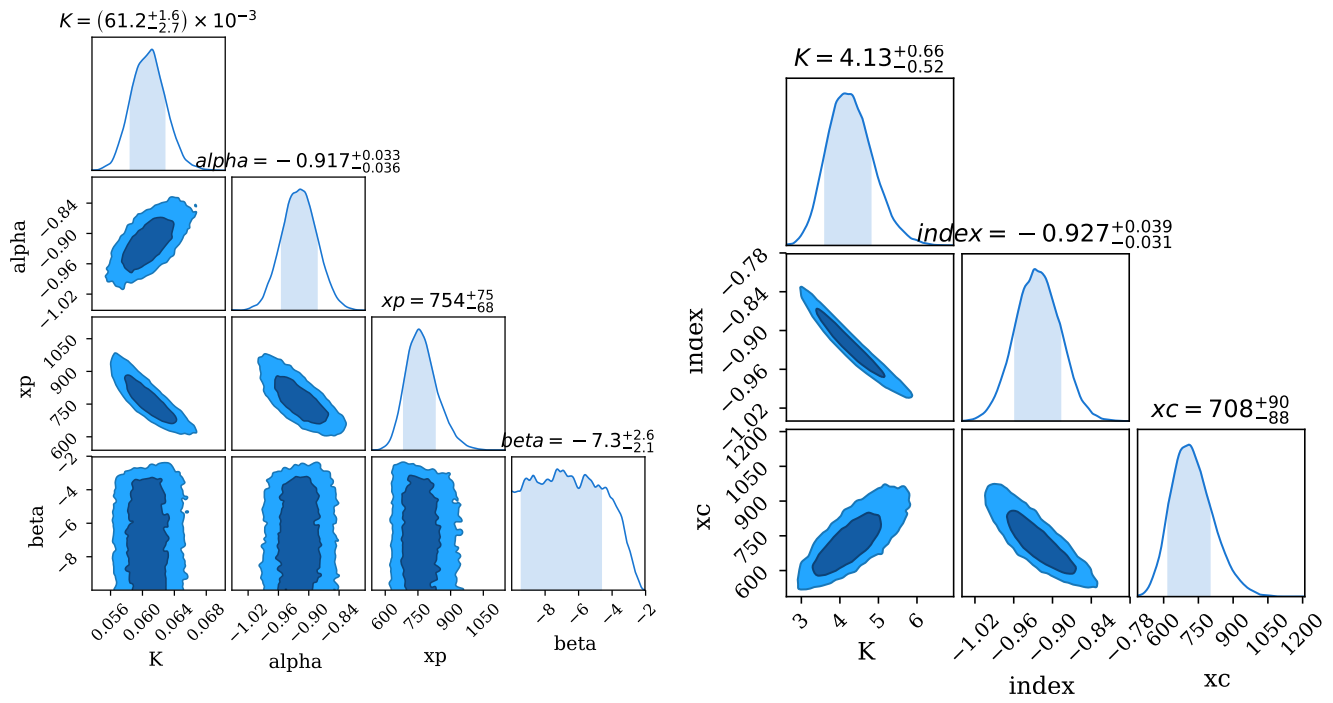


Figure S7. Example fit to the data in one time bin (between 11.84s and 12.57s) of GRB 140206B using the Band model and the CPL model, respectively. Left panel: the Band model with an unconstrained parameter β ; right panel: the CPL model.

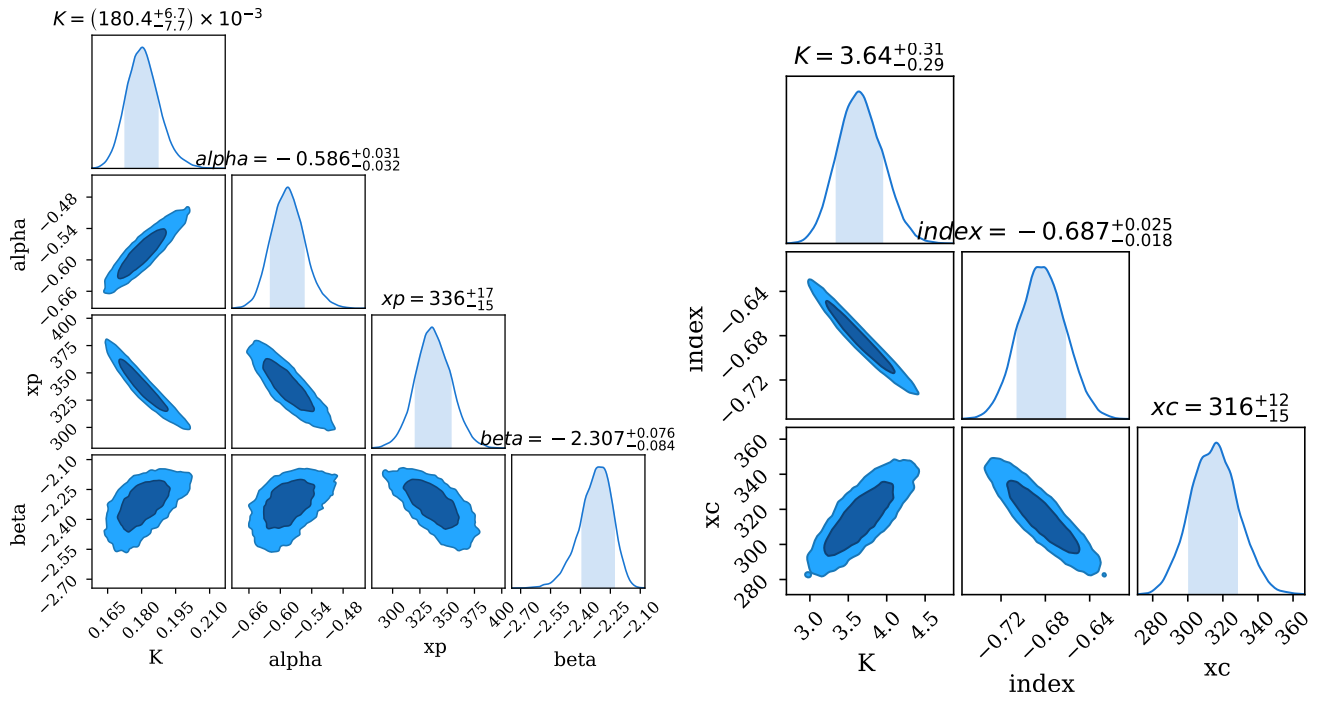


Figure S8. Example fit to the data in one time bin (between 13.24 and 14.60s) of GRB 140206B using the Band model and the CPL model, respectively. Left panel: the Band model with a well-constrained parameter β ; right panel: the CPL model.

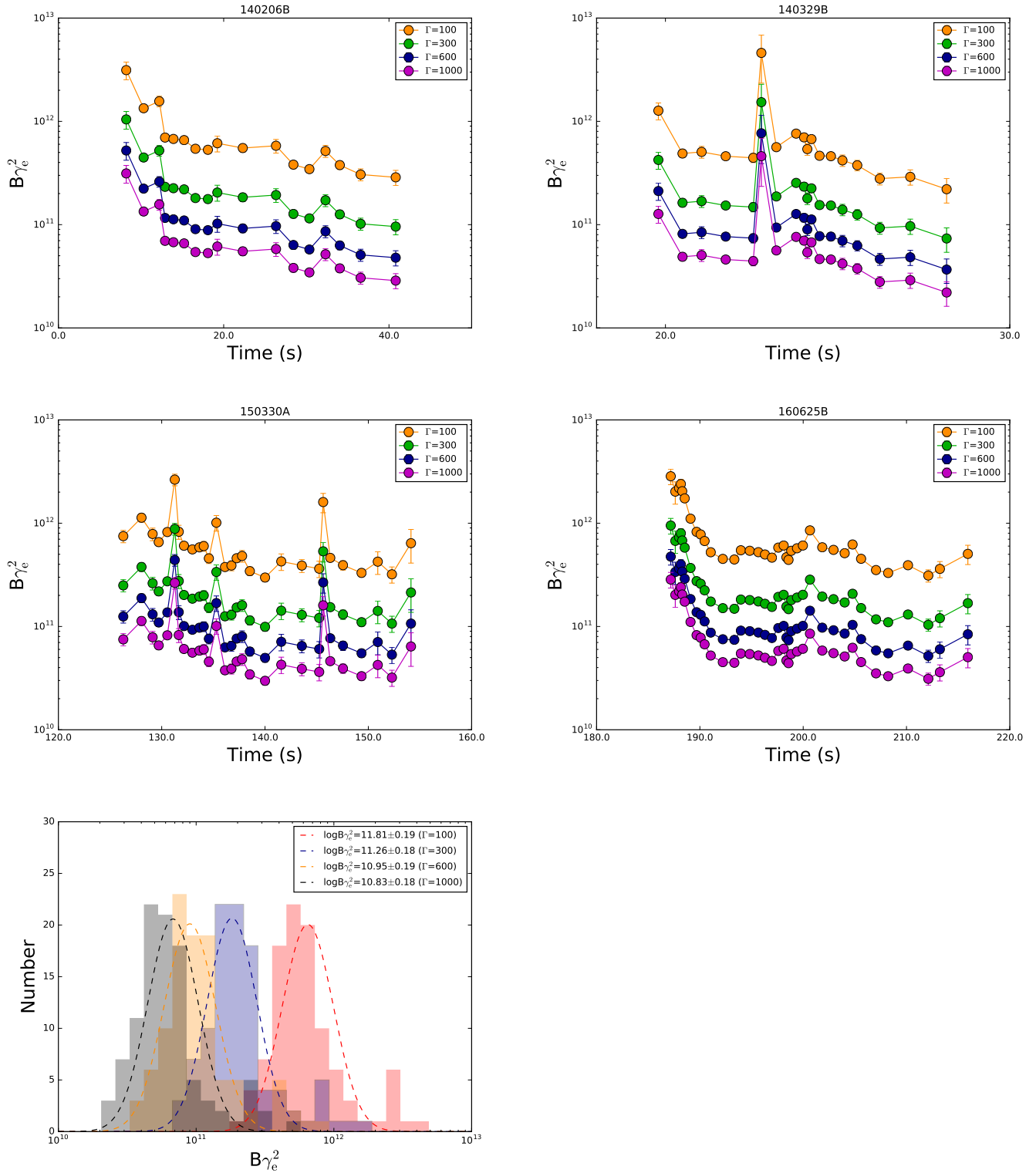


Figure S9. Temporal evolution of $B\gamma_e^2$ for various typical Γ values; different colors represent different Γ values. Distributions of $B\gamma_e^2$ are based on these four typical Γ values: $\Gamma=100$ (orange), $\Gamma=300$ (green), $\Gamma=600$ (blue), and $\Gamma=1000$ (pink). The best Gaussian fitting gives $\log B\gamma_e^2=11.81\pm 0.19$ for $\Gamma=100$, $\log B\gamma_e^2=11.26\pm 0.18$ for $\Gamma=300$, $\log B\gamma_e^2=10.95\pm 0.19$ for $\Gamma=600$, and $\log B\gamma_e^2=10.83\pm 0.18$ for $\Gamma=1000$.